# EXTREME WINDS: IMPACTS OF HURRICANES AND RAMP EVENTS ON WIND ENERGY

by

ROCHELLE PAULINE WORSNOP

B.S., Florida State University, 2012

M.S., University of Colorado, 2016

A thesis submitted to the

Faculty of the Graduate School of the

University of Colorado in partial fulfillment

of the requirement for the degree of

Doctor of Philosophy

Department of Atmospheric and Oceanic Sciences

2018

This thesis entitled:
Extreme Winds: Impacts of Hurricanes and Ramp Events on Wind Energy
written by Rochelle Pauline Worsnop
has been approved for the Department of Atmospheric and Oceanic Sciences.

Prof. Julie Lundquist

Dr. George Bryan

Date____________________

The final copy of this thesis has been examined by the signatories, and we find that both the content and the form meet acceptable presentation standards of scholarly work in the above mentioned discipline.

Worsnop, Rochelle Pauline (Ph.D., Department of Atmospheric and Oceanic Sciences)

**Extreme Winds: Impacts of Hurricanes and Ramp Events on Wind Energy**

Thesis directed by Associate Professor Julie K. Lundquist

# Abstract

Extreme fluctuations of wind cause damaging loads on wind turbines and pose significant difficulties in wind power forecasting. Increased global interest to move from conventional to renewable energy sources highlights the importance of successful wind energy integration into the electrical grid. Knowledge of extreme atmospheric phenomena that may affect wind turbines and the power they produce is critical to a wind farm's success. This dissertation addresses two types of extreme events: extreme winds in the hurricane boundary layer, and forecasting challenges of rapid changes in wind speeds, or wind ramping events.

First, this dissertation quantifies the extreme wind conditions that future offshore wind turbines, placed in hurricane-prone regions, could experience. The analyses include novel large-eddy simulations of major hurricanes evaluated with real hurricane reconnaissance flights. Investigations into turbulence characteristics, mean wind speeds, 3-s gusts, wind veer, and wind shear at different locations of the hurricane provide first-ever estimates of how these variables could impact wind turbines. Comparisons of these variables to current wind turbine design standards suggest that modifications to the standards may be required to represent extreme hurricane conditions.

Work presented herein also addresses the difficulty in predicting power ramp events, which are large and abrupt changes in wind power production. These ramp events often lead to costly fees imposed on wind farm operators and decreased reliability of wind as an energy source. An exploration of four multivariate statistical post-processing techniques is performed to improve power ramp forecasts by the High-Resolution Rapid Refresh model. Specifically, the techniques seek to reduce under- and over-forecasting biases of ramp events and provide valuable uncertainty information through the generation of numerous forecast scenarios.

All of the research discussed herein alludes to modifications of current turbine design or forecasting practices to account for extreme wind conditions. Therefore, recommendations to change design codes and to increase forecast skill are provided throughout the main chapters.

# Acknowledgements

I did not get to the point of writing this dissertation on my own, rather this work is a culmination of many people's encouragement, guidance, generosity, and love. I first thank my undergraduate research mentors, Melissa Griffin and Shaun Smith who gave me my first opportunity to research and inspired me to pursue graduate school. Dr. Evan Kalina, MaryEllen Kalina and Donald Kalina assisted me with my National Science Foundation fellowship application to make sure that I presented my research and myself in an exciting way, and for that, I am so thankful. I received this fellowship to fund three years of my graduate career, and I attribute a big part of this success to them.

During my years in graduate school, I could not have been blessed with a more intelligent, intuitive, and kind advisor. I came to CU to work with Dr. Julie Lundquist and received a multitude of knowledge about not only research skills, but also networking, career preparation, and life. She always knew the perfect balance of when to provide guidance and when to let me explore and figure things out on my own. She also exemplified a care towards everyone and taught through her actions that science is not just about the numbers, but also about the people that crunch them. Thank you, Julie!

I also greatly appreciate the many wonderful coauthors that I have had the honor to do research with. I learned a great deal from conversations with them, their feedback, and best practices. I especially want to thank Dr. George Bryan and Dr. Michael Scheuerer for their mentorship. They did not have to answer my millions of curious questions, but did so patiently and with enthusiasm. Their expertise and excitement for their science is infectious, and I hope to excite others about science one day like they have me. I also thank my thesis committee members, Dr. Julie Lundquist, Dr. George Bryan, Dr. Katja Friedrich, Dr. Peter Hamlington, and Dr. Branko Kosović, for their feedback and discussions during my second comprehensive exam and defense. I would not have been able to attend graduate school if it were not for the support of the Department of Atmospheric and Oceanic Sciences. The department provided me with a year of funding to be a teaching assistant and provided a great environment to learn.

The most enjoyable moments that I have had in graduate school are the ones that I have shared with my peers, especially the cohort I began graduate school with and the members of my research group. Nights spent on Pearl Street, movie/game nights, hikes in the mountains, and many hours lamenting over broken code with these great people are forever stamped in my memory. I especially thank Dr. Evan Kalina, Dr. Brian Vanderwende, Dr. Clara St. Martin, Dr. Stephanie Higgins, Chris Maloney, and Josh Pettit for their warm and fun friendship.

It may be impossible for me to express how grateful I am for my parents Fred and Susie Worsnop. My parents instilled in me a work ethic that got me to this point, especially during times when I felt I had no idea what I was doing. They believed in me even when I thought I would fail. I owe my Dad for my passion for meteorology and the outdoors and for my desire to watch possibly dangerous weather phenomena. I owe my mom for my faith in God. I have never met a more devoted and inspiring person of faith. She always reminded me that God would help me no matter the situation, and even though I sometimes could not see it, I knew she was right about this. Thank you both for providing me with a loving household growing up and for supporting me through my grand adventures to become a scientist.

Finally, I thank the most influential person in my life, my partner Dr. Evan Kalina, who also graduated from the Department of Atmospheric and Oceanic Sciences. He supported me through undergraduate and graduate school, even during my annoying times of doubt. I cannot thank him enough for the guidance he gave me with classes, and when I was first learning how to code. Our conversations make me a better scientist and person. His work ethic, passion for science, and determination to solve problems no matter how difficult are admirable and truly inspiring. Thank you for always showing me love and support and for providing me with endless and challenging adventures through the mountains. You have made graduate school not only bearable but enjoyable! Thank you, Evan!

# Table of Contents

# List of Tables

# List of Figures

# List of Abbreviations

| | |
|---|---|
| **AGL** | Above Ground Level |
| **ASL** | Above Sea Level |
| **ASOS** | Automated Surface Observing System |
| **AWEA** | American Wind Energy Association |
| **CBLAST** | Coupled Boundary Layer Air-Sea Transfer [Experiment] |
| **CM1** | Cloud Model 1 [Model] |
| **CM1C** | Complex configuration of CM1 |
| **CM1S** | Simple configuration of CM1 |
| **Coh** | Coherence |
| **CPSD** | Cross-power Spectral Density |
| **DOE** | Department of Energy |
| **EU** | European Union |
| **FAST** | Fatigue, Aerodynamics, Structures, and Turbulence [Simulator] |
| **GC** | Gaussian Copula |
| **GHG** | Green House Gas |
| **GWEC** | Global Wind Energy Council |
| **HBL** | Hurricane Boundary Layer |
| **HRRR** | High-resolution Rapid Refresh [Model] |
| **Hz** | Hertz [Unit] |
| **IEC** | International Electrotechnical Comission |
| **LES** | Large-eddy Simulation |
| **LIST** | Long-term Inflow and Structural Test program |
| **MDSS** | Minimum Divergence Schaake Shuffle |

| | |
|---|---|
| **MDSS+** | Enhanced Version of MDSS |
| **NCAR** | National Center for Atmospheric Research |
| **NHC** | National Hurricane Center |
| **NOAA** | National Oceanic and Atmospheric Administration |
| **NREL** | National Renewable Energy Laboratory |
| **NWTC** | National Wind Technology Center |
| **PBL** | Planetary Boundary Layer |
| **PSD** | Power Spectral Density |
| **RMW** | Radius of Maximum Winds |
| **StSS** | Standard Schaake Shuffle |
| **TKE** | Turbulent Kinetic Energy |
| **TS** | Tropical Storm |
| **US** | United States of America |
| **UTC** | Coordinated Universal Time |
| **WRF-ARW** | Advanced Research Weather Research and Forecasting [Model] |

# 1 INTRODUCTION

Wind energy extraction, now a modern and mature source of electricity that rivals that of conventional methods in production, reliability, and cost, began as one of civilization's first means of harnessing energy from the natural environment. Wind energy propelled early sailors across bodies of water, and with the creation of primitive windmills, it also provided energy to grind grains, pump water for irrigation, drain marshy areas, and aided in textile production. Although the use of wind energy has ebbed and flowed throughout history, with a significant reduction in use during the onset of the steam engine in the 1700s, wind energy and wind turbines have made a remarkable resurgence around the world over the last century and a half. Wind turbines are still used to convert kinetic energy of the wind into mechanical energy as used for the purposes listed above, but in recent decades, the conversion of kinetic energy in the wind to electrical energy has rapidly expanded the global development and use of renewable energy.

According to the Global Wind Energy Council (GWEC 2017), during the last 16 years, global installed wind capacity grew from 23.9 GW in 2001 to more than 486 GW by the end of 2016 (Figure 1.1a) with over half (251 GW) of the total wind capacity added within the last five years alone (Figure 1.1b). Nearly thirty countries had > 1000 MW of total installed wind capacity by the end of 2016 and nine countries had > 10,000 MW, including the US. The US currently ranks as the country with the second highest total installed capacity (> 80 GW) trailing behind China's impressive 168,732 GW of installed capacity. The 2016 US wind power production supplied 5.5% of the nation's electricity, which equated to electricity for approximately 24 million homes (GWEC 2017). The state of Iowa produced 36.6% of its electricity generation from wind power at the end of 2016, the highest percentage in the nation, and Texas, with the greatest amount of installed wind capacity (> 21 MW) in the US, produced 12.6% of its electricity from wind (AWEA 2017). Increasing trends are also seen in the overall size and capacity of wind turbines during the last 15 years (Figure 1.2), with the greatest increase occurring in the average size of the wind turbine rotor diameter. Newly installed wind turbines in the US now average 80-m hub heights, 110-m rotor diameters, and an average nameplate capacity > 2 MW (DOE 2017).

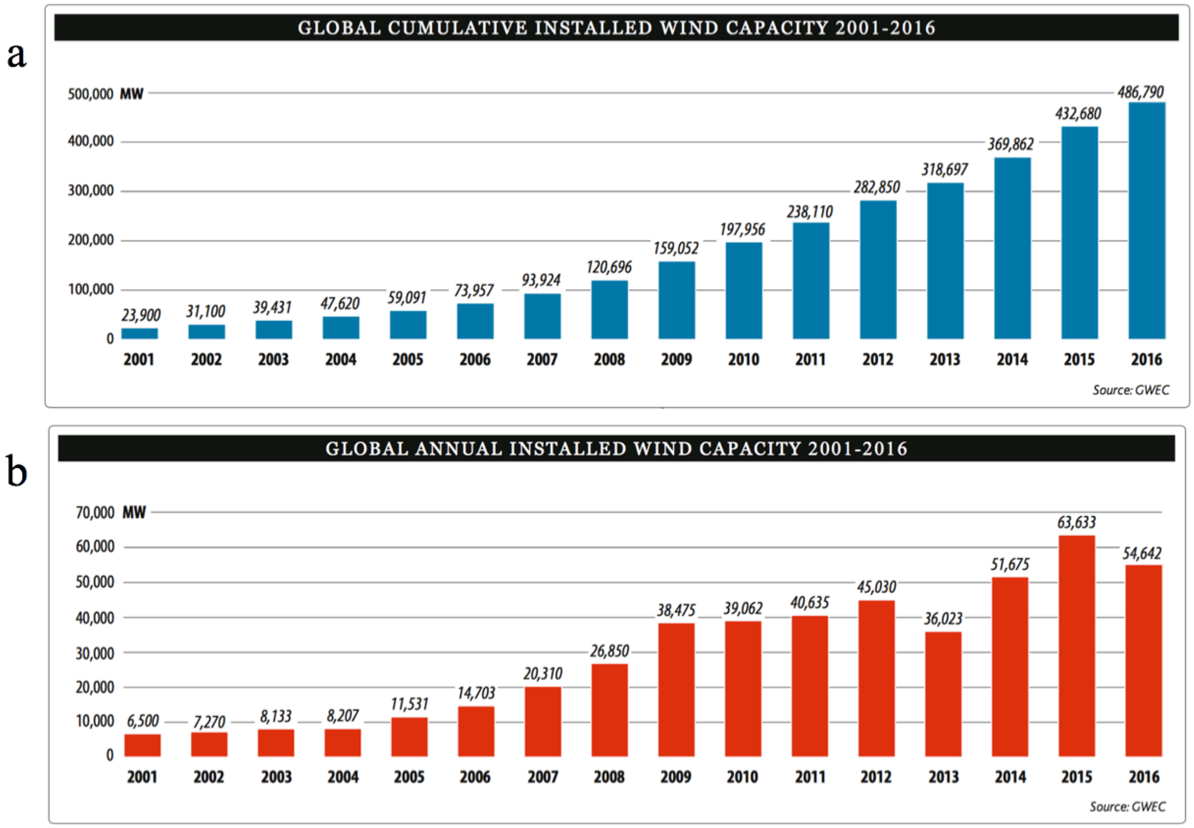

Figure 1.1 Global cumulative  installed wind capacity from 2001-2016 (a) and the global wind capacity installed each year from 2001-2016 (b). Source: Global Wind Report 2016 (GWEC 2017). Available online at [http://gwec.net/publications/global-wind-report-2/].

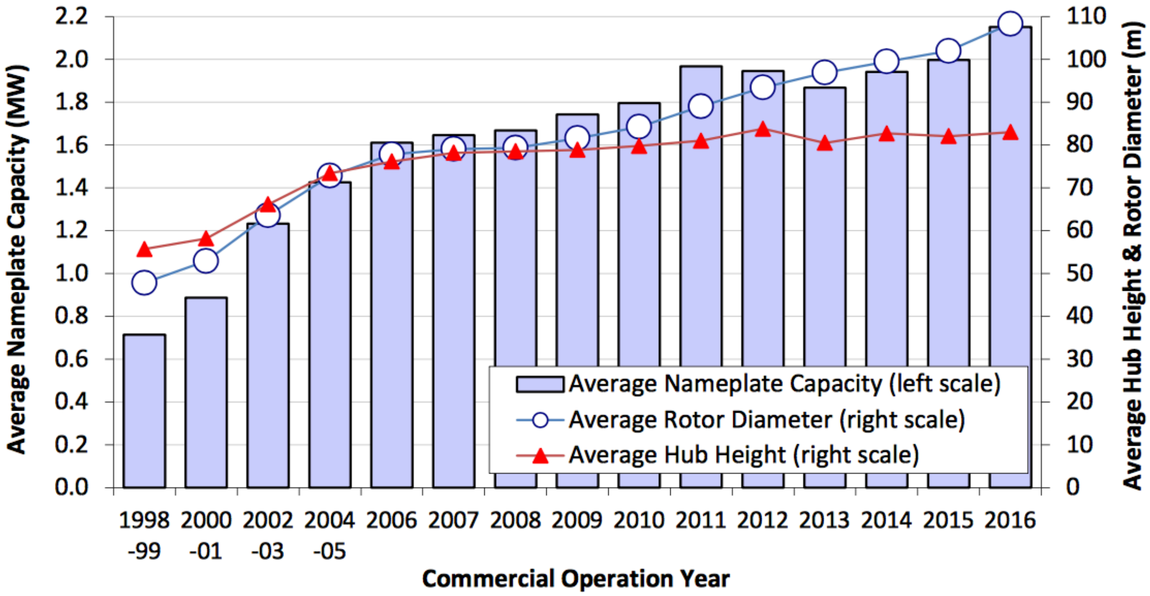

Figure 1.2 Average turbine nameplate capacity (bars, left scale), rotor diameter (line with circles, right scale), and hub height (line with triangles, right scale) from years 1998–2016. Figure from DOE 2017. Available online at [https://energy.gov/sites/prod/files/2017/08/f35/2016_Wind_Technologies_Market_Report_0.pdf].

As of 2016, wind energy production in the US no longer solely comes from onshore wind farms. In December 2016, America's first commercial offshore wind farm built 6 km southeast of Block Island, RI pumped electricity through its transmission lines buried underneath the ocean floor to mainland RI (Justin Gillis 2016). The Block Island wind farm comprises five 6-MW turbines to provide a total capacity of 30 MW of clean energy to the island and mainland.

Although land-based wind resource has the potential to provide enough generation to meet US energy demand, the offshore wind resource offers many advantages over its counterpart. Onshore wind farms require large amounts of land for maintenance roads and for adequate spacing between turbines and upwind obstructions. Collocating large-scale wind farms with agricultural farms has worked extremely well for states in the Midwest and the Great Plains where farms and open-land are abundant. However, open land is sparse along densely-populated coastal regions where the electricity demand is the highest. Additionally, transmission lines across multiple state borders spreading hundreds of miles are expensive, cumbersome, and more likely to lose voltage the longer the transmission lines become. The use of offshore wind resource circumvents these issue by harnessing momentum from the wind and converting it to electricity only a few kilometers away from the populated coastline. Regions with offshore wind speeds $\geq 7$ m $s^{-1}$ at hub height (100 m) are considered good locations for wind farm development; these areas exist all along US coastlines except for portions along the Florida coastline and just offshore of southern California (Figure 1.3). Offshore and coastal wind turbines can take advantage of sea breezes as well; sea breezes increase power performance during peak energy demand during spring and summer months (Dvorak et al. 2012). Offshore wind development also allows for larger wind turbines (i.e., height and rotor diameter) because there are fewer transportation constraints at sea than over land. Also, wind speeds just off the coasts of the US tend to be stronger and more steady throughout the day, which increases overall power generation and decreases wear and tear on wind turbine components (Musial et al. 2016).

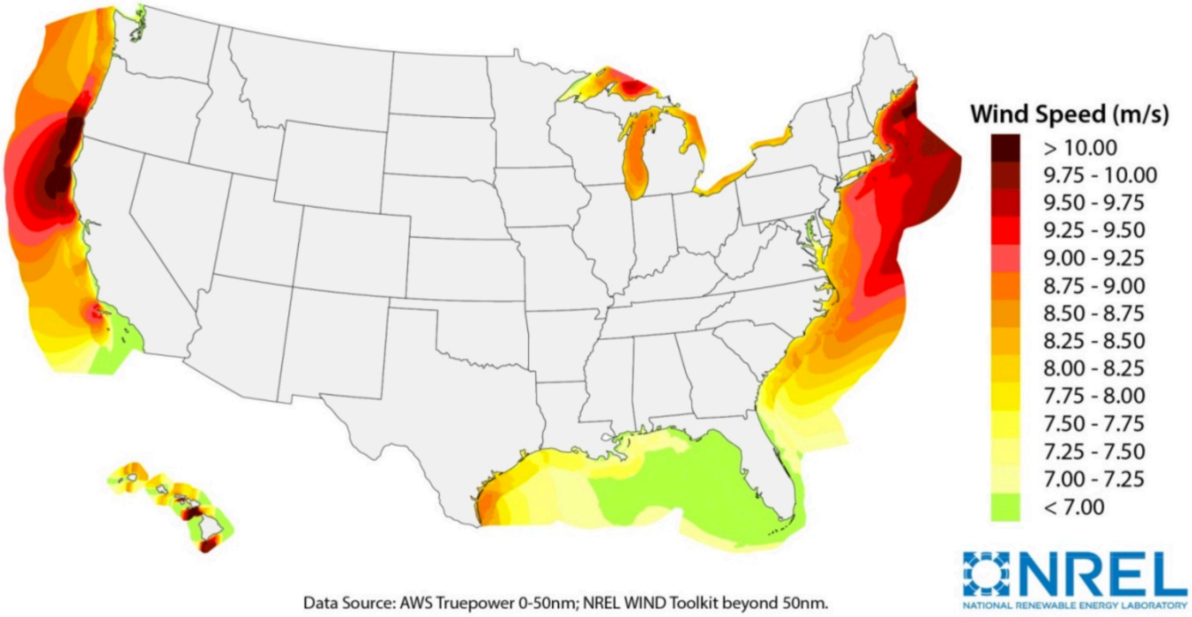

Data Source: AWS Truepower 0-50nm; NREL WIND Toolkit beyond 50nm.

Figure 1.3 United States offshore wind resource at 100 m above sea level extending out to 50 nm. NREL WIND Tooklit provided wind resource estimates beyond 50 nm from the coastline. Regions with wind speeds ≥ 7 $m\ s^{-1}$ are considered adequate for wind energy development. Map provided by NREL, AWS Truepower, and Vaisala/3TIER (Musial et al. 2016). Available online at [https://www.nrel.gov/docs/fy16osti/66599.pdf].

Despite the great advantages of offshore wind over its onshore counterpart, offshore wind farms are a relatively recent development. The first offshore wind turbines originated in the shallow waters (< 30 m) of the Baltic Sea and North Sea; the first offshore wind turbine was a single 220-kW turbine deployed by Sweden in 1990 (Nikolaos 2004). Since then, other countries in the European Union (EU) have become world leaders of offshore wind. Demark installed the first offshore wind farm, Vindeby, in 1991. The wind farm consisted of eleven 450-kW wind turbines with a total wind farm capacity just shy of 5 MW (Bilgili et al. 2011). At present, the London Array is the largest offshore wind farm, which is located 20 km from the coast of the United Kingdom and consists of 175 3.6-MW turbines (London Array 2017). At peak performance, the London Array provides 630 MW of clean energy.

Offshore wind development is not without its challenges, which have significantly contributed to the late deployment of offshore wind turbines compared to turbines on land. Worldwide, offshore turbines require more expensive marine foundations and submarine transmission lines, which are often drilled into the sea floor (BOEM 2017). Sturdier materials to withstand salt-water intrusion and turbulent ocean waves also increase the cost (Musial and Butterfield 2004). Additionally, current offshore wind technology limits turbine deployment to water depths $< 1000$ m, with the most feasibility for deployment for depths $< 60$ m (Musial et al. 2016). This depth limitation is reached within $\approx 50$ nautical miles (nm) from the US east coast and $\approx 30$ nm from the US west coast (Musial et al. 2016). Nonetheless, the benefits of offshore wind resources hold promise for the expansion of wind generation capacity. However, unique meteorological challenges influence offshore deployments in the waters of North American, Asian, and African countries, which aside from political and societal reasons, are some of the reasons why offshore wind development in these countries is decades behind that of the EU.

Tropical cyclones are referred to as hurricanes in the Atlantic Ocean and northeastern Pacific Ocean (i.e., for sustained 1-min averaged wind speeds $> 33$ m s$^{-1}$ at 10-m above ground level), and as typhoons in the northwestern Pacific Ocean. These cyclones are serious hazards to offshore structures, including wind turbines. Recently, hurricanes have damaged wind turbines: hurricane Maria made landfall over Puerto Rico on 20 September 2017 as a Category 4 hurricane, devastating the island and severely damaging the Punta de Lima wind farm, which is located on the east coast of Puerto Rico (Figure 1.4a). The coastal wind farm was comprised of 13 Vestas 1.8 MW turbines. After landfall, at least 8 of the turbines were damaged as demonstrated by broken blades and towers in images (Figure 1.4b, c) captured by the National Oceanic and Atmospheric Administration's

(NOAA) Emergency Response Imagery (NOAA 2017). The remaining five turbines were not visible in the imagery, but may have incurred damage as well. Despite risk of hurricane damage, the lucrative offshore-wind market and increasing support for clean, renewable energy to mitigate greenhouse gas (GHG) emissions has propelled these countries and international development companies to propose or begin offshore energy production, particularly in the US, China, Taiwan, Japan, and the Philippines.

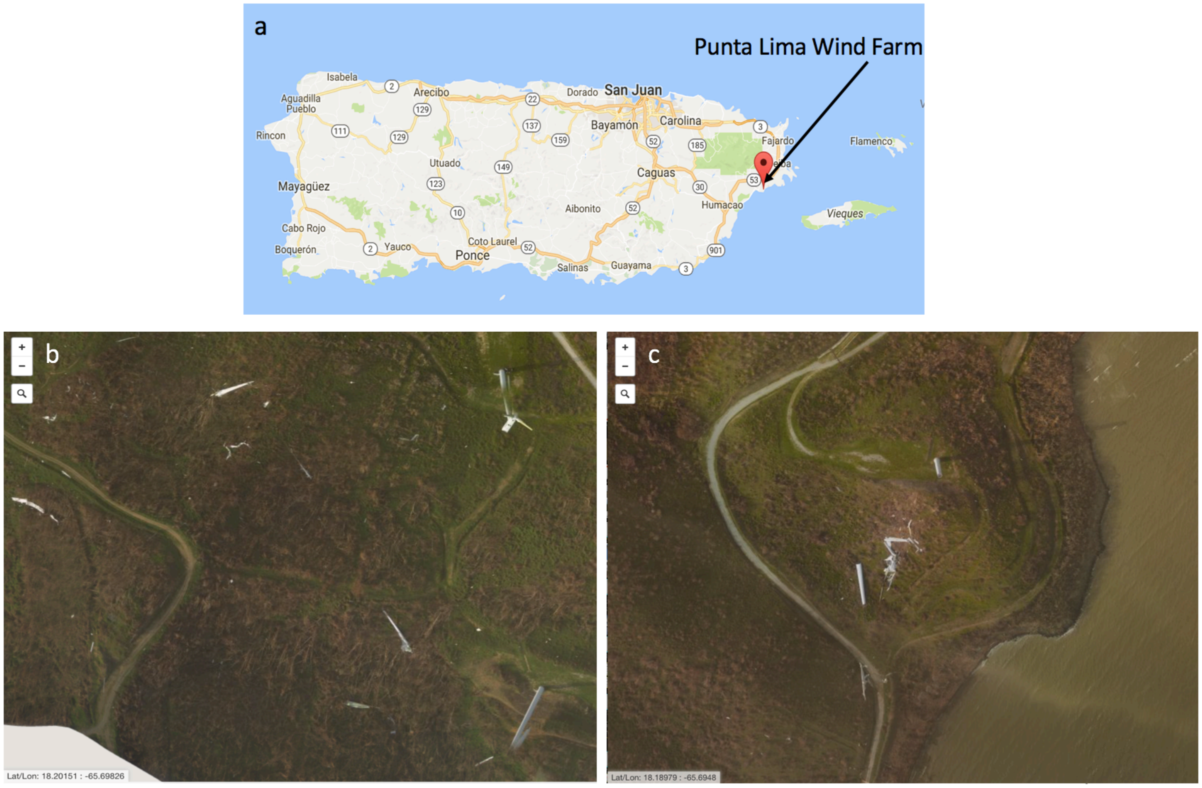

Figure 1.4 Map of Puerto Rico marked with the location of the Punta de Lima wind farm (a), pictures of damaged wind turbines from Punta Lima wind farm (b and c). Image b is centered around 18.202°N, -65.698°W and image c is centered around 18.189°N, -65.695°W. The map is from https://maps.google.com and the turbine pictures are from the NOAA Emergency Response Imagery database (NOAA 2017) available online at [https://storms.ngs.noaa.gov].

The Block Island wind farm off the coast of Block Island, RI is not in great risk of damage from major hurricanes (Category 3 or higher on the Saffir-Simpson hurricane wind scale), but potential sites for offshore wind farms in the waters off of the southeast US and

Asian countries are at risk. Further complexity arises for development in these areas, because quantifying the winds offshore turbines would experience in these intense hurricanes is extremely difficult. Most wind measurements inside of hurricanes are made either from flights several kilometers above sea level (ASL) or from buoys or meteorological towers at 10 m above ground level (AGL), missing critical observations of the flow at altitudes where the turbine rotor layer would exist (≤ 200 m ASL). Additionally, instrumentation on the ground often incur damage during the passage of major hurricanes (Figure 1.5) leaving the data unreliable.

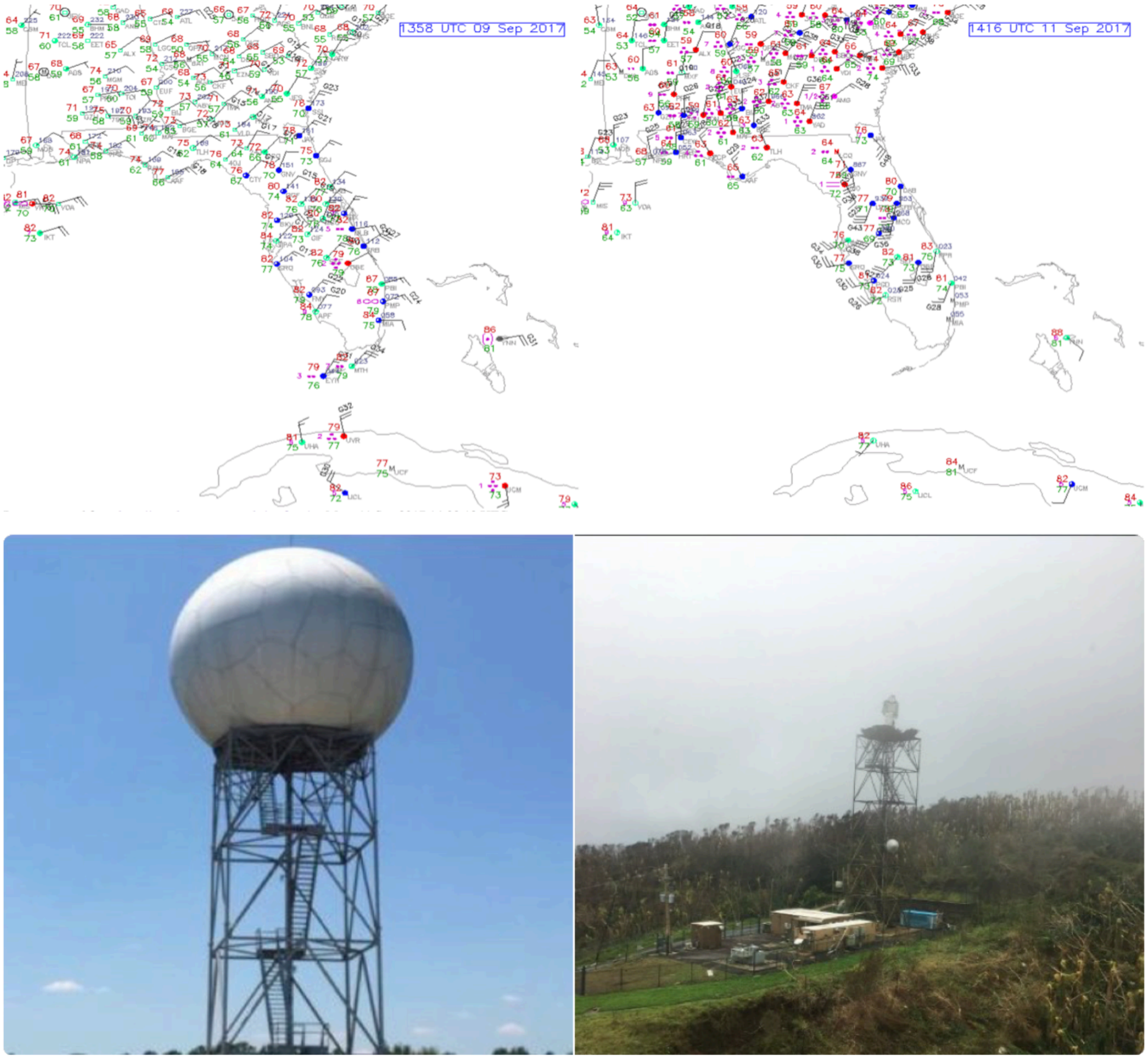

Figure 1.5 Surface weather maps before (top left) and after (top right) landfall of Hurricane Irma September 2017 over Cuba and the Florida peninsula. Approximately ten ASOS stations no longer visible in the right image were damaged during landfall. Irma made landfall as a Category 5 hurricane in the far northeastern portion of Cuba, but the portion of the country shown here as well as portions of southern FL endured Category 3 and 4 hurricane-force wind speeds. Weather maps are from the National Center for Atmospheric Research Real-Time Weather Data webpage (NCAR 2017) and available online at [http://weather.rap.ucar.edu/surface/]. Photos of the National Weather Service's NEXRAD radar in San Juan, Puerto Rico before (bottom left) and after (bottom right) landfall of the then Category 4 Hurricane Maria on 20 September 2017. Radar photos are from (Samenow 2017) and available online at [https://www.washingtonpost.com/news/capital-weather-gang/wp/2017/09/25/hurricane-maria-destroyed-puerto-ricos-radar-a-critical-tool-for-forecasting/?utm_term=.068f1e876b6e].

Without adequate observations, how can we answer the following questions: how strong are the winds and how swift are the changes in wind direction that offshore wind turbines would experience during a direct eyewall hit? Are current wind turbine design standards robust enough for hurricane conditions? If not, what modifications to the standards are needed? Additionally, do all portions of a hurricane present challenges for offshore wind turbine survival, or rather is it only certain regions of the hurricane that are problematic? To answer these questions, I ran large-eddy simulations (LES) of an idealized Category 5 hurricane using the Cloud Model 1 (CM1) model. The LES resolve most of the turbulence within the eyewall of the hurricane, the region with the strongest and most turbulent winds. The LES also provide critical spatial and temporal data that observations cannot (i.e., estimates of wind characteristics at every location within the hurricane). With these simulated data, I quantify regions of the hurricane for which turbines designed with the current standard would incur damage. I also offer suggestions for modification of the standard to represent hurricane environments. Discussions of the analysis I performed with these hurricane simulations and their impacts on potential offshore wind turbines are covered in the second and third chapters of this dissertation.

The final project included in this dissertation focuses on wind-power forecasting of ramp events for onshore wind turbines. Wind power is a function of the cube of the wind speed entering the wind turbine rotor layer. This nonlinear relationship between wind speed and power, known as the power curve (Figure 1.6) means that small to moderate changes in wind speed can have significant impacts on power production. Ramp events are sharp upward or downward changes in power production during short time periods on the order of minutes to hours. Ramp events challenge utilities and electrical balancing authorities, because changes in power production must be met with equal adjustments within the power grid. If an increase in power occurs, then the grid operator may choose to buy the extra power produced instead of using a more conventional carbon-based source of energy. In some cases, curtailments are necessary, in which wind turbines are turned off to reduce power production that the electrical grid cannot utilize because of congested transmission lines. These increases in power production in a short period of time (i.e., up-ramps) should be advantageous for a wind farm's bottom-line, but are actually problematic when they are not forecasted to allow time for grid operators to make allotments for extra wind-power production. Even more problematic and costly are when power production decreases drastically in a short period of time (i.e., down-ramps). Unexpected down-ramps can lead to brown- and black-outs if power grid operators cannot garner enough energy from other sources to "balance the load" on the electrical grid.

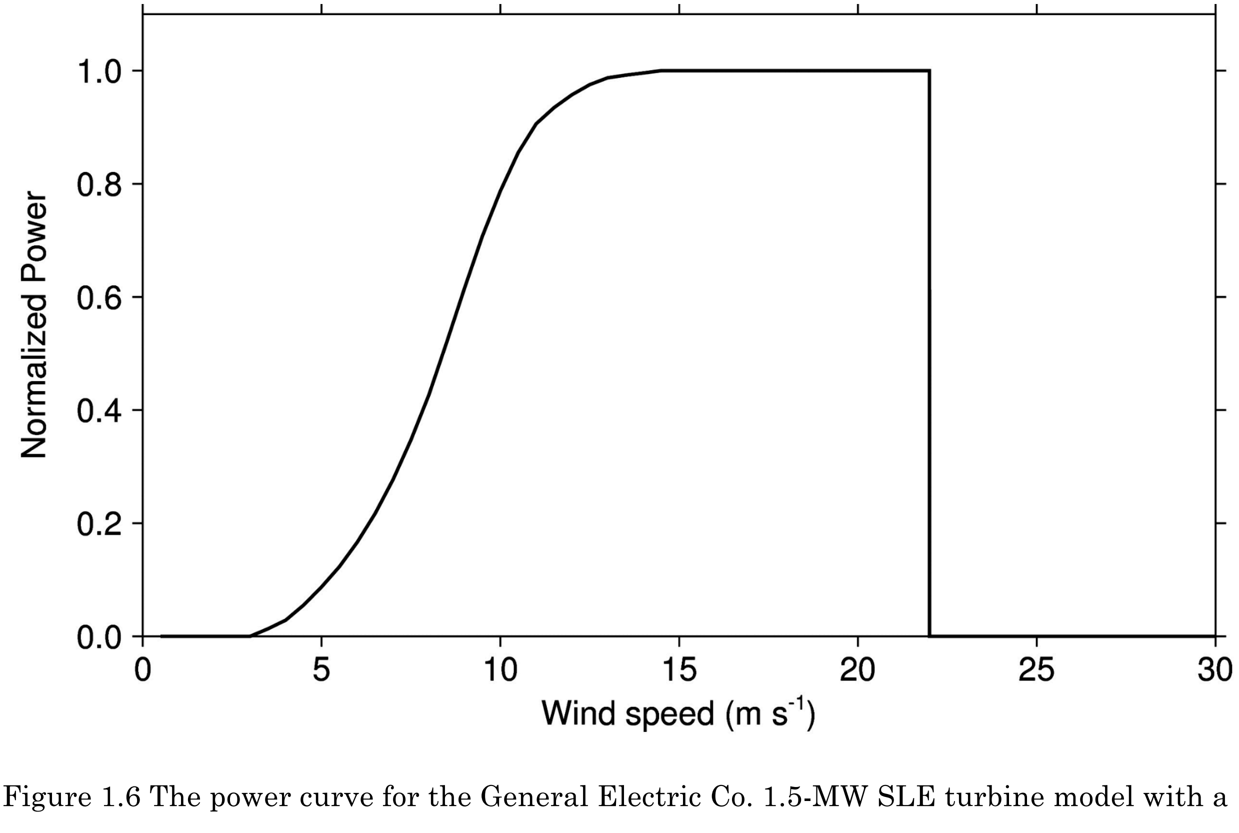

Figure 1.6 The power curve for the General Electric Co. 1.5-MW SLE turbine model with a rotor diameter of 77 m and a hub height of 80 m. Figure from Yang et al. 2013 (their Fig. 3).

Typically, wind farm operators use forecasts of persistence on the scale of 30 min to an hour to predict the upcoming power production. Persistence forecasts on short time-scales are hard to beat with numerical weather prediction, but persistence cannot capture rapid changes in production. Additionally, point or single forecasts are generally used to make decisions related to power output, but a point forecast cannot represent the many possible outcomes of power production that could occur. For these reasons, I utilized the High-Resolution Rapid Refresh (HRRR) mesoscale model and statistical post-processing techniques to generate short-term scenarios of possible power production at two onshore wind-turbine sites. Both of the turbine sites are located in regions of complex terrain, which makes wind-power forecasting even more difficult.

The addition of uncertainty information in wind-power forecasts can allow the wind-farm operator to make more conservative decisions during times of high risk (e.g., high electricity demand and potential for brown- or black-outs), or to make more liberal decisions during times of lower risk to increase revenue when there is a chance for large up-ramps in power production. Better forecasts of short-term wind power production are needed to further the success of wind energy as a clean and reliable resource in the US and worldwide.

The overall significance of the work presented in this dissertation is that it examines the viability of wind as an energy resource during times of irregular and extreme wind phenomena. This information is needed to enhance our understanding of the influences that such weather events have on wind turbines. With such knowledge, we can increase forecast skill of those events and mitigate the impacts those events have on wind turbines through robust turbine design. I quantify the vulnerability of offshore wind turbines during turbulent hurricane conditions in Chapters 2 and 3. In Chapter 2, I discuss two different methods to simulate hurricane wind profiles with LES and compare theoretical curves of power spectral density and spatial coherence to those simulated within tropical cyclones of varying strengths. In Chapter 3, I discuss wind speed and direction variables pertinent to current wind turbine design and how those variables require modification within design standards to represent hurricane conditions. I also provide analysis of veer and shear within the simulated hurricanes that are not currently included in the design standards, but may be consequential to turbine survival. Finally, in Chapter 4, I discuss how irregular and large swings in power production, known as ramps, challenge utility grids. To address this challenge, I demonstrate and verify four different methods to generate probabilistic power scenarios to improve short-term wind-power forecasting via statistical post-processing.

## Arrangement of the thesis

This dissertation outlines the three research projects that I have performed during my Ph.D. research. Each of these studies has led to publishable material, with the first study published in *Boundary Layer Meteorology*, the second published in *Geophysical Research Letters*, and the third in preparation for submission to *Wind Energy Science*. The three projects are discussed individually in the three main chapters of the thesis and each is presented as a self-contained work. Therefore, Chapters 2-4 appear like peer-reviewed journal articles and include an abstract, introduction, methods, results, and conclusion sections with figures and tables numbered appropriately for each chapter. Before delving into the research for each study, I provide a preface that summarizes the study and highlights notable details about the work. I offer general conclusions from all of the analyses in Chapter 5. References from all of the chapters are listed together after the general conclusions.

# 2 USING LARGE-EDDY SIMULATIONS TO DEFINE SPECTRAL AND COHERENCE CHARACTERISTICS OF THE HURRICANE BOUNDARY LAYER FOR WIND-ENERGY APPLICATIONS

## Preface

The US and other countries with risk of tropical-cyclone landfalls are starting to plan and construct offshore wind farms. Offshore wind resources are strong and consistent and can provide electricity to densely-populated coastal cities. A new challenge to offshore wind development is the lack of understanding of how hurricanes will impact wind turbines. This challenge is further exacerbated by the fact that adequate observations are not available to fully sample hurricane conditions in all portions of the hurricane and at heights pertinent to offshore wind turbines.

To address these challenges and to quantify the conditions offshore wind turbines would experience inside strong hurricanes, the work presented in this chapter uses two different configurations of the Cloud Model 1 to simulate hurricane data with large-eddy simulations (LES). We analyze data at multiple radii of the hurricane, which represent different hurricane strengths ranging from tropical storm to Category 4-strength on the Saffir-Simpson hurricane wind scale.

The goal of the work discussed in this chapter is to compare power spectral density (PSD) and coherence curves derived from the hurricane simulations to the theoretical curves used within current turbine design standards, which do not specifically address hurricane conditions. This analysis is performed for different hurricane radii (i.e., hurricane strength) to determine coherence and power spectral density curves for a range of hurricane strengths. The hurricane simulations presented within this chapter provide a unique dataset to analyze impacts on wind turbines during hurricane conditions. The PSD and coherence curves provided can be implemented into turbine load simulators to quantify loads on certain components of turbines to assess if design modifications are needed.

Additionally, this work compares a relatively simple method for simulating hurricane wind profiles (Bryan et al. 2017) to a more complex and computationally-expensive configuration of LES. The simple method could be used for any research requiring wind profiles within the hurricane boundary layer but away from the eyewall.

This chapter is adapted and reformatted from:

Worsnop, R. P., G. H. Bryan, J. K. Lundquist, and J. A. Zhang, 2017: Using large-eddy simulations to define spectral and coherence characteristics of the hurricane boundary layer for wind-energy applications. *Bound.-Layer. Meteor.*, 165, 55−86, doi: 10.1007/s10546-017-0266-x.

## 2.0 ABSTRACT

Offshore wind-energy development is planned for regions where hurricanes commonly occur, such as the US Atlantic Coast. Even the most robust wind-turbine design (IEC Class I) may be unable to withstand a Category-2 hurricane (hub-height wind speeds >50 m $s^{-1}$). Characteristics of the hurricane boundary layer that affect the structural integrity of turbines, especially in major hurricanes, are poorly understood, primarily due to a lack of adequate observations that span typical turbine heights (<200 m above sea level). To provide these data, we use large-eddy simulations to produce wind profiles of an idealized Category-5 hurricane at high spatial (10 m) and temporal (0.1 s) resolution. By comparison with unique flight-level observations from a field project, we find that a relatively simple configuration of the Cloud Model I model accurately represents the properties of Hurricane

Isabel (2003) in terms of mean wind speeds, wind-speed variances, and power spectra. Comparisons of power spectra and coherence curves derived from our hurricane simulations to those used in current turbine design standards suggest that adjustments to these standards may be needed to capture characteristics of turbulence seen within the simulated hurricane boundary layer. To enable improved design standards for wind turbines to withstand hurricanes, we suggest modifications to account for shifts in peak power to higher frequencies and greater spectral coherence at large separations.

## 2.1 INTRODUCTION

Plans for wind-power generation in the US outlined by the Department of Energy (DOE) suggest that the total installed wind capacity in the US will reach 113 GW by 2030, an increase from the 61 GW installed as of 2013 (DOE 2015). The DOE plan also highlights that 3 GW of future installations will derive from offshore wind turbines. Currently, proposals for offshore wind farms focus on the ocean along the north-east US, partly because of the lower risk of major hurricanes (≥ Category 3 on the Saffir-Simpson hurricane wind scale, corresponding to maximum 1-min sustained winds of 49 m $s^{-1}$ or higher at 10 m ASL) compared to the Atlantic Ocean south of New England and in the Gulf of Mexico (Dvorak et al. 2012). However, as offshore wind development expands, construction in regions vulnerable to destructive hurricanes, such as the US East Coast and the Gulf of Mexico, seems likely.

Even the most robust wind-turbine design (IEC Class I) is not rated to withstand a 10-min mean wind speed > 50 m $s^{-1}$ and a 3-sec gust of 70 m $s^{-1}$ at hub height (IEC 2007a). Since categories of hurricane intensity are assigned based on the peak 1-min sustained wind speed at 10 m ASL, we use the logarithmic wind profile (IEC 2007a) to first convert the hub-height 10-min wind speed to the corresponding wind speed at 10 m ASL. A 10-min hub-height wind speed of 50 m $s^{-1}$ corresponds to 40 m $s^{-1}$ at 10 m ASL for the same averaging period; then, assuming a wind averaging conversion factor of 0.93 (Harper et al. 2010) to convert the peak 10-min wind speed to a peak 1-min sustained wind speed at 10 m ASL, the 10-min wind speed of 40 m $s^{-1}$ becomes a 43 m $s^{-1}$ 1-min wind speed, which corresponds to a weak Category-2 hurricane. Turbine failure due to hurricanes of this intensity has occurred in Typhoons Maemi (2003) (Ishihara et al. 2005) and Usagi (2013) (Chen and Xu 2016).

Numerous simulations and observations show that hurricanes cause damage to offshore structures. A probabilistic model has estimated that a Category-3 hurricane can seriously damage 46% of towers in a 50-turbine wind farm designed with the highest current wind standards (IEC Class I) (Rose et al. 2012). Hurricanes have disastrous effects on the energy infrastructure of the oil industry; in 2005, more than 100 oil-rig platforms were destroyed by hurricanes Katrina and Rita because of wave inundation and excessive wind loads (Cruz and Krausmann 2008). The destruction resulted from inadequate structural design for withstanding a weak Category-3 hurricane, much like the current wind-turbine design standards. More accurate hurricane load estimations are needed to mitigate the destruction of wind turbines; the first step to estimating such loads is to determine the wind characteristics inside the hurricane boundary layer (HBL).

On average, 6.2 hurricanes and 2.3 major hurricanes occur each year in the Atlantic Basin based on a hurricane climatology from 1996-2009 (NHC 2016); it is important to determine how the extreme wind speeds associated with these storms affect offshore turbines. Further, hurricane frequency may decrease under future climate change, but future hurricanes may be more intense suggesting an increase in the number of major hurricanes in the late 21st century (Bender et al. 2010). As wind farms are designed to last at least twenty years (IEC 2007a), major hurricanes pose a substantial risk to offshore wind-turbine development.

Observations of the HBL are rare or incomplete. Dropsondes that descend from aircraft provide a single slant profile, but do not allow for a temporal or spatial analysis at turbine-hub height and across the rotor layer. Obvious safety concerns limit reconnaissance flights at turbine heights (< 200 m ASL). Few offshore towers exist (Archer et al. 2016), and even when instrumented towers exist and are equipped with multiple anemometers, the peak wind speed may be underestimated due to under-sampling (Nolan et al. 2014). Unmanned aircraft systems are currently being tested (Cione et al. 2016) to collect continuous hurricane data at relatively high resolution (1 Hz), but not yet at turbine heights. To address this critical data void, numerical models can be used to estimate wind speed, wind direction, and turbulence in the HBL.

Large-eddy simulations (LES) simulate wind fields and turbulence in hurricanes with a spatial resolution on the order of tens of meters; this detailed information is required to predict how wind speeds and directions in the HBL may influence loads on offshore structures such as wind turbines. The model data are particularly useful for wind-energy applications, because of the lack of observations spanning the height and width of offshore turbines (40 to 200 m ASL) during major hurricanes. A better understanding of the HBL wind characteristics, and subsequently the loads induced on turbine structures, can support turbine manufacturers in the design of sturdier structures and adequate mechanical systems to withstand the force of major hurricanes.

Turbine load estimators such as the National Renewable Energy Laboratory’s FAST model (Jonkman and Buhl 2005) rely on three-dimensional wind fields defined by atmospheric power spectral density and spatial coherence, among other variables. Such simulations rely on theoretical spectral (e.g., Kaimal et al. (1972) and von Kármán and Lin (1951)) and coherence (e.g., IEC exponential coherence (IEC 2007a)) models that may not necessarily represent the true inflow[1] conditions, particularly in a hurricane. Although the IEC 61400-3 (International Electrotechnical Commission Design Requirements for Offshore Wind Turbines) standard states that turbulence models defined for onshore turbine design should also be used for offshore turbine design, Wang et al. (2014) found that the turbulence intensity model referred to as the Normal Turbulence Model (IEC 2007a), recommended in the IEC 61400-3, does not represent the non-linear relationship between offshore turbulence intensity and wind speed.

Even though offshore turbine-inflow characteristics during hurricanes are not well understood, previous studies of atmospheric turbulence and possible turbulence effects on loads using observations have examined inflow characteristics of onshore turbines located in non-hurricane conditions. Saranyasoontorn et al. (2004) analyzed the spatial coherence (i.e., the magnitude squared of the cross spectrum normalized by the auto power spectrum of two different signals) of inflow into an onshore turbine using data collected from a turbine and an array of five upwind towers during the Long-term Inflow and Structural Test (LIST) program. Specifically, they found that the IEC exponential coherence model (described in Sect. 3.2) generally performed well for small lateral separations (≈ 6 m), but for large separations (≈ 30 m), the model overestimated coherence at most frequencies, but significantly underestimated coherence at low frequencies for wind speeds ranging from 11

---

[1] Inflow herein refers to the airflow into the turbine rotor-disk region.

– 13 m s$^{-1}$. We investigate the coherence over various lateral and vertical separations and for 10-m mean wind speeds of 23, 47, and 63 m s$^{-1}$.

Investigations of turbulent spectra in the HBL (Yu et al. 2008; Zhang 2010a; Zhang et al. 2010; Li et al. 2015) have relied on observations from less intense hurricanes (undergoing landfall), without an emphasis on turbine loads. Zhang (2010a) compared normalized spectra and cospectra of wind velocity, temperature, and humidity fluctuations to theoretical spectral curves over the land and ocean based on Monin-Obukhov similarity theory. The wind-velocity spectra in the HBL between outer rain bands compared well with the theoretical surface-layer curves from Miyake et al. (1970) over water and Kaimal et al. (1972) over land. However, Zhang (2010a) found that the frequency of peak power was shifted towards higher frequencies in the HBL, noting a structural difference between the HBL and the boundary layer over land.

These studies have motivated the need to understand the nature of spectral characteristics inside of a hurricane, and serve as motivation for exploring similar spectra for offshore wind-energy applications. We first validate the use of our relatively simple LES set-up by comparison with a more complex LES set-up and a rare dataset of hurricane observations made below 200 m ASL. Then, using high-resolution simulations with the simple LES framework, we perform spectral and coherence analyses of varying wind speeds inside the HBL at heights relevant for offshore wind turbines. We specifically address how turbulence characteristics vary with height and with hurricane mean wind speed.

In Sect. 2.2, we describe the hurricane model configurations and observational dataset used, while in Sect. 2.3, we describe how power spectral density and coherence are calculated using LES data. Section 2.4 presents the results, including suggestions for modified spectral and coherence models for use in three-dimensional wind-field simulators. In Sect. 2.5, we summarize the results and offer suggestions for future research.

## 2.2 DATASETS

### *2.2.1 CLOUD MODEL I (CM1)*

To assess the HBL, we use idealized simulations with the non-hydrostatic, time-dependent, numerical model, Cloud Model 1 (CM1) (Bryan and Rotunno 2009), with two different configurations, detailed below, created for the purposes of assessing turbulent characteristics inside a major hurricane. We use the CM1 model for all simulations herein. The first model configuration, which we refer to as the *Complex* set-up simulates the entire inner core of a hurricane, including the eye, eyewall, and rainbands, but this approach is computationally expensive, and so relatively coarse resolution is used. The second configuration, referred to as the *Simple* set-up, reduces computational expense by simulating only a small portion (approximately 5 km × 5 km) of the hurricane, an approach that allows for higher-resolution simulations so that coherence can be calculated across a theoretical turbine rotor layer. A general comparison of the *Complex* and *Simple* set-ups appears below.

Both the *Complex* and *Simple* set-ups use the same numerical code, which uses Runge-Kutta time integration with fifth-order advection (Wicker and Skamarock 2002). A prognostic subgrid-scale turbulent kinetic energy (TKE) model (i.e., Deardorff-type TKE scheme) is used to parametrize unresolved turbulence (Stevens et al. 1999; Bryan et al. 2017). For all of the simulations, surface ocean waves are not modelled explicitly; rather, the surface roughness is varied as a function of the time-averaged 10-m wind speed ($\overline{U}$), as described in Bryan et al. (2017). Herein, for $\overline{U} \geq 25$ m s$^{-1}$, the roughness length is held constant at 0.0028 m. This parametrization yields a surface friction velocity $u_*$ that varies roughly linear with $\overline{U}$, as suggested by recent observational studies (e.g., Andreas et al. 2012).

### *2.2.2 COMPLEX SET-UP*

For the *Complex* set-up, simulation data were generated by first running an axisymmetric (two-dimensional) configuration of the model for twelve days with a horizontal grid spacing of 1 km and a temporal resolution of 2.5 s to spin-up the quasi-steady state hurricane as in Bryan (2012). Then, time-averaged fields surrounding the time of maximum hurricane intensity (day 10) over a two-day period were used as initial conditions for a three-dimensional LES. Small-amplitude random perturbations (±0.1 K) of potential temperature were used to initiate turbulent, three-dimensional motions in the model, and the model then was integrated for 4 h to fully spin-up turbulent flow. Two additional hours of simulation were used to generate data analyzed herein. For more information about the model set-up, such as the sea-surface temperature and microphysical scheme, see Bryan (2012). The total domain size (i.e., entire hurricane and environment) of the simulation is 3000 km × 3000 km in the horizontal and 25 km in the vertical with increasingly stretched grid spacing away from a central fine-mesh part of the domain (Figure 2.1). The fine-mesh LES domain spans 80 km × 80 km × 3 km centered in the middle of the overall domain. The grid spacing within the fine mesh domain is a constant 62.5 m in the horizontal and 31.25 m in the vertical, and the timestep is 0.375 sec. Data are provided every timestep for 2 h over a 7 × 7 grid (spanning 437.5 m × 437.5 m) at four locations east of the hurricane center (at radii of 20 km, 25 km, 30 km, and 35 km) from the surface to 500 m ASL (Table 2.1). These four locations were chosen so as to provide a range of mean wind speeds (from tropical storm to Category-4 conditions) and to allow for comparison of the *Complex* set-up with the *Simple* set-up discussed in Sect. 2.2.3. We examine data up to heights of 200 m

ASL to explore turbulence characteristics that may be relevant to offshore turbines of varying heights. In the LES domain, the quiescence of the eye, as well as small high-speed gusts in excess of 90 m s$^{-1}$ located outside of the eyewall, are apparent (Figure 2.1); such high-speed gusts have been observed in nature (Stern et al. 2016).

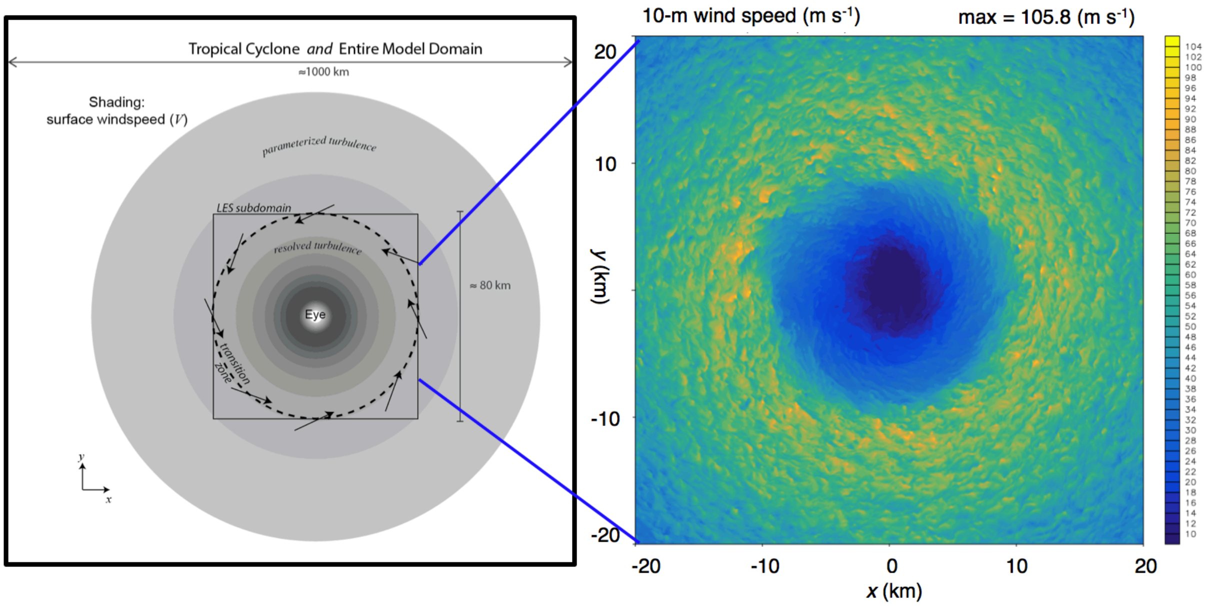

Figure 2.1 *Complex* set-up shown on the left. Instantaneous 10-m wind speed after 6 h of the LES is shown on the right. The data are from the LES domain with a horizontal grid spacing of 62.5 m and a temporal resolution of 0.375 s.

Table 2.1 Summary of the *Complex* (CM1C) and *Simple* (CM1S) set-ups used in the analysis. The abbreviations in column one are formatted so that the first letter represents the *Complex* (C) or *Simple* (S) set-ups while the number represents the horizontal grid spacing of the run. SF10 is a simulation of flight data through the *Simple* set-up domain. Values in column three are the mean horizontal wind speeds at ≈ 10 m ASL. Wind speeds at hub height are approximately 20% greater than those at 10 m ASL. TS is an abbreviation for tropical storm.

| Sim. | Model configuration | Wind speed (m $s^{-1}$) at 10 m ASL | Approx. category | $\Delta t$ (s) | $\Delta x$, $\Delta y$, $\Delta z$ (m) | Radius (km) |
|---|---|---|---|---|---|---|
| C62 | CM1C | ≈57, 43, 41, 30 | 3, 2, 1, TS | 0.375 | $\Delta x$, $\Delta y$ = 62.5<br>$\Delta z$ = 31.25 | 20, 25,<br>30, 35 |
| S62 | CM1S | ≈ 57, 43, 41, 30 | 4, 3, 2, 1 | 0.375 | $\Delta x$, $\Delta y$ = 62.5<br>$\Delta z$ = 31.25 | 20, 25,<br>30, 35 |
| S10 | CM1S | ≈ 63, 47, 23 | 4, 2, TS | 0.1 | $\Delta x$, $\Delta y$ =10<br>$\Delta z$ = 5 | 35, 70,<br>130 |
| SF10 | CM1S, "flight" | ≈ 23 | TS | 0.1 | $\Delta x$, $\Delta y$ =10<br>$\Delta z$ = 5 | 130 |

### 2.2.3 *SIMPLE SET-UP*

The *Simple* set-up does not simulate a full hurricane, but rather is designed to simulate the conditions in a small region of the hurricane (see Figure 2.2) and accounts for the large-scale tendencies associated with a hurricane (e.g., pressure-gradient and centrifugal accelerations) via mesoscale tendency terms, as formulated by Bryan et al. (2017). The *Simple* set-up uses a LES configuration, so the planetary boundary-layer (PBL) parametrization in the model is removed and the subgrid turbulence model described in the Appendix of Bryan et al. (2017) is employed. In addition, to simplify initial conditions and decrease computational expense, the *Simple* set-up does not include moisture and therefore employs no microphysical scheme, unlike the *Complex* set-up. Surface heat fluxes are also neglected (see Bryan et al. 2017) and thus the PBL in these simulations is neutral. As will be shown, wind profiles from the *Simple* set-up compare well to those from the *Complex* set-up (Sect. 2.4.1), suggesting that moisture and surface heat fluxes are not required to create the turbulent conditions. Both set-ups employ periodic lateral boundary conditions, as is common for LES of the PBL, which is justified if the scales of the horizontal variations in the atmosphere are large compared to the horizontal scale of the domain (e.g., Sommeria 1976). Periodic lateral boundary conditions also allow turbulent eddies to be “recycled” through the domain, which obviates the need to specify turbulent fluctuations at lateral boundaries.

For the *Simple* set-up, the initial conditions are specified analytically with a small number of parameters, including: the Coriolis parameter $f$, the wind speed above the boundary layer $V$, the radius from the hurricane center to the *Simple* set-up domain $R$ (see Figure 2.2), and the radial gradient of wind speed above the boundary layer $dV/dR$. The mesoscale tendency terms, which use these parameters, are described in detail in Bryan et al. (2017). For the present study, we include subsidence terms (see Siebesma et al. 2003) except that the minimum vertical velocity $w_{min}$, has a larger amplitude (stated below) and is located at 1 km ASL.

The two set-ups result in greatly different computational expense. Due to the different domain sizes (5.12 km × 5.12 km × 3 km for the *Simple* set-up versus 3000 km × 3000 km × 25 km for the *Complex* set-up) and inclusion of moisture, the *Complex* set-up requires approximately two orders of magnitude more CPU hours than the *Simple* set-up for a simulation using the same horizontal and vertical grid spacing. This great advantage of the *Simple* set-up allows for temporal and spatial resolutions fine enough for calculations of coherence across the turbine rotor layer (i.e., ≤ 30 m for at least two points across a typical blade length). However, the *Simple* set-up is not able to accurately simulate the eyewall of a hurricane, which is dominated by strong mesoscale vertical motions that are not accounted for in the *Simple* framework. Therefore, only locations outside the radius of maximum wind speeds (i.e., outside the hurricane eyewall) can be assessed with the *Simple* set-up. As with the *Complex* set-up, the *Simple* set-up data are provided at high resolution (every timestep) over a small grid at a radius of interest (Table 2.1), see in Figure 2.2. The hurricane-like profiles simulated by the *Simple* set-up are analogous to observations from virtual towers at each location on the grid.

The simulations discussed herein are summarized in Table 2.1. First, we compare simulations from the *Complex* and *Simple* set-ups at the same temporal and spatial resolution, as denoted by C62 and S62, respectively in Table 2.1. This direct comparison employs an idealized simulation of a relatively small, but intense, hurricane, e.g., Hurricane Felix 2007.

Then, to compare with hurricane observations, we ran the *Simple* set-up at a significantly higher spatial and temporal resolution ($\Delta x$ = 10 m, $\Delta t$ = 0.1 s), denoted by S10 in Table 2.1. Data from the first case, at a radius of 130 km (Sect. 2.2.4) are compared to observations collected in Hurricane Isabel of 2003, as described below. Further simulations with $\Delta x$ = 10 m and $\Delta t$ = 0.1 s at two additional radii, 35 km and 70 km, are used to evaluate variations of the power spectral density and coherence as a function of hurricane radius or, essentially, for different mean wind speeds (since wind speed increases as the radius decreases outside of the eye of a given hurricane). For all S10 simulations, high-resolution data over a 21 × 21 grid (200 m × 200 m) from the center of the domain allows calculation of power spectral density at high frequencies to estimate spatial coherence across the turbine rotor layer.

Finally, to compare directly with aircraft observations, data from the S10 simulation at a radius of 130 km were extracted along a fictitious aircraft track moving through space every timestep in a straight line through the *Simple* set-up domain. This approach allows for a fair comparison of the aircraft observations and model results, and ensures that analyzed gust frequencies are consistent in the two datasets. To allow for calculations of mean conditions and variations, we simulated 21 different flights, each separated by 250 m in the model domain, from this simulation denoted as SF10 in Table 2.1.

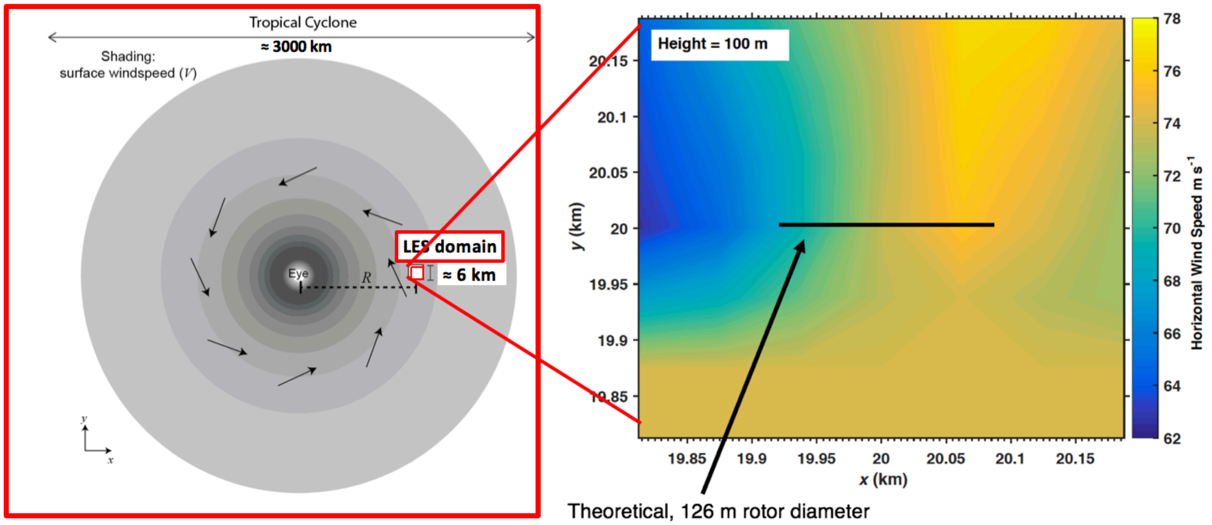

Figure 2.2 *Simple* set-up shown on the left. Instantaneous 100-m horizontal wind speed at a radius of approximately 20 km is shown on the right. The hurricane center is at (0,0). The data are from a LES domain with a horizontal grid spacing of 62.5 m and a temporal resolution of 0.375 s to match that of the *Complex* set-up. The black line represents the theoretical rotor span (NREL 5-MW reference wind turbine), looking down on top of the turbine.

### *2.2.4 OBSERVATIONS*

Both the *Complex* and *Simple* set-ups have been evaluated in other studies (e.g., Richter et al. 2016; Bryan et al. 2017). To test the suitability of the *Simple* set-up to represent turbulent flow in hurricanes, we compare data from the *Simple* set-up to the limited observational data available at turbine height and taken at suitable temporal resolution for power-spectral-density estimates. The sample time series comprises approximately 6 min of wind-velocity observations (Figure 2.3) collected during the Coupled Boundary Layer Air-Sea Transfer (CBLAST) – Hurricane experiment (Black et al. 2007; Zhang et al. 2009; Zhang 2010a). The length of this dataset is one-of-a-kind, because the other CBLAST measurements were taken for a duration of 3 min or less. The data were collected by the NOAA WP-3D Orion aircraft at a temporal resolution of 40 Hz at 194 m above the surface on 12 September 2003 inside Hurricane Isabel, with the storm at Category-5 intensity. The data were collected nearly 130 km away from the storm center, and at this location, the near-surface wind speeds were of tropical storm intensity and no rainbands were present. The virtual tower and mock flights at a radius of 130 km described in Sect. 2.2.3 were designed to simulate the conditions under which these observations were obtained.

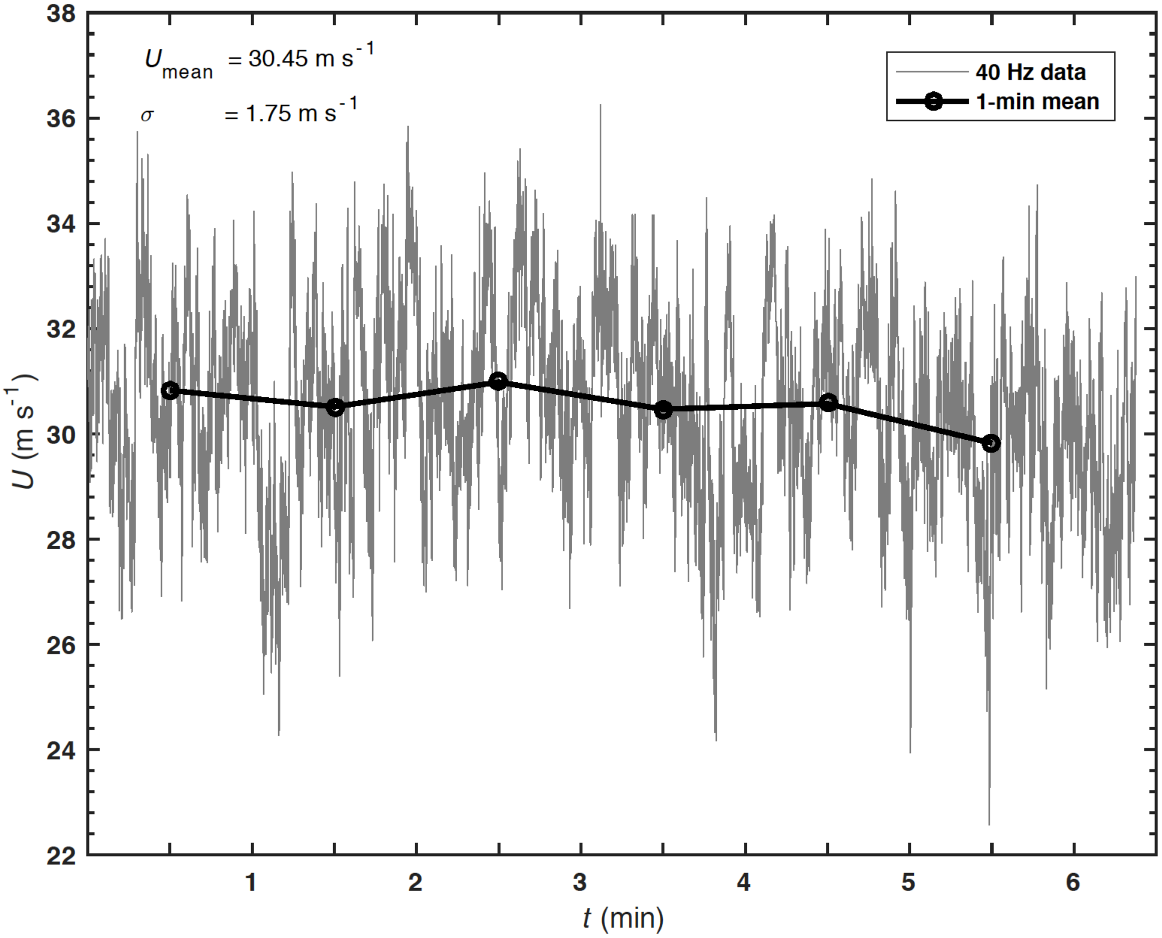

Figure 2.3 Instantaneous (grey) and 1-min average (black) time series of the total horizontal wind speed collected during Hurricane Isabel on 12 September 2003 around 1800 UTC. The standard deviation and mean wind speeds were calculated from the complete time series. Data were collected during the CBLAST experiment at an altitude of 194 m and at a hurricane radius of 130 km.

## 2.3 ANALYSIS METHODS

### *2.3.1 POWER SPECTRAL DENSITY*

To prepare the data and calculate power spectral density, several data processing steps are required. First, the components of the wind velocity are converted to streamwise/along-wind, cross-stream/cross-wind, and vertical components. Hereafter, $u$, $v$, and $w$, are used interchangeably with the above wind-component definitions. Then, to smooth the spectrum and reduce bias, an ensemble average of 50% overlapping, equal-length segments of power spectral density is calculated. The ensemble average consists of 39 samples derived from 2 h of simulation. A 6-min segment of the time series is used here to match the duration of the CBLAST observations. After removing any linear trend, a window function is applied to minimize edge effects (i.e., sharp transitions in the signal) that result in spectral leakage (i.e., high side-lobes). The edge effects occur as artifacts of the underlying periodic assumption of the fast Fourier transform. A Blackman-Harris window function is used, which is a generalization of the Hamming window function that further minimizes side-lobes (Harris 1978).

When the turbulence spectrum in the atmosphere is considered for wind loads, standard spectral models are frequently used. Common spectral models include the empirical Kaimal model (based on observations in a neutrally-stratified PBL, Kaimal et al. 1972) and the theoretical isotropic von Kármán model (assuming homogeneous and isotropic turbulence) (von Kármán and Lin 1951). On average, the HBL is neutrally stable (Powell et al. 2003; Vickery and Skerlj 2005) except at its top (Zhang et al. 2011; Kepert et al. 2015), which is well above turbine-hub height, allowing for comparison with these traditional models.

The IEC 61400-1 (IEC 2007a) standard for the streamwise Kaimal model (Eq. 2.1), incorporates a constant integral scale parameter, $L_u$, equal to 340 m for hub heights > 60 m, and a standard deviation of the horizontal wind speed at hub height, $\sigma$,

$$S_u(f) = \frac{\frac{a\sigma^2 L_u}{V_{hub}}}{\left(b+c\left(\frac{fL_u}{V_{hub}}\right)\right)^{\frac{5}{3}}}, \tag{2.1}$$

where $a$, $b$, and $c$ are coefficients equal to 4, 1, and 6, respectively. $V_{hub}$ is the mean horizontal wind speed at hub height and $f$ is the frequency.

The isotropic von Kármán model (Eq. 2.2) parameters are the integral scale parameter $L_{vk}$, mean horizontal wind speed at hub height $V_{hub}$, frequency $f$, and variance of the wind speed at hub height $\sigma^2$. The integral scale parameter $L_{vk}$, is set to the IEC standard value of 147 m for hub heights > 60 m,

$$S_u(f) = \frac{a\sigma^2 L_{vk}/V_{hub}}{\left(b+c\left(\frac{fL_{vk}}{V_{hub}}\right)^2\right)^{\frac{5}{6}}}, \tag{2.2}$$

where $a$, $b$, and $c$ are coefficients equal to 4, 1, and 71, respectively.

### 2.3.2 *SPECTRAL COHERENCE*

Spectral coherence (Eq. 2.3) is a function of frequency with a value between zero and one. It indicates how well two spatially-separated time series are correlated. The square of the cross-power spectral density (*CPSD*) function between two time series, separated by some distance, is normalized by the product of the auto-power spectral densities (*PSD*) of each of the two time series $x_1$ and $x_2$ (Larsen and Hansen 2004; Saranyasoontorn et al. 2004),

$$Coh(f)^2 = \frac{|CPSD_{x1x2}(f)|^2}{PSD_{x1}(f) * PSD_{x2}(f)}, \tag{2.3}$$

where $f$ is frequency in Hertz and $x$ can be the $u$, $v$, or $w$ velocity component of the flow. Each wind-velocity component is treated separately. For example, if $x_1$ is the streamwise component at one location, $x_2$ is the streamwise component at a different location; two different wind-velocity components are not included in the same calculation of $Coh(f)^2$.

For the S10 simulations, coherence is calculated in a 21 × 21 grid centered at the location of a theoretical offshore turbine with the dimensions of the NREL 5-MW reference wind turbine (Jonkman et al. 2009). This turbine is a three-bladed, upwind turbine with a hub height of 90 m and rotor diameter of 126 m. Since the model does not directly represent turbines, the analysis is based on what the power spectral density and coherence would be if the turbine were in place (i.e., flow at hub height and across the rotor layer). The coherence calculations capture the turbulent flow experienced by the turbine in the rotor-swept area but do not consider downwind wake effects. A model of the wind turbine itself, such as in Mirocha et al. (2014) and Aitken et al. (2014), would be required to consider wake effects. Coherence calculated across various lengths of the turbine structure is examined below.

The commonly-used empirical model for horizontal and vertical separations of coherence is the IEC exponential coherence model (Thresher et al. 1981; IEC 2007a),

$$Coh(f)^2 = \left(\exp\left[-a\sqrt{\left(\frac{fS}{V_{hub}}\right)^2 + \left(\frac{bS}{L_c}\right)^2}\ \right]\right)^2, \tag{2.4}$$

where $L_c$ is the coherence scale parameter, specified by the IEC as 340 m for wind turbines with a hub height > 60 m, $S$ is the spatial separation between two points of interest along the turbine, $f$ is frequency, and $V_{hub}$ is the mean horizontal wind speed at hub height. The coefficients $a$ and $b$ are equal to 12 and 0.12, respectively, according to the IEC standard.

## 2.4 RESULTS

### *2.4.1 COMPARISON BETWEEN COMPLEX AND SIMPLE SET-UPS*

Because the *Complex* set-up simulates all aspects of a hurricane (including the eye and eyewall) and includes moisture, it would ideally be used for all analyses in our study. However, the *Complex* set-up is two orders of magnitude more computationally expensive than the *Simple* set-up, which limits the resolution in practice ($\Delta x = 62.5$, $\Delta z = 31.25$ m, $\Delta t = 0.375$ s herein). Therefore, the bulk of our analysis below uses the *Simple* set-up to allow for higher-resolution simulations ($\Delta x = 10$ m, $\Delta z = 5$ m, $\Delta t = 0.1$ s) and also allows for larger radii than the *Complex* set-up (for which the fine-mesh domain spans only 80 km × 80 km). To establish the utility of the *Simple* set-up to represent the complex nature of wind conditions in a full hurricane, we first compare wind speed, variance, and power spectra from a *Simple* set-up simulation to those of a *Complex* set-up simulation (i.e. C62 and S62 simulations as listed in Table 2.1).

Normalized average total horizontal wind speed and total horizontal variance for both C62 and S62 simulations are compared at three radii of the modelled hurricane (Figure 2.4). Normalized wind-speed and variance profiles from the *Simple* set-up simulation compare favorably to those in the *Complex* set-up simulation at 25 km (Figure 2.4a, d) and 30 km (Figure 2.4b, e), in the sense that the shape of the wind-speed profiles is similar and the wind speed and variance are within 15% at all heights. At a radius of 35 km (Figure 2.4c, f), the S62 wind speeds are consistently less than those in the C62 wind profiles, by as much as 46%, although, data from the *Simple* set-up are very sensitive to model parameters (see Sect 3.2 of Bryan et al. 2017), suggesting that the parameters for the S62 simulation could be better "tuned" to match the C62 case. In all cases shown in Figure 2.4, differences in the mean wind speed increase with height, while differences in the variance are largest between 50 and 150 m. These differences in variance suggest differences in the power spectral density, although we have not found any significant differences between the power spectra in the two set-ups (Figure 2.5).

The dominant length scales associated with the normalized frequency at the peak magnitude of the normalized spectra are similar between the two set-ups. The dominant length scale is ≈ 3, 2, and 3.5 km at 50, 100, and 200 m ASL, respectively for the *Simple* set-up; for the *Complex* set-up, the dominant length scales are ≈ 1.5, 1, and 3 km for the same altitudes. The mean wind speed at the radius shown in Figure 2.5 (i.e., $R$ = 20 km) is roughly 2-3 m $s^{-1}$ greater in the *Simple* set-up than in the *Complex* set-up, which contributes to the slightly larger length scales in the *Simple* set-up than in the *Complex* set-up.

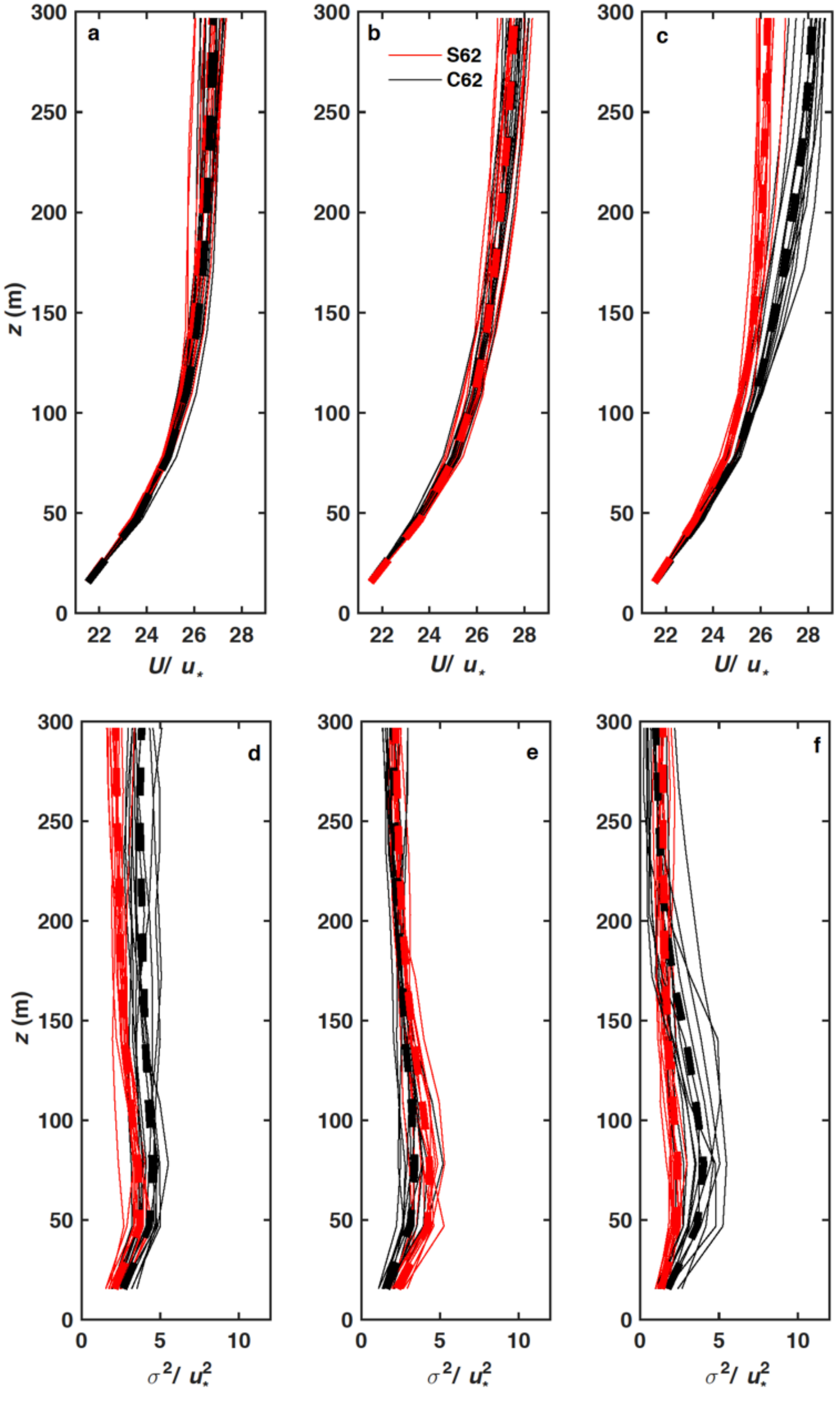

Figure 2.4 Profiles of the average total horizontal wind speed for C62 (black) and S62 (red) simulations at radii of, a) 25 km, b) 30 km, and c) 35 km normalized by friction velocity, $u_*$. Profiles of the normalized average resolved-scale variance of the total horizontal wind speed at radii of, d) 25 km, e) 30 km, and f) 35 km are also shown. Thick, dashed lines are 2-h averages while thin, solid lines are 10-min averages.

Comparisons between normalized power spectral density from the S62 and C62 simulations at three different altitudes relevant to the theoretical turbine also show good agreement in magnitude and shape; the average percentage difference between the two spectra is $< 1\%$ for each altitude (Figure 2.5). Spectra from both set-ups agree well at all altitudes; both follow the Kolmogorov $-5/3$ power law in the inertial subrange (beginning at a normalized frequency of $\approx 0.03$, 0.1, and 0.2 for an altitude of 50, 100, and 200 m ASL, respectively) with a rapid drop-off at higher frequencies due to the model's numerical schemes (e.g., Bryan et al. 2017).

To resolve higher frequencies (smaller wavelengths), the spatial and temporal resolutions need to be increased, and the ability to use increased resolution is the main advantage of the the *Simple* set-up. Results in this section demonstrate that the *Simple* set-up produces qualitatively similar wind-speed and variance profiles as the *Complex* set-up (Figure 2.4), and yields very similar spectra (Figure 2.5), providing confidence that the *Simple* set-up faithfully represents turbulent conditions in more complex hurricane simulations.

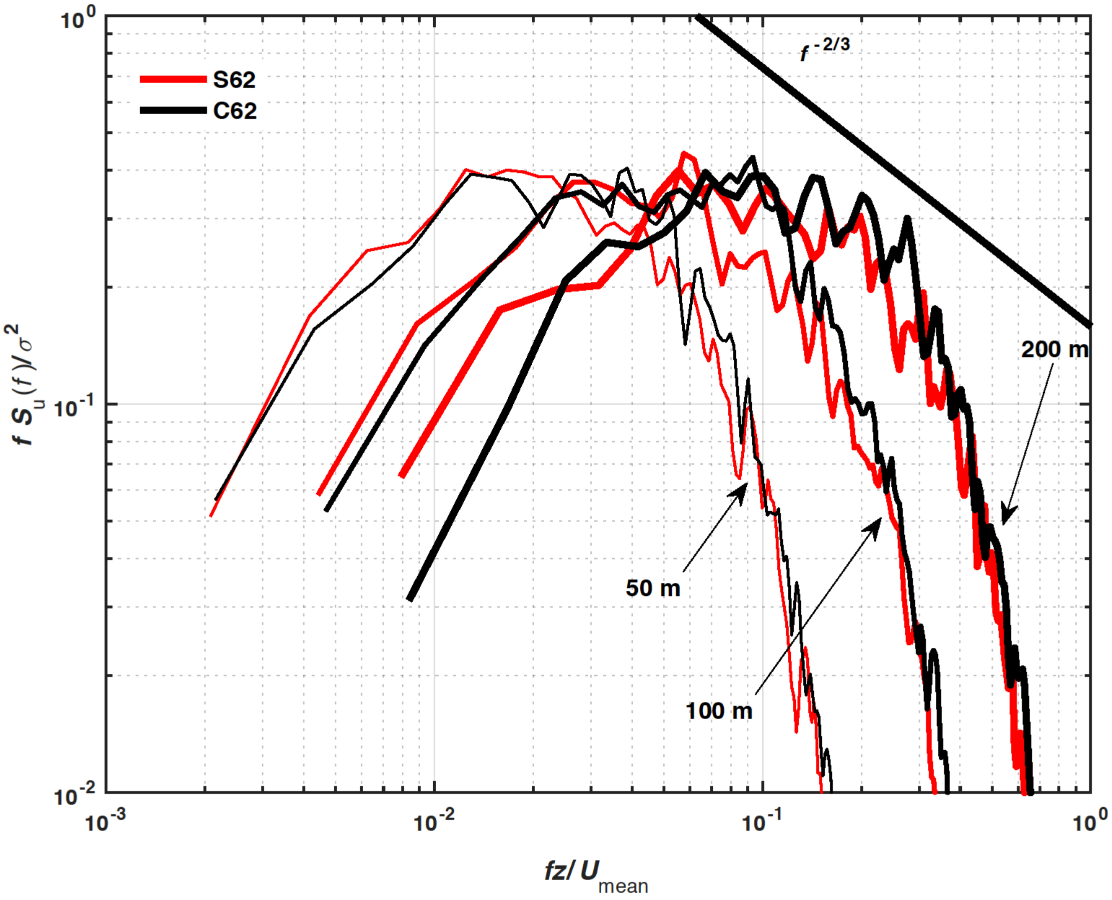

Figure 2.5 Normalized power spectral density of the streamwise velocity component from S62 (red) and C62 (black) simulations at a hurricane radius of 20 km and at three different altitudes pertinent to wind-turbine heights (50, 100, and 200 m).

### 2.4.2 *SIMPLE SET-UP SIMULATIONS COMPARED TO HURRICANE OBSERVATIONS*

To further evaluate the *Simple* set-up, we now compare simulations with hurricane observations collected at a hurricane radius of 130 km. Extended best-track hurricane wind-speed and radius data (Demuth et al. 2006) and analyses performed by Zhang and Drennan (their Fig. 2b, 2012) of Hurricane Isabel (2003) helped us determine appropriate model parameters (Table 2.2) for the *Simple* set-up simulation, for comparison to the CBLAST observations of Hurricane Isabel. The mean horizontal wind speed and standard deviation from 21 mock flights through the *Simple* set-up domain are 30 m s$^{-1}$ and 1.6 m s$^{-1}$, respectively, values that are within 1 m s$^{-1}$ of those calculated for the CBLAST observations (see Figure 2.3). The spectra from the CBLAST observations and from the 21 mock flights in Figure 2.3 are smoothed to better explore agreement between the observations and simulated results. We block-average the spectra using 100 equally-spaced, non-overlapping bins of the logarithm of the frequency (Blackman and Tukey 1959; Piper and Lundquist 2004).

Table 2.2 Model parameters for the *Simple* set-up simulations of Hurricane Isabel (2003). The SF10 mock flights were directly compared to CBLAST flight observations of Hurricane Isabel at 1800 UTC 12 September 2003. The mock flights were flown into the mean wind (south-south-east) with a fixed ground speed of 140 m s$^{-1}$, the mean wind speed of the P3 aircraft that collected data during the CBLAST experiment.

| Simulation | $f$ (s$^{-1}$) | $V$ (m s$^{-1}$) | $R$ (km) | $dV/dR$ (s$^{-1}$) | $w_{min}$ (m s$^{-1}$) |
|---|---|---|---|---|---|
| SF10, TS | $5 \times 10^{-5}$ | 37 | 130 | $-2 \times 10^{-4}$ | $-1.0 \times 10^{-2}$ |
| S10, TS | $5 \times 10^{-5}$ | 37 | 130 | $-2 \times 10^{-4}$ | $-1.0 \times 10^{-2}$ |
| S10, Cat 2 | $5 \times 10^{-5}$ | 72 | 70 | $-8.2 \times 10^{-4}$ | $-2.5 \times 10^{-2}$ |
| S10, Cat 4 | $5 \times 10^{-5}$ | 90 | 35 | $-2 \times 10^{-3}$ | $-5.0 \times 10^{-2}$ |

The comparison of the power spectral density for each wind-velocity component calculated from CBLAST observations and that from the mock flights from the *Simple* set-up exhibits good agreement (Figure 2.6). For the streamwise and vertical velocity components, the observations fall within the bounds of the minimum and maximum power spectral density for all 21 mock flights denoted by the light-blue shaded region in Figure 2.6. The average vertical power-spectral-density curve from the model follows the observations remarkably well at frequencies below 2 Hz. For the cross-stream component, the model mock flights do not match the power spectral density from observations for frequencies < 0.02 Hz. This discrepancy may be because the observations are from one flight only and one time series, and a flight that may have sampled a mesoscale velocity fluctuation that cannot be represented in the *Simple* set-up, e.g., as related to rainbands.

Also, with more data, the observed power spectral density of the cross-stream component may align with the simulated “flights”. Nonetheless, for all components, the *Simple* set-up produces a realistic inertial subrange (i.e., the range of frequencies where turbulence energy is neither produced nor dissipated, but rather transported to smaller scales). Both power-spectral-density curves from the HBL observations and simulations vary according to the Kolmogorov power law, $f^{-5/3}$, in the inertial subrange. The simulated spectra for all wind-velocity components begin to deviate from the Kolmogorov power law for frequencies $> 2$ Hz, as expected from LES (which does not simulate all scales of a turbulent flow). The details of the “drop-off” in power are related to the model’s numerical methods, which affect scales $< 6\Delta x$ in the model (e.g., Bryan et al. 2003). In this case, the drop-off begins at roughly 2 Hz, corresponding to a frequency $f = u_a/(6\Delta x)$, where $u_a = 120$ m s$^{-1}$ corresponds roughly to the airspeed of the mock airplanes.

This agreement in the shape, magnitude, and inertial subrange of the power-spectral-density curve of the model data suggests that the *Simple* set-up produces realistic turbulent fluctuations in hurricanes, and thus model data can be used further to investigate coherence inside the HBL, where adequate observations to calculate coherence are unavailable. Subsequent analysis is performed with the S10 simulation data, using stationary virtual towers.

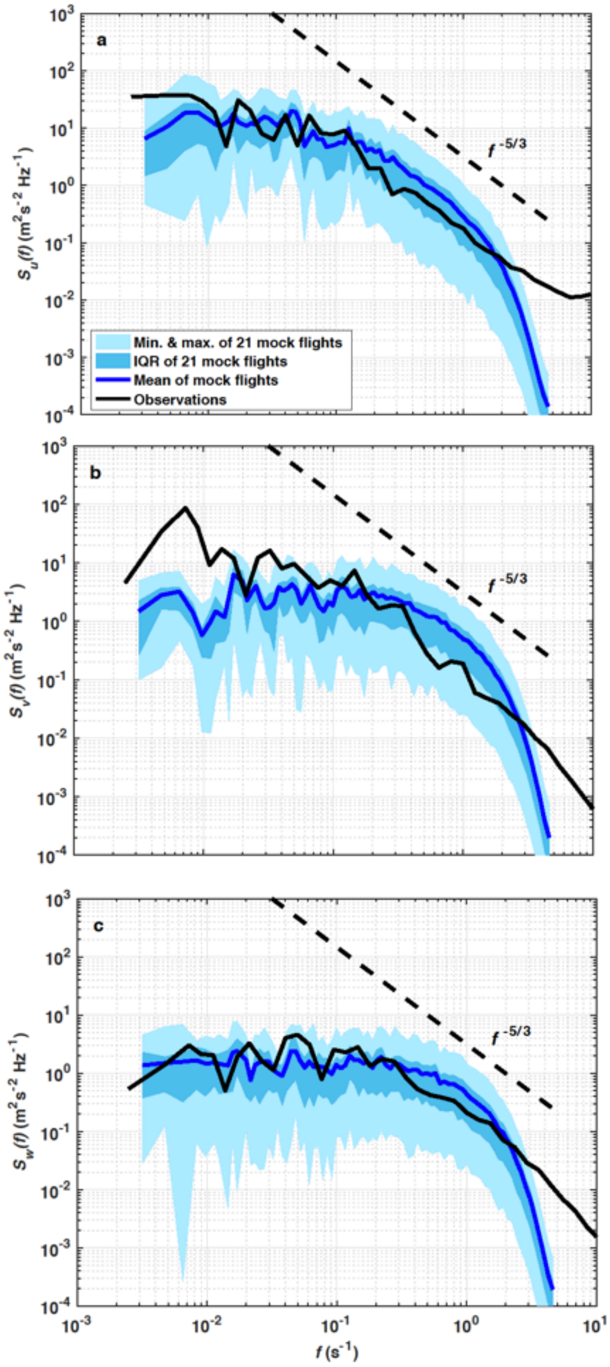

Figure 2.6 Comparison of power spectral density between the SF10 simulation (blue line) at 194 m altitude and the CBLAST observations (black line) at 194 m altitude at a radius of 130 km from the storm center. The streamwise power spectral density is shown in a), the cross-stream in b), and the vertical power spectral density in c). The dark blue line is the average power spectral density calculated from 21 mock flights, the medium-blue-shaded region represents the interquartile range (IQR) and the light-shaded region represents the maximum and minimum of all 21 power spectral densities.

### *2.4.3 COMPARISON OF LES-DERIVED POWER SPECTRAL DENSITY TO ESTABLISHED SPECTRA*

The power spectral density from the *Simple* set-up can be compared to the Kaimal and von Kármán spectra detailed in Sect. 2.3.1. For this comparison, the variables $V_{hub}$ and $\sigma^2$ for the Kaimal (Eq. 2.1) and von Kármán (Eq. 2.2) spectral models were calculated using a 2-h mean of the horizontal wind speed produced from the entire time series of the S10 simulations at 100 m ASL (near hub height for the NREL 5-MW turbine). The empirical and theoretical spectra are then compared to the three S10 power-spectral-density curves representing mean wind speeds corresponding to a tropical storm ($R$ = 130 km), a Category-2 condition ($R$ = 70 km), and a Category-4 condition ($R$ = 35 km) (Figure 2.7). Because the Kaimal and von Kármán models are provided $V_{hub}$, and $\sigma^2$ from the *Simple* set-up, the spectral models should match the power-spectral-density curves from the S10 simulations if the spectral models represent turbulence characteristics of the HBL.

Both the Kaimal and von Kármán spectral curves slightly underestimate the power spectral density at most frequencies (Figure 2.7). Analyses at other altitudes (not shown) show the same result, up to at least 200 m ASL. These differences may occur because the wind conditions in the HBL are more variable than in the onshore, neutral PBL from which these curves were derived. This result is consistent with onshore-hurricane observations (Yu et al. 2008). Yu et al. (2008) found that the magnitude of the streamwise power spectral density of flow from the sea was greater than the power spectral density of flow originating over open terrain based on tower measurements 5 m and 10 m above the surface. However, the increased magnitude of the power-spectral-density curve in the sea-to-land case in Yu et al. (2008) could be attributed to increased turbulent energy induced by waves breaking and shoaling on approach to the coastline.

The greatest difference between the simulated spectra and the theoretical curves occurs in the inertial subrange, where the spectral magnitude decreases according to Kolmogorov's theory (shown as the dashed-black lines in Figure 2.7). The power in the inertial subrange of the simulated spectrum is also approximately two times greater than that in the observed spectrum for the TS case. This increase in energy for the simulated flow in the inertial region implies that TKE dissipation $\varepsilon$ and the friction velocity $u_*$ are high (i.e., $u_*$ ranges between 1-3 m s$^{-1}$). However, $u_*$ calculated from the TKE dissipation within the inertial subrange for each case according to Eqs. 2.5 and 2.6 is consistent with $u_*$ calculated from the turbulence parametrization scheme,

$$\varepsilon = \alpha_u^{-\frac{3}{2}} 2\pi f U^{-1} [f S_u(f)]^{\frac{3}{2}}, \tag{2.5}$$

where $\varepsilon$ is the rate of dissipation of TKE, $U$ is the mean wind speed, $S_u$ is the streamwise power spectral density, $f$ is the frequency, and $\alpha_u$ is the one-dimensional Kolmogorov constant (= 0.53) for the streamwise component, versus

$$u_*^3 = \varepsilon \kappa z, \tag{2.6}$$

where $z$ is the altitude and $\kappa$ is the von Kármán constant (= 0.4).

For the TS case (Figure 2.7a), $u_*$ calculated from the spectra is 1.08 m s$^{-1}$ and $u_*$ from the turbulence scheme is 1.06 m s$^{-1}$. Similar results between the calculated $u_*$ and the model $u_*$ were also found for the other two cases: ≈ 2 m s$^{-1}$ for the Category-2 case and 3 m s$^{-1}$ for the Category-4 case. These $u_*$ values are consistent with recent observations (Andreas et al. 2012; Bell et al. 2012). Additionally, increases in $u_*$ (and $\varepsilon$) with hurricane wind speed have been observed (Zhang 2010b). These results provide confidence that the larger magnitudes of power spectral density within the inertial subrange of the simulated data are accurate.

Compared to the Kaimal and von Kármán curves, the frequency of peak power in the S10 power-spectral-density curves is also shifted to higher frequencies for all three storm examples, in agreement with Zhang (2010a). The normalized frequency of the peak power-spectral-density curve for all storm examples (blue lines in Figure 2.7), is approximately 1.5 to three times greater than that for the Kaimal curve and up to 2.5 times greater than for the von Kármán curve. This shift suggests that eddies that contribute the most turbulent energy to the HBL are of a smaller wavelength than in non-hurricane conditions where the empirical and theoretical curves apply.

Therefore, adjustments can be made to these spectral models to better represent the turbulent nature of the HBL. To account for the greater magnitude of power spectral density at most frequencies, and the shift in peak power to higher frequencies in the HBL, the new suggested spectral model follows the general structure of the Kaimal relation (Eq. 2.1), but with modified coefficients. We estimated the coefficients for each storm category (Table 2.3) by iterative least-squares estimation of a non-linear regression, given initial values corresponding to the selected coefficients used in Eq. 2.1 (described below) and fitting only for normalized frequencies from 0.005 to $\approx 0.35$ (because the LES model inherently loses power at higher frequencies).

Since the power-spectral-density curves from the S10 simulation (Figure 2.7) are larger in magnitude than the Kaimal curve, except at normalized frequencies $< 10^{-1}$ Hz in the TS case, and the peak frequency is also offset from that of the Kaimal curve, we only need to adjust the coefficients that affect the magnitude and location of the peak of the spectrum. For the Kaimal equation, the coefficient $a$ in Eq. 2.1 controls the magnitude of the spectrum; an increase in the coefficient produces an increase in the spectrum magnitude at all frequencies. The coefficient, $b$ in Eq. 2.1, controls the location of the peak frequency; an increase causes the peak energy of the spectrum to shift to higher frequencies. The final coefficient, $c$ in Eq. 2.1, has the same effect as coefficient $b$, but an increase in coefficient $c$ results in a shift of the peak energy to lower frequencies. Here, we chose to determine the best-fit for coefficients $a$ and $b$ while maintaining coefficient $c$ the same as that used in Eq. 2.1.

The same values for $V_{hub}$ and $\sigma^2$ used in Eq. 2.1 were used in the regression analyses for each corresponding hurricane case; the values were calculated from the entire time series, and so truncation did not affect these values. We tested different length scales ranging from 180 m to 450 m, which are observed hurricane length scales (Yu et al. 2008). We did not see any notable differences in the non-linear fits, so we chose to keep the length scale the same as that used in the IEC standard, 340 m, which also falls within the range of length scales reported by Yu et al. (2008). The non-linear fits (black curves in Figure 2.7a, Figure 2.7b, and Figure 2.7c) follow the normalized power spectrum of the HBL while providing simple adjustments to the commonly-used Kaimal spectrum that can be implemented in a straight-forward way in wind-field simulators.

Table 2.3 Coefficients for the Kaimal spectra (Eq. 2.1) as they are defined in the IEC standard, and as calculated from LES of three different hurricane intensities. The recommended coefficients, based on a general fit for a range of tropical storms and hurricane intensities, are also shown.

| | IEC | TS | Category 2 | Category 4 | Recommended |
|---|---|---|---|---|---|
| $a$ | 4 | 11 | 6.7 | 6 | 8.7 |
| $b$ | 1 | 2.7 | 1.6 | 2 | 2 |
| $c$ | 6 | 6 | 6 | 6 | 6 |

Based on the coefficients in Table 2.3, we note that the power spectral density is most different for the TS case compared to the IEC Kaimal coefficients, and also when the TS case is compared to the other two cases. The coefficients derived from the non-linear regression for the Category-2 and Category-4 cases are essentially the same, suggesting similar turbulence characteristics for hurricanes spanning Categories 2-4. Tests for load models such as TURBSIM would have to be conducted to determine if the coefficients in the TS case differ enough to produce significant variations in the overall turbulence intensities compared to the coefficients used in the Category-2 and -4 cases. Slightly better fits are achieved with wind-speed-specific parameters, but for general application, we suggest using the coefficients in the “Recommended” column in Table 2.3. for the modified power spectral density, as these coefficients were determined from a non-linear regression using all three storm categories (shown as the red curves in Figure 2.7). For all storm categories, the root-mean-square errors calculated between the simulated HBL spectra and the Kaimal spectra were reduced by ≈ 42 – 63% by using the coefficients in the “Recommended” column in Table 2.3 instead of the IEC coefficients for the Kaimal curve. Similar results were found for altitudes of 50 m and 200 m ASL (not shown).

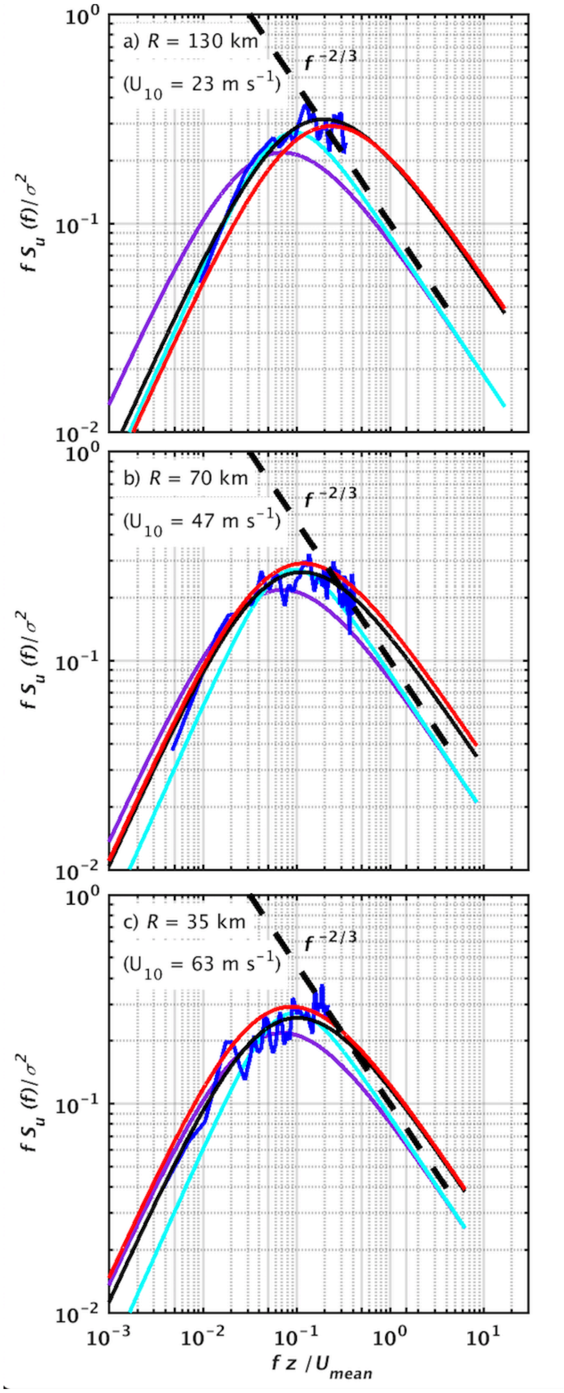

Figure 2.7 Normalized power spectral density of the streamwise velocity component at an altitude of 100 m for the, a) TS, b) Category-2, and c) Category-4 cases. The normalized average power spectral density from the *Simple* set-up at 10 m horizontal grid spacing (blue), Kaimal model (purple), von Kármán model (cyan), the best-fit line of the power spectrum from the *Simple* set-up (black-solid) for each storm intensity, and the general power-spectral-density fit (red) are shown. The Kolmogorov power law (black-dashed) is also shown to reveal the inertial subrange. The mean wind speed at 10 m ASL for each case is also displayed.

### *2.4.4 FLOW VARIABILITY IN THE HBL*

To explore the variability of streamwise power spectral density in the HBL at different hurricane radii (or, essentially, for different mean wind speeds in a given hurricane), we highlight features of the power spectral density as a function of altitude and frequency (Figure 2.8). In the HBL, as simulated here, the peak magnitude of the power spectral density occurs at altitudes $< 100$ m (Figure 2.8) for all three storm intensities. Recall that the NREL 5-MW turbine-hub height is 90 m and the rotor layer spans altitudes from 15 m to 165 m. Thus, dominant energy in the flow occurs at lower reaches of the turbine, which might lead to increased loading at the base of the tower and outer part of the blades via bending.

Additionally, the peak of the power spectral density shifts to higher frequencies as radius decreases. In other words, higher frequency structures dominate the energy in the turbulent flow as one moves closer to the hurricane eyewall. A dependence of peak power spectral density on hurricane intensity is also visible as a function of altitude: as the radius decreases (i.e., wind speed increases, excluding the eye), the vertical extent of the peak power increases. The Category-4 case shows that the location of the peak power (yellow contours in Figure 2.8) in the flow exceeds 150 m ASL, potentially causing significant loading across the entire turbine.

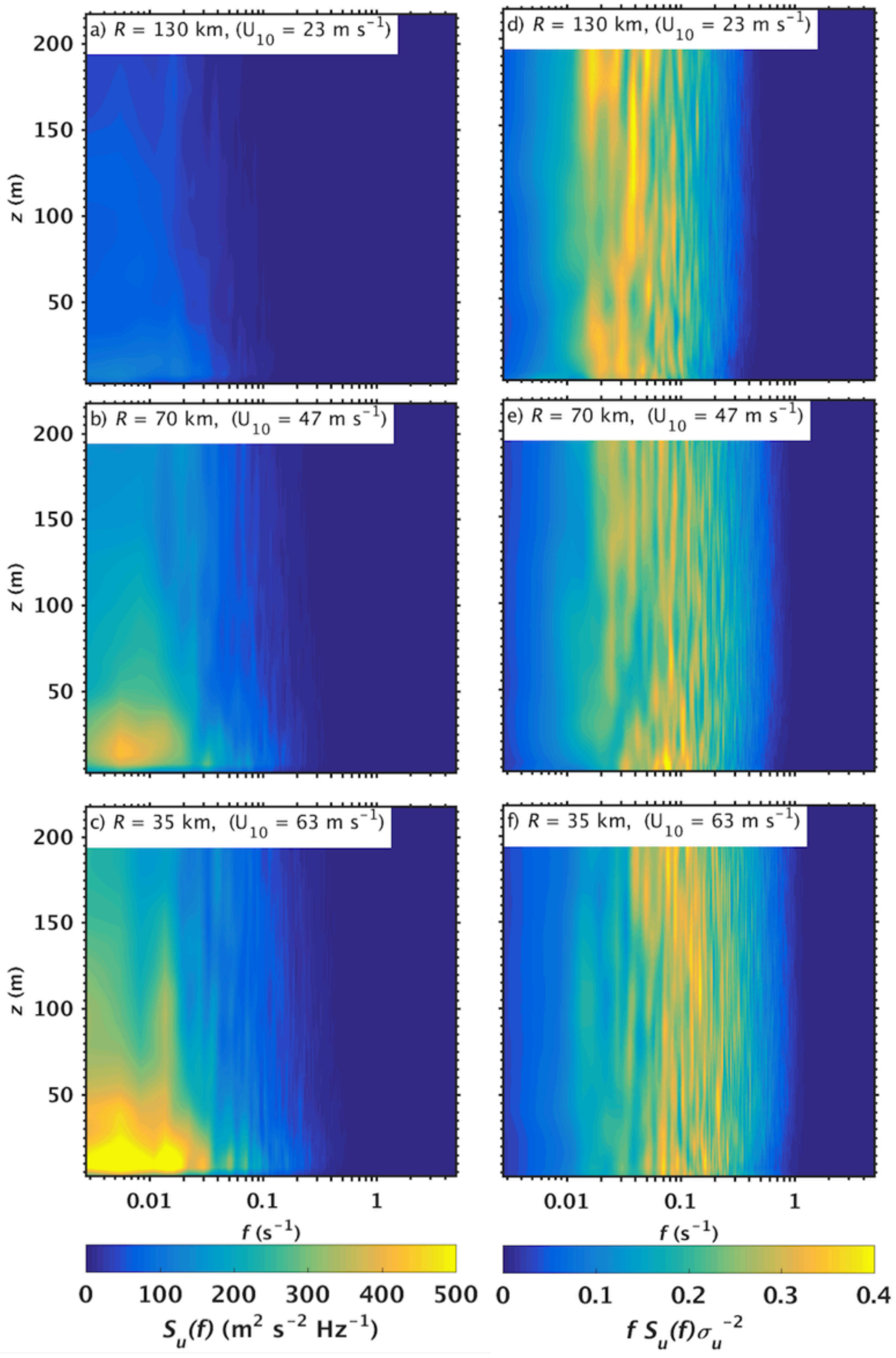

Figure 2.8 Contours of the non-normalized (left column) and normalized (right column) power spectral density of the streamwise velocity component of the *Simple* set-up with a horizontal spacing of 10 m. Three different hurricane radii are shown to represent tropical storm (a, d), Category-2 (b, e), and Category-4 (c, f) intensities. The mean wind speed at 10 m ASL for each case is also displayed.

When normalized by frequency and the variance of the streamwise velocity component (Figure 2.8d-f), the peak power spans the entire vertical extent of the turbine at all radii shown. The dependence of the peak energy on frequency is also apparent. At radii closer to the eyewall (e.g., for higher wind speeds, Figure 2.8e, f), the normalized frequencies that dominate the energy in the flow are higher (up to 0.4) than the contributing frequencies (up to 0.15) at the larger radii (e.g., TS case). This result is consistent with the results shown for the non-normalized power spectral densities in Figure 2.8a-c, which show that higher frequency features contribute larger proportions of energy to the turbulent flow near the eyewall than at large radii.

### *2.4.5 COHERENCE IN THE HBL*

Because of the presence of boundary-layer rolls (Wurman and Winslow 1998; Nolan 2005) and the overall structure of hurricanes (e.g., eye, eyewall, rainbands), the HBL is inherently inhomogeneous. Turbulent flow in contact with an offshore wind turbine varies over different portions of the turbine, including the rotor-swept area. Analysis of coherence at points of interest on a turbine provides information on how turbulence within the HBL changes over the turbine structure, influencing loads like bending moments. In addition, coherence is an essential component in three-dimensional wind-field simulators, because it describes how turbulence is correlated as a function of spatial separation. Although established models for coherence are codified in design standards (i.e., IEC 61400-1, 2007), limited observational studies suggest that coherence is more widely variable than assumed in these standards (Saranyasoontorn et al. 2004).

To assess spatial coherence in the HBL, we calculate coherence across the 21 × 21 (200 m × 200 m) subdomain of the S10 simulation. We assume that a theoretical turbine is located at the far downwind end of this domain so that coherence across the entire rotor layer can be calculated. Eddies within the flow that are approximately the length of the turbine blade and that exhibit high coherence across this length can cause increased damage-equivalent loads on turbine mechanical components.

Our simulations suggest that the HBL is highly coherent. At a radius of 130 km and horizontal separations of 10 m (Figure 2.9a), the flow is highly coherent (≥ 0.6) at all altitudes and at frequencies as high as 0.2 Hz. For horizontal separations < 20 m (Figure 2.9a-b), the flow is highly coherent at all altitudes < 210 m ASL and for all frequencies < 0.05 Hz. Therefore, at hub height, flow is highly coherent across at least one-third the length of the theoretical turbine blade (≈ 63 m) for a range of frequencies spanning two orders of magnitude. At 100 m ASL, separations as large as 40 m produce high coherence values for frequencies < 0.02 Hz. Further, flow remains highly coherent at a wider range of frequencies at altitudes > 50 m compared to the flow at altitudes close to the surface. Turbine designers should consider the possibility of smaller eddies existing near the foundation of the turbine and larger eddies existing near hub height when designing offshore turbines for hurricane-prone regions.

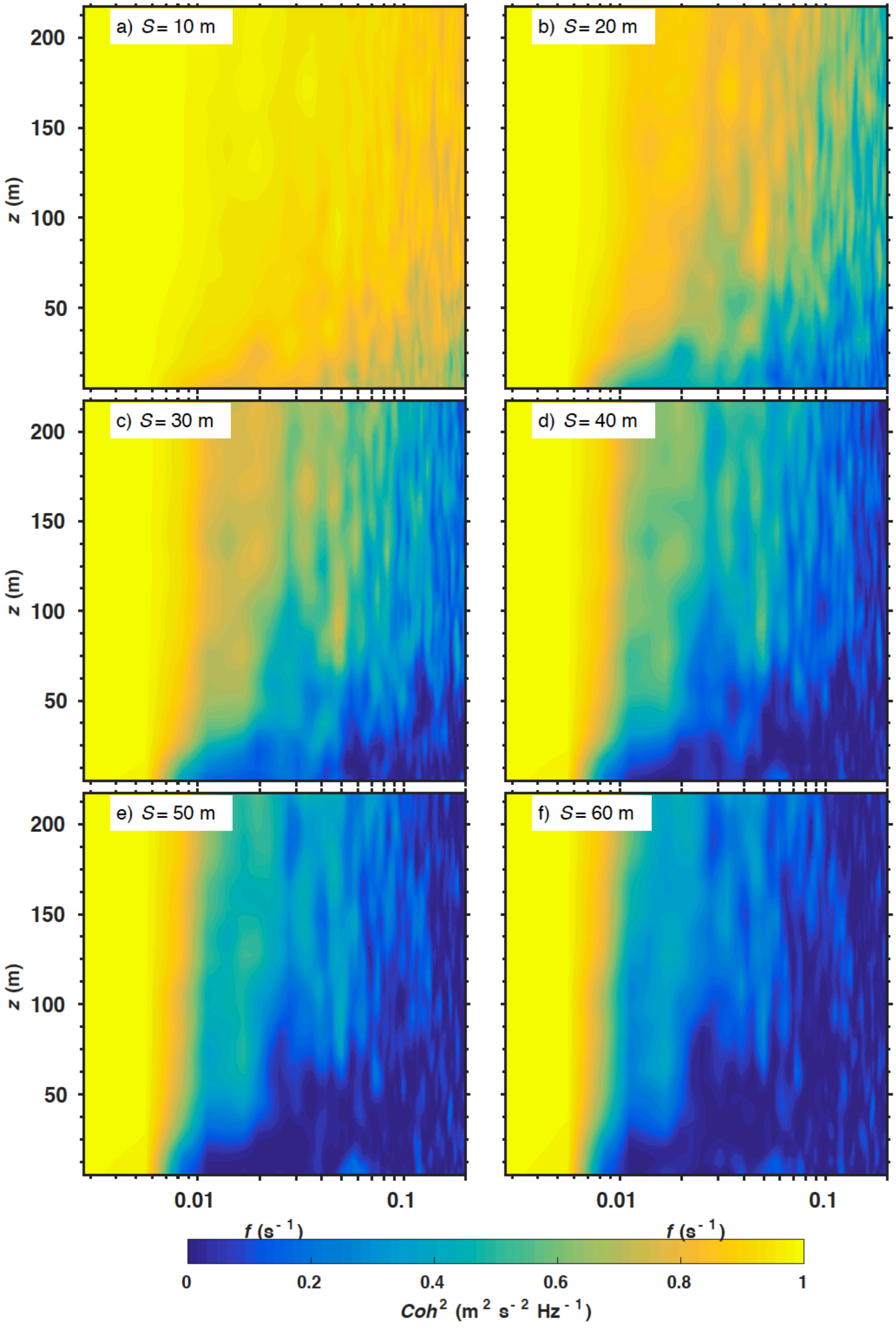

Figure 2.9 Contours of spatial coherence of the streamwise velocity component at six different horizontal separations, a) 10 m , b) 20 m, c) 30 m, d) 40 m, e) 50 m, and f) 60 m across the theoretical turbine. Data from the S10 simulation correspond to a radius of 130 km from the centre of the hurricane. The wind speeds at this radius represent a tropical storm case.

Coherence in the HBL is not only a function of frequency and altitude, but also of hurricane intensity. At a radius of 70 km (Figure 2.10) and 35 km (Figure 2.11), corresponding to Category-2 and Category-4 wind speeds, respectively, the coherence is larger than that in the tropical storm case for all separations and frequencies (Figure 2.9). The wind velocity in the HBL is so coherent in the strong hurricane cases that at 100 m ASL, the turbulence remains highly coherent ($\geq 0.6$) for separations as large as 60 m for frequencies as high as 0.05 Hz (Category-2 case) and 0.07 Hz (Category-4 case). This separation length is roughly the size of a typical turbine blade.

The increase in coherence from tropical storm intensity to that of Category 2 is more drastic than the increase in coherence from Category-2 to Category-4 intensity. This behavior is consistent with the results in Table 2.3, which showed that the modified-Kaimal power-spectral-density curves fit to the Category-2 and -4 cases were essentially the same. Conversely, differences in coherence between the two hurricane categories and the tropical storm case are evident. These results suggest that once a certain hurricane intensity is reached, the turbulence may be predicted with one set of turbulence curves rather than separate curves for every hurricane category.

As separation increases, coherence decreases for the highest frequencies in the flow, presumably because dominant eddy size becomes smaller than the separation length. Saranyasoontorn et al. (2004) also found that the coherence decreased as separation increased, but in their case, the coherence decreased to non-significant values at separations < 15 m opposed to 60-m separations in our cases. This difference may be related to the 10-m grid resolution of our numerical model, but the prevalence of roll vortices in the HBL (discussed below) may produce larger coherence in the HBL as compared with onshore and non-hurricane conditions.

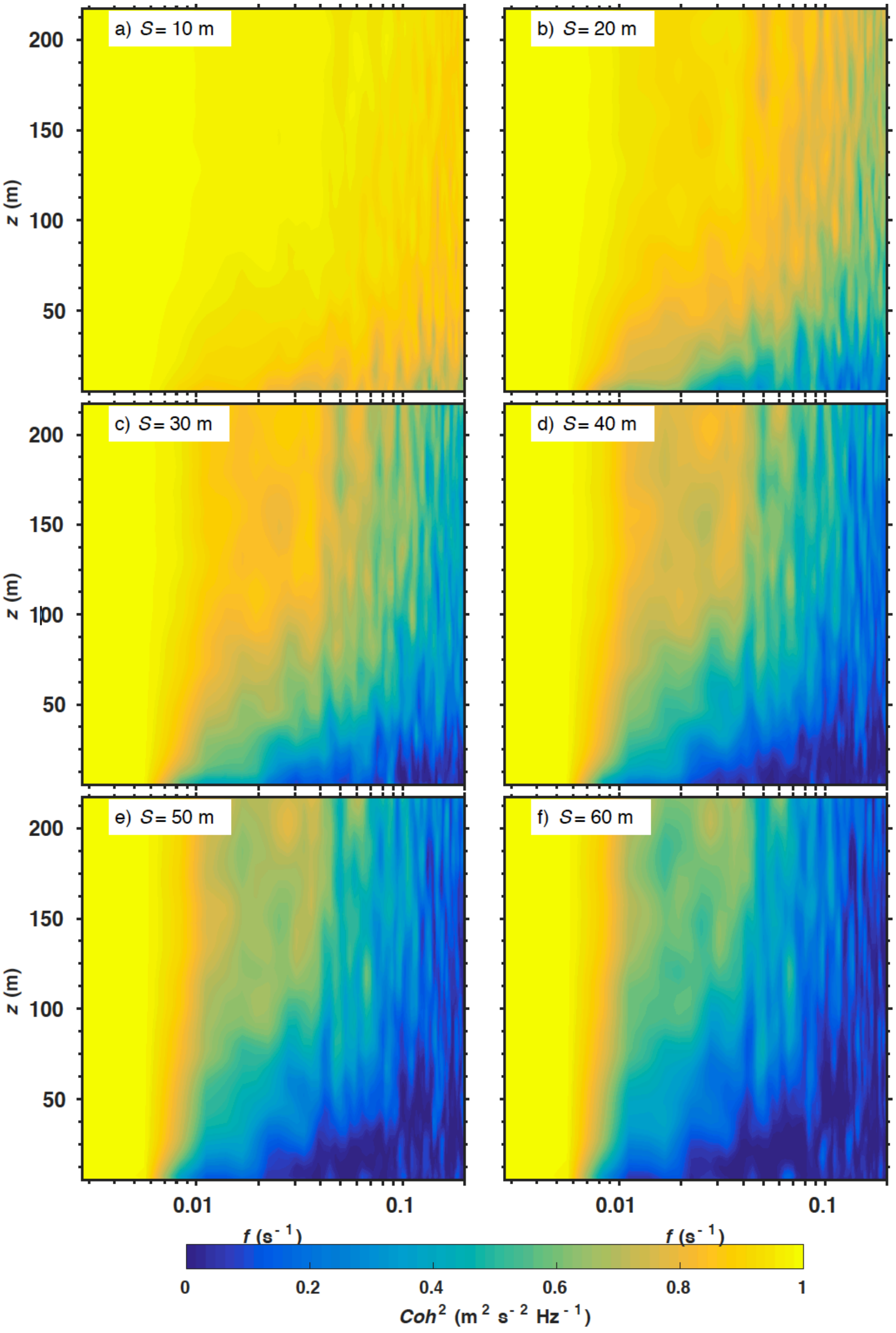

Figure 2.10 Contours of spatial coherence of the streamwise velocity component at six different horizontal separations, a) 10 m, b) 20 m, c) 30 m, d) 40 m, e) 50 m, and f) 60 m across the theoretical turbine. Data from the S10 simulation are from a radius of 70 km from the center of the hurricane. The wind speeds at this radius represent a Category-2 case.

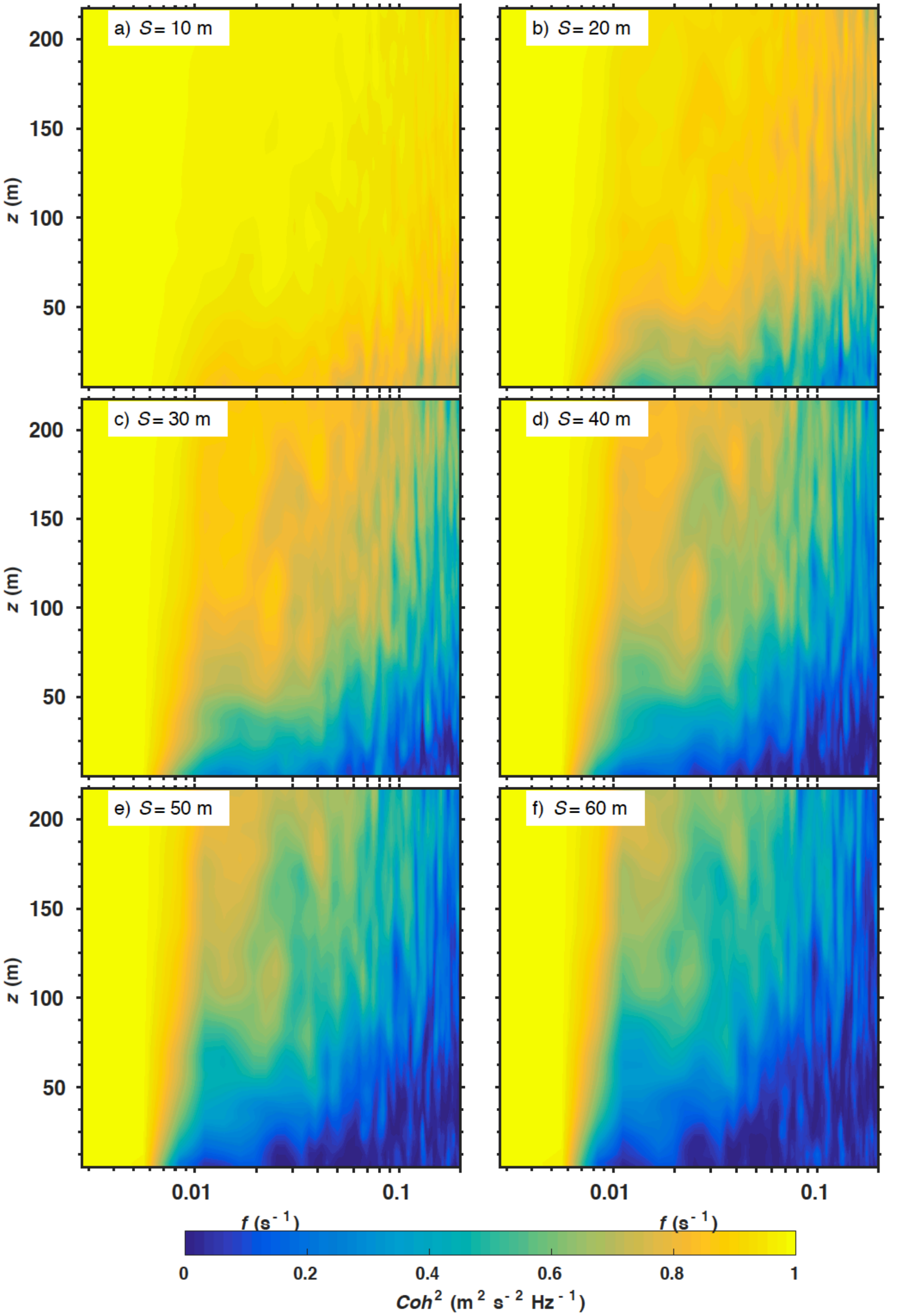

Figure 2.11 Contours of spatial coherence of the streamwise velocity component at six different horizontal separations, a) 10 m, b) 20 m, c) 30 m, d) 40 m, e) 50 m, and f) 60 m across the theoretical turbine. The data from the S10 simulation are from a radius of 35 km from the center of the hurricane. The wind speeds at this radius represent a Category-4 case.

Streamwise coherence in the HBL differs when calculated with horizontal and vertical separations (Figure 2.12). We calculate coherence between two horizontally-separated locations at 100 m ASL (Figure 2.12 a, b, c) and also between two vertically-separated locations (Figure 2.12 d, e, f). For the calculation using vertical separations, one location is at hub height (100 m ASL) while the other location is higher than the first location (i.e., at 110-190 m ASL).

First, at a radius of 130 km (TS case), the flow remains highly coherent (≥ 0.6) for greater horizontal separations than it does for vertical separations (Figure 2.12a, d). To illustrate this behavior, coherence as a function of separation is plotted at four frequencies representative of the flow. Turbulence in the HBL remains highly coherent for horizontal distances as great as 45 m for frequencies of 0.01 Hz (Figure 2.12a). For the same frequency, turbulence remains highly coherent for vertical distances of only15 m (Figure 2.12d).

Calculations of horizontal coherence show that large-scale turbulent structures in the HBL are very coherent for approximately 30 m of additional separation than that calculated for vertical coherence. This result occurs for all cases shown in Figure 2.12. We suspect that the larger coherence in the horizontal direction is related to the boundary-layer roll structure of the HBL (e.g., Wurman and Winslow 1998; Nolan 2005; Morrison et al. 2005; Zhang et al. 2008; Nakanishi and Niino 2012), which is reproduced in the *Simple* set-up (Bryan et al. 2017).

The coherence estimates from the *Simple* set-up differ greatly from the empirical coherence model recommended in IEC 61400-1 (IEC 2007a). The IEC exponential model (dashed lines in Figure 2.12) generally predicts coherence values smaller than that of the S10 simulations for horizontal separations, except at the lowest frequency, $f = 0.01$ Hz. The coherence predicted by the empirical model decreases too quickly, especially for short separations. However, as noted earlier, these differences may be related to the 10-m grid spacing of these hurricane simulations. Conversely, the coherence between two points separated by some vertical distance is slightly overestimated by the IEC coherence model.

The undulations in coherence seen in Figure 2.12d, e, and f suggest that, at a certain vertical separation, the structures in the HBL flow become similar again; the coherence does not simply decrease exponentially as vertical separation increases. Of course, these undulations occur for coherence values < 0.6, so the flow is not highly coherent over these large separations, anyway.

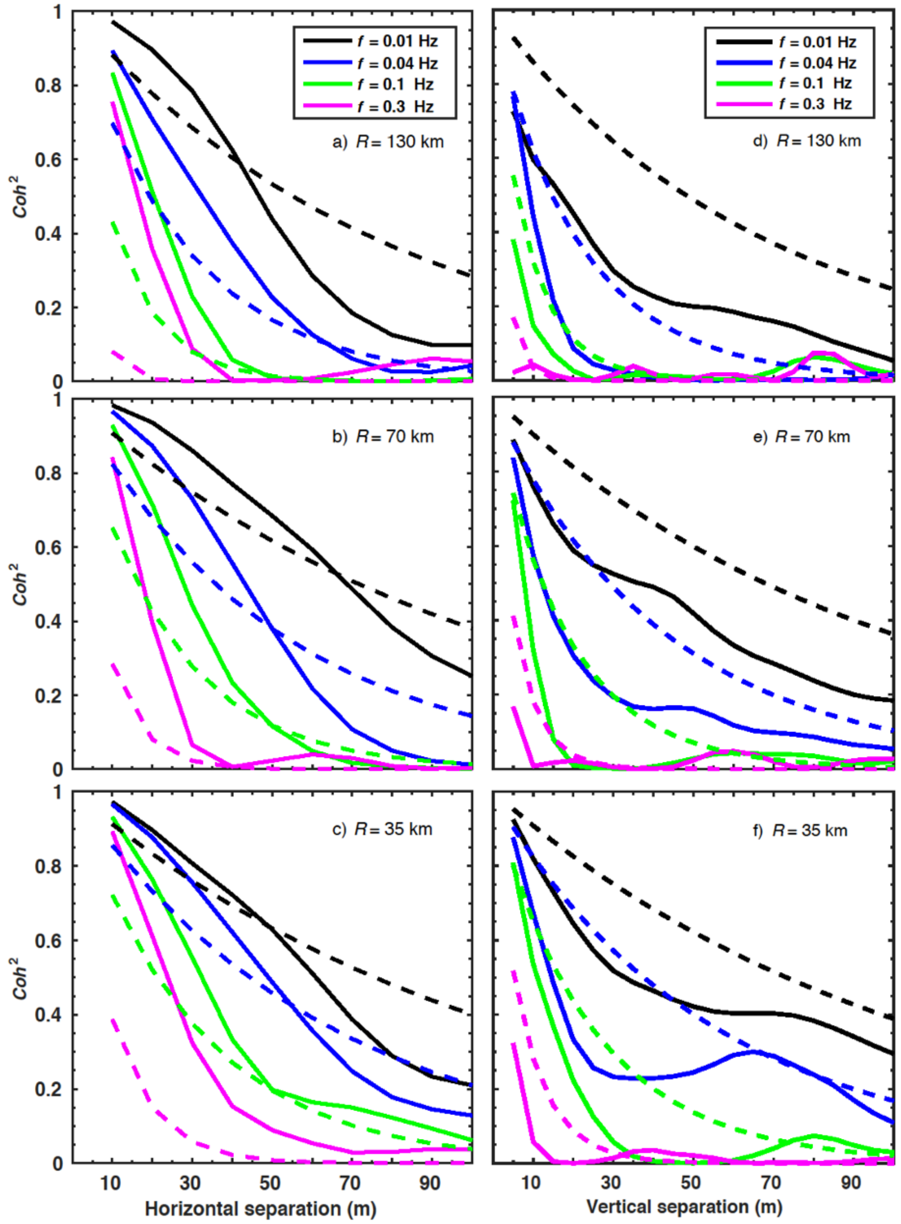

Figure 2.12 Spectral coherence of the streamwise velocity component as a function of horizontal (left) and vertical (right) separation across the theoretical turbine rotor-swept area. Coherence from the S10 simulations (solid lines) and the corresponding IEC exponential coherence model (dashed lines) are displayed. The four frequencies shown are representative of some of the eddies found within the HBL.

Finally, we present comparisons of coherence curves best-fit for various horizontal separations in the S10 simulations to those determined by the IEC coherence model (Figure 2.13). We estimate the coefficients of Eq. 2.4 that best represent the coherence of the flow in the HBL. Coefficients $a$ and $b$ are estimated for each storm case and for six different horizontal separations ranging from 10 m to 60 m (Table 2.4). The best-fit value for coefficient $a$ varies by an average absolute difference of 12.3% as the wind speed increases from tropical storm to Category-2 intensity and 6.8% as the wind speed increases from Category-2 to Category-4 intensity. A more noticeable difference in coefficient $a$ is how it varies as a function of separation. As the horizontal separation increases, coefficient $a$ increases by approximately a factor of 2 for each additional 10 m of separation. This sharp increase in coefficient $a$ as a function of separation is what leads to the rapid decrease in coherence as separation increases for each storm case (Figure 2.13). In the HBL, the LES-based estimates of coefficient $b$ are typically smaller than that used for the IEC standard (0.12). The second term under the square root in Eq. 2.4 becomes insignificant when coefficient $b$ is approximately zero, which occurs frequently in the HBL as seen in Table 2.4

In general, the exponential model used in the IEC standard underestimates the coherence between two points separated by some horizontal distance in the HBL (Figure 2.13). We suggest that separate coherence curves be used for the separation that is most relevant for a given aspect of turbine design. For instance, if an estimation of coherence between the hub and blade tip is essential, then we recommend using the coefficients in the column '$S = 60$ m' to achieve the best estimate. It is possible that one coherence curve could be used to represent these three storm intensities for a certain separation, but the significance of the differences among coefficients in each storm intensity should be tested in load simulations.

.

Table 2.4 Coefficients *a* and *b* for the IEC exponential coherence model (Eq. 2.4) (column 2) and estimates of coefficients *a* and *b* that best fit the coherence in the HBL for wind speeds associated with storms of tropical storm, Category-2, and Category-4 intensities (columns 3-8). Coefficients for six different horizontal separations, *S*, are presented.

| | | IEC | *S* = 10 m | *S* = 20 m | *S* = 30 m | *S* = 40 m | *S* = 50 m | *S* = 60 m |
|---|---|---|---|---|---|---|---|---|
| TS | *a* | 12 | 2.2269 | 4.3179 | 6.4679 | 8.5543 | 10.9075 | 13.7283 |
| | *b* | 0.12 | 0.1808 | 0.1386 | 0.0015 | 0.0001 | 0 | -0.0146 |
| Cat 2 | *a* | 12 | 2.6972 | 5.1046 | 7.1424 | 8.7773 | 10.1455 | 11.6413 |
| | *b* | 0.12 | 0 | 0 | 0 | 0 | 0 | 0 |
| Cat 4 | *a* | 12 | 2.5334 | 4.7865 | 6.7304 | 8.6356 | 10.8248 | 13.3475 |
| | *b* | 0.12 | 0.1071 | 0.1001 | 0.0883 | 0.0651 | 0.0349 | 0 |

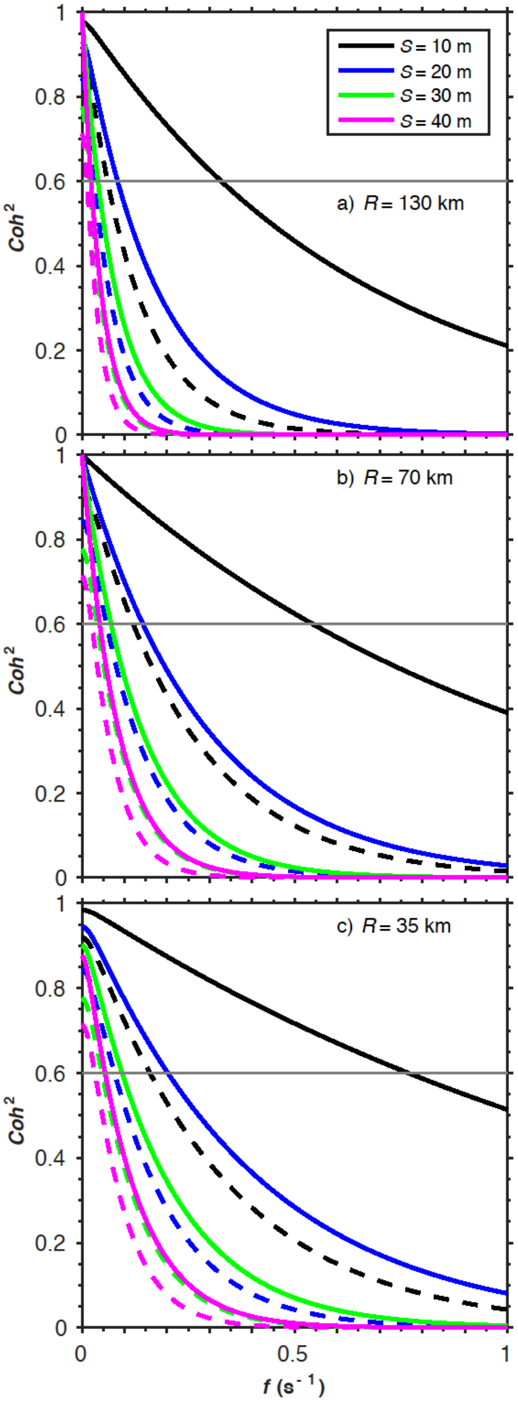

Figure 2.13 Coherence calculated for four different horizontal separations, 10 m (black), 20 m (blue), 30 m (green), and 40 m (magenta). The solid lines represent the best-fits from the non-linear regression to the S10 simulations and the dashed lines represent the coherence predicted by the IEC exponential coherence model (Eq. 2.4). Three radii/hurricane intensities are displayed, a) tropical storm, b) Category-2 hurricane, and c) Category-4 hurricane. The grey horizontal line shows the threshold above which the coherence is considered high (≥ 0.6).

## 2.5 DISCUSSION AND CONCLUSIONS

In the future, for wind turbines to survive Category-3, -4 and/or -5 hurricanes, designers should quantify the hurricane environment that such wind turbines would experience. Turbine survival during such major hurricanes introduces the possibility for lower-risk offshore wind-energy development off the US East Coast, including the south-east US. To assist in the understanding and design of these sturdy turbines, our study examined turbulence characteristics in the hurricane boundary layer using large-eddy simulation (LES).

In our study, an idealized Category-5 hurricane was simulated using two LES configurations (set-ups) of the CM1 model. The *Complex* and *Simple* set-ups produced similar normalized mean wind speeds, variances of the mean wind speed, and power spectral densities at altitudes of 50 m, 100 m, and 200 m ASL. The results from the two configurations also compared well at multiple hurricane radii. Since the *Simple* set-up provides results comparable to the *Complex* set-up but is computationally less expensive, the *Simple* set-up was then used at a much higher resolution (with $\Delta x$ =10 m and $\Delta t$ = 0.1 s) to analyze power spectral density and coherence. Validation of the *Simple* set-up was achieved via comparisons of virtual flights through the *Simple* set-up domain with actual flight-level observations collected from Hurricane Isabel (2003) during the CBLAST experiment. The comparison showed that the *Simple* set-up can be used to estimate realistic spectra within a hurricane where, unfortunately, suitable observations of adequate spatial and temporal resolution are extremely limited.

High frequency data (available at every timestep) from simulations using the *Simple* set-up provided virtual mock towers over a 21 × 21 grid (spanning 200 m × 200 m) to quantify the power-spectral-density and coherence characteristics that a theoretical turbine based on the NREL 5-MW reference turbine (Jonkman et al. 2009) would experience in the HBL. These simulations were run at three different radii of the overall Category-5 hurricane: 130 km, 70 km, and 35 km, that represent three different mean wind speeds: tropical storm, Category-2, and Category-4 hurricanes, respectively.

The power-spectral-density analyses revealed that the power spectrum of the wind speed in the HBL is dependent on hurricane wind speed (or, essentially, to radius within a given hurricane, excluding the eye). The peak of the power spectral density increased in magnitude as the hurricane intensity increased (or, equivalently, as the radius decreased in a given hurricane). Additionally, as the hurricane intensity increased, eddies with frequencies as high as $10^{-1}$ Hz significantly contributed to the turbulent energy in the flow. The vertical extent of the peak power spectral density in the HBL also increased with increasing hurricane intensity. In the Category-4 case, the greatest power in the flow extended upwards of 150 m. Recall that the NREL 5-MW turbine-rotor layer extends from 15 m to 165 m, implying that turbines located in intense hurricanes may experience extreme loads across the entire structure.

We compared the power-spectral-density curve derived from the *Simple* set-up to the standard Kaimal and von Kármán spectral models, which represent a homogeneous neutral PBL and are commonly used in a class of turbulent-inflow simulators for turbine design and load estimation. The empirical and theoretical spectral models underestimated the magnitude of the power spectral density in the HBL for all hurricane intensities. Further, the peaks in the simulated power spectral densities were shifted to higher frequencies than the peaks of the standard spectral models. This shift suggests that in the HBL, the most dominant eddies in the flow have a smaller wavelength (higher frequency) than in non-hurricane conditions. Modifications of the Kaimal model were proposed to account for the greater variance and the shifted peak in turbulent energy to higher frequencies in hurricanes. Because the difference between the modified Kaimal model coefficients derived using all three storm intensities was small, particularly between the Category-2 and -4 storms, we suggest one spectral curve for all cases.

Lastly, we analyzed coherence in the HBL. In general, the HBL flow remained highly coherent (≥ 0.6 coherence) for relatively large separations. Coherent flow between points separated horizontally by ≈ 60 m was apparent in the Category-4 case. This length is nearly the entire blade length of the NREL 5-MW turbine (≈ 63 m). As the hurricane intensity decreased, the coherence for these separations also decreased. However, even in the tropical storm case, the flow was highly coherent for separations as large as 40 m. The prevalence of rolls in the HBL (e.g., Wurman and Winslow 1998; Morrison et al. 2005) may explain these relatively large values of coherence. We suggest that turbine designers consider the potential additional mechanical loads induced by the prevalent and highly coherent structures with lengths corresponding to a typical turbine blade.

As with the power-spectral-density curve, we also compared the coherence curves produced from wind speeds in the hurricane cases to that generated by the IEC standard exponential model. The IEC exponential model generally underestimated the coherence for a given horizontal separation but overestimated the coherence for a given vertical separation. For these reasons, adjustments to the coefficients used in the IEC exponential model may be required.

We recognize that engineering design standards utilize simplifications that address a “worst case” loading scenario on a turbine. Our study highlights the fact that conditions in a major hurricane are likely not fully captured in the existing design standard. The results herein could be included in future design standards such as the upcoming subclass

T (i.e., tropical cyclone-specific design) to be released in the fourth edition of IEC 61400-1. Additionally, our results lay the groundwork for future investigations of the impacts of hurricanes on turbine loads. Based on the power-spectral-density and coherence analyses presented here, it is likely that the loads induced inside the HBL on offshore turbines vary from those induced in non-hurricane conditions. For this reason, it is important that loads on turbines located in the HBL be assessed. The three-dimensional wind velocities produced from these large-eddy simulations can be directly included in load simulators (as in Sim et al. 2010 and Park et al. 2014) or the modified spectral and coherence curves suggested can be used to simulate the full-field of inflow in wind simulators before utilizing load simulators. Additional simulations of varying hurricane intensities may provide further insight into hurricane turbulence effects on turbines. Wind-wave interactions in coupled models may influence these results (Suzuki et al. 2014; Hara and Sullivan 2015a), so LES models with both of these components could be used to analyze the effects of waves and the atmosphere on offshore turbines located in the HBL.

## 2.6 ACKNOWLEDGEMENTS

This material is based upon work supported by the National Science Foundation under Grant No. DGE-1144083. We thank Branko Kosović for helping define the initial directions of this research and contributing to the spectral calculations. Additionally, we are greatly appreciative of Evan Kalina and Paul Veers for sharing their expertise of hurricanes and turbine loads, respectively. We also acknowledge high-performance computing support from Yellowstone (ark:/85065/d7wd3xhc) provided by NCAR’s Computational and Information Systems Laboratory, sponsored by the National Science Foundation. We also thank the three anonymous reviewers who provided valuable feedback.

# 3 GUSTS AND SHEAR WITHIN HURRICANE EYEWALLS CAN EXCEED OFFSHORE WIND-TURBINE STANDARDS

## Preface

Current design standards for wind turbines typically suggest values for 10-min mean wind speed and 3-s gusts depending on the wind environment that a turbine will endure. Currently, there are no designated values for hurricane conditions in the International Electrotechnical Commission (IEC) design standard for wind turbines; it is the responsibility of the manufacturer to decide these values.

The work presented in this chapter builds upon the work discussed in Chapter 2 and provides estimates of the maximum 10-min mean wind speed, 3-s gusts, and gust factor found at mock-tower locations within a LES of a Category 5 hurricane using CM1. Hurricanes of this strength are considered to be a "worst-case" scenario for offshore wind turbines. We also evaluate metrics not currently used within the IEC design standard; results suggest that these metrics could be consequential to the durability of turbines. These metrics are veer across the rotor layer and wind direction shear at hub height during various averaging periods.

Collaboration with wind-turbine engineers for this project ensured that the metrics we analyzed are of practical use for the engineers that design and test wind turbines. The goal of the work presented in this chapter is to provide estimates of wind variables within the hurricane boundary layer that would influence wind turbines so that sturdier wind turbines can be built or so that risk is mitigated through financial tools such as insurance.

This work has sparked great interest within the offshore-wind-energy community, because hurricanes are a largely unknown component in regards to the viability of offshore development in hurricane-prone regions, including the US. It is our hope that the results within this and the previous chapter can help quantify the viability of offshore wind and the risks associated with it. The published manuscript has been featured in an *EOS* Research Spotlight available online at https://eos.org/research-spotlights/offshore-wind-turbines-cant-yet-withstand-category-5-hurricanes and in PBS NewsHour available online at http://www.pbs.org/newshour/rundown/offshore-wind-turbines-cant-handle-toughest-hurricanes/.

This chapter is adapted and reformatted from:

Worsnop, R. P., J. K. Lundquist, G. H. Bryan, R. Damiani, and W. Musial, 2017: Gusts and shear within hurricane eyewalls can exceed offshore wind-turbine design standards. *Geophys. Res. Lett.,* **44**, 6413−6420, doi: 10.1002/2017GL073537.

## 3.0 ABSTRACT

Offshore wind-energy development is underway in the U.S.A., with proposed sites located in hurricane-prone regions. Turbine-design criteria outlined by the International Electrotechnical Commission do not encompass the extreme wind speeds and directional shifts of hurricanes stronger than Category 2. We examine a hurricane's turbulent eyewall using large-eddy simulations with Cloud Model 1 (CM1). Gusts and mean wind speeds near the eyewall of a Category 5 hurricane exceed the current Class I turbine design threshold of 50 m $s^{-1}$ mean wind and 70 m $s^{-1}$ gusts. Largest gust factors occur at the eye-eyewall interface. Further, shifts in wind direction suggest turbines must rotate or yaw faster than

current practice. Although current design standards omit mention of wind direction change across the rotor layer, large values (15–50 deg) suggest that veer should be considered.

## 3.1 INTRODUCTION

Offshore wind energy generation in the U.S.A began with a 20-m tall, 20-kW turbine deployed ≈ 4 km off Maine's coast (Russo 2014). The first utility-scale wind farm, off the coast of Block Island, Rhode Island, can generate 30 MW (Justin Gillis 2016). Offshore wind farm sites are proposed in regions with hurricane return periods less than the 20-year expected lifetime of a wind farm (Keim et al. 2007; Russo 2014). According to the National Hurricane Center (NHC), a return period of a major hurricane (1-min sustained winds ≥ 49 m $s^{-1}$ at 10-m elevation) is as short as 16 years along the North Carolina coast (NHC 2016). Three-second gusts exceeding this wind speed threshold can occur even more frequently (Neumann 1991). Hurricane winds pose a substantial risk to turbines deployed in hurricane-prone regions, as demonstrated by the destruction of turbines during Typhoons Maemi (2003) and Usagi (2013) (Chen and Xu 2016). Therefore, hurricane-tolerant turbine designs are now being considered to address this risk (DOE 2015).

Current design standards for offshore wind turbines do not provide design parameters accounting for extreme winds associated with tropical cyclones. The International Electrotechnical Commision (IEC) offers a special class of wind turbines, Class S, for conditions outside of Class I-III specifications, as in hurricanes (IEC 2007a). However, the values of extreme wind speeds and directions must be specified by the turbine manufacturer, because design parameters specifically for hurricanes have not yet been issued by IEC. Further, the standard is silent on the issue of veer for all turbine classes. To provide design guidance, we compare our results to values provided by the IEC for the strongest class of turbines outside of tropical conditions (Class I). We demonstrate that mean wind speed, 3-s gusts, gust factor, and wind direction shifts can exceed current Class I design criteria, suggesting that modifications are required. Because the current classes of turbines in the IEC standard are not intended for tropical storm environments (IEC 2007a), a well-defined special design class may be needed for turbines in hurricane-prone regions.

The lack of adequate turbulence measurements at turbine heights undermines the understanding of how wind conditions in the hurricane boundary layer (HBL) affect wind turbines in the path of major hurricanes. Profiles of mean horizontal wind speed within the HBL are approximately logarithmic from ≈ 20 m to 300 m above sea level (ASL) (Powell et al. 2003; Vickery et al. 2009), consistent with the IEC's standard logarithmic profile. Vickery and Skerlj (2005) found the IEC's gust factor can represent hurricane gust factors at 10-m elevation, for wind speeds ≤ 60 m $s^{-1}$. They did not examine hub-height gust factors, which are needed to determine the loads turbines experience. Worsnop et al. (2017a) assessed turbulence spectra and spatial coherence for a theoretical wind turbine within a simulated HBL. Their results showed greater horizontal coherence along with a shift in peak spectra to higher frequencies than those in the IEC standard, suggesting that unique wind characteristics within the HBL may exceed current design standards and may intensify aerodynamic loading effects.

To study the most extreme wind conditions, data are required from the strongest winds in the eyewall, the turbulent region surrounding the eye of the hurricane (Powell and Cocke 2012). The radius of maximum winds (RMW), within the eyewall, is typically ≈ 20 km for a Category 5 hurricane (Kimball and Mulekar 2004; Stern et al. 2015). Offshore hurricane wind data at turbine heights (below 200 m ASL) are extremely limited. Reconnaissance flights are normally flown at 1.5–3 km ASL (French et al. 2007; Cione et al.

2016), offshore towers are sparse (Archer et al. 2013) and usually incur damage from direct hurricane hits, and dropsonde data are spatially limited within the storm, and unlikely to sample the most extreme winds (Stern et al. 2016). However, large-eddy simulations (LES) can provide simulated winds within the eyewall at turbine heights with high spatial (≈ 30 m) and temporal (≈ 0.2 s) resolution. We can also examine the radial dependence of wind speed and direction to determine the most problematic regions within the hurricane. These data could provide further design guidance for upcoming hurricane-resilient turbine standards, which will appear in IEC 61400-1 Ed. 4.

Herein, we use LES to provide critical data to revise offshore wind-turbine design standards. In section 3.2, we discuss the model configuration and data-aggregation methods. In section 3.3, we quantify gusts and gust factors at a range of radii. We discuss shifts in wind direction at hub height in section 3.4 and veer across the rotor layer in section 3.5. Lastly, we summarize findings and offer suggestions to modify design standards in section 3.6.

## 3.2 LES OF A HURRICANE

We simulate an idealized Category-5 hurricane, a worst-case scenario for wind turbines: damage increases exponentially with wind speed (Landsea 1993). We use the 3D, non-hydrostatic, time-dependent numerical model Cloud Model 1 (CM1) (Bryan and Rotunno 2009; Bryan et al. 2017). This idealized simulation is based on a Category-5 hurricane, Felix (2007). The simulation's outer domain (3000 km x 3000 km x 25 km) encompasses the entire hurricane (eye, eyewall, and rainbands). Within this outer domain, a fine-mesh LES domain (80 km x 80 km x 3 km) with horizontal (vertical) grid spacing of 31.25 m (15.625 m) resolves the turbulent winds within the inner core, including the eye and eyewall. We output data every 0.1875-s time step at virtual towers located every kilometer in x and y (Figure 3.1) and at every model level from 7.81 m to 507.81 m ASL.

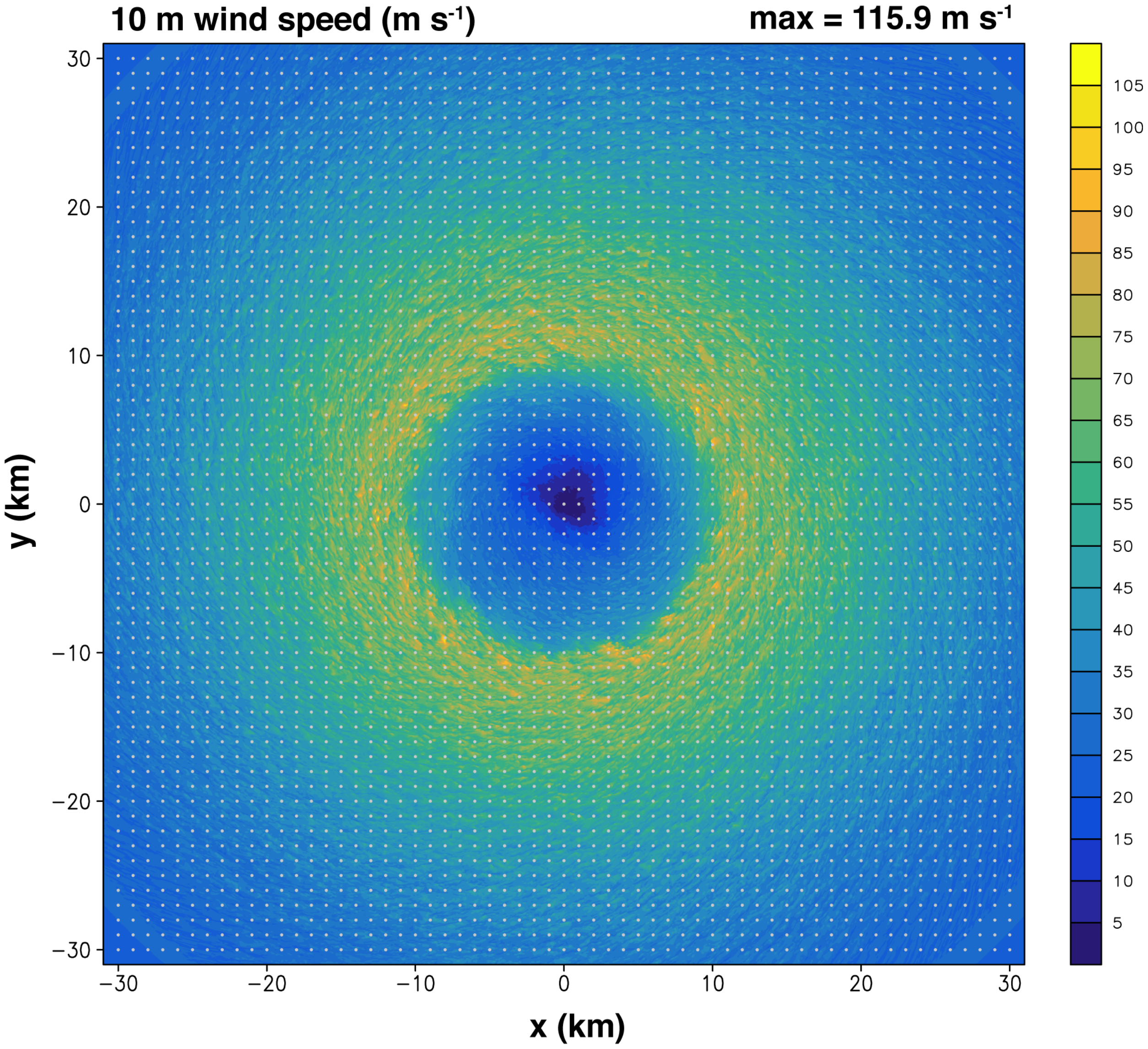

Figure 3.1 Instantaneous snapshot of the 10-m wind field produced by the CM1 model ($\Delta x = \Delta y = 31.25\ m$). Locations of the virtual towers and thus data output are shown as the gray dots.

This simulation is initialized from an axisymmetric model simulation of the hurricane, plus random perturbations, as in Richter et al. (2016) and Worsnop et al. (2017a). The simulation reaches steady-state after 4 h. We analyze wind fields from a subsequent 10-min period, the averaging period used in the IEC standard and recommended by the World Meteorological Organization (Harper et al. 2010). LES are computationally expensive; this simulation required more than 500,000 core hours (one week of wall-clock time using 4,096 cores). Worsnop et al. (2017a) present validation of CM1 compared to hurricane observations. This configuration is identical to the "Complex" simulation of Worsnop et al. (2017a); here, we double the temporal and spatial resolution.

We calculate 10-min mean wind speeds, 3-s gusts, gust factors, directional shifts at hub height (≈ 100 m), and veer at each virtual tower location shown in Figure 3.1. We then aggregate the towers into 1-km radial bins to obtain a representative sample at each radius. Finally, we take the maximum value of these variables at each radius to assess the strongest wind conditions a wind turbine would experience in a major hurricane.

## 3.3 HURRICANE GUSTS AND GUST FACTOR

HBL flow is not homogeneous: greatest wind speeds occur within the eyewall. The peak 3-s gust quantifies the highest 3-s average wind speed observed within a longer interval, here 10-min (Harper et al. 2010), and is used to estimate loads. Gusts exceeding 70 m $s^{-1}$ at altitudes across the rotor are problematic (IEC 2007a) and may cause significant damage; we find these gusts occur within and just outside of the eyewall of major hurricanes (Figure 3.2b–d). Some gusts exceed 100 m $s^{-1}$. These gusts could cause extreme aerodynamic and structural loading on turbines, leading to damage/failure of turbine components and possibly component fatigue if the gusts re-occur. For this storm, this critical region spans ≈ 10 km ($R$ = 10-20 km). These wind speeds agree with maximum observed speeds in an analysis of ≈ 12,000 dropsondes from tropical cyclones (Stern et al. 2016); extreme horizontal wind speeds (≥ 90 m $s^{-1}$) and updrafts (≥ 10 m $s^{-1}$) can occur within the eyewall at altitudes as low as 100 m. Outside the simulated eyewall region, gusts fall below 70 m s$^{-1}$.

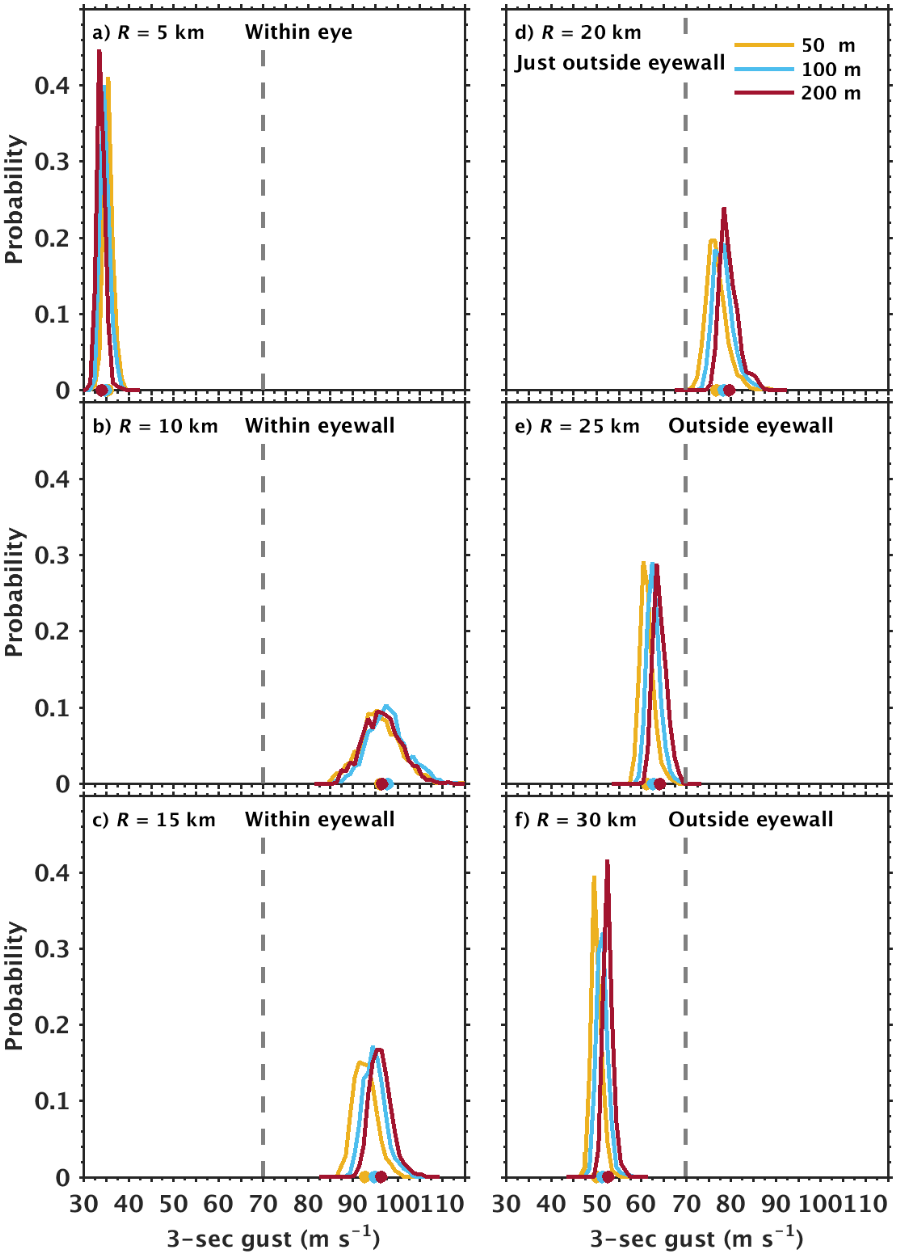

Figure 3.2 Histograms of the 3 s gusts at different locations within the hurricane: a) eye (in this case, R = 5 km), b) and c) eyewall (in this case, R = 10 and 15 km), d) just outside of the eyewall (in this case, R = 20 km, and e) and f) outside of the eyewall (in this case, R = 25 and R = 30 km). Probabilities are shown for gusts at 50 m (gold), 100 m (blue), and 200 m (brown) ASL. Means of the distributions are shown as the gold, blue, and brown dots. For reference, the 70 m s$^{-1}$ gust threshold is also shown (gray dashed).

By considering maximum 10-min mean wind speed and 3-s gusts at each radius (Figure 3.3a), we identify regions where the wind speeds exceed current Class I design thresholds (50 m $s^{-1}$ mean wind and 70 m $s^{-1}$ peak gusts) and therefore where Class I wind turbines may fail. Even these thresholds may be too lenient: turbines along Japan's coast were severely damaged in mean wind speeds below this threshold ($\approx$ 38 m $s^{-1}$): the peak gust reached 74 m $s^{-1}$ during Typhoon Maemi (2003) (Ishihara et al. 2005). Peak gusts (Figure 3.3, black lines) exceed 100 m $s^{-1}$ over a range of $\approx$ 8 km, suggesting that in a direct strike, turbines should anticipate gusts higher than the current threshold (or that destruction should be assumed). Such an occurrence may be rare. However, mean wind speeds can exceed design thresholds even outside the eyewall (radii up to $\approx$ 32 km) (Figure 3.3a). A thorough investigation of return periods and likelihoods of eyewall conditions is needed to justify the expense of design modifications.

Gust factor, $G_{t,T_0}$, estimates the expected peak gust based on the mean wind speed, $V_{T_0}$,

$$G_{t,T_0} = \frac{V_{\tau,T_0}}{V_{T_0}}, \tag{3.1}$$

where $V_{\tau,T_0}$ is the highest 3-s mean (gust) that occurs within 10 min ($\tau$ = 3 sec, $T_0$ = 600 sec) (Harper et al. 2010). Gust factors for turbines should be representative of hub-height winds. Vickery and Skerlj (2005) determined hurricane gust factors from onshore and offshore observations collected below 40 m and for wind speeds $\leq$ 60 m $s^{-1}$. Here, we examine gust factors at turbine heights to highlight regions with the highest gust factors (Figure 3.3b).

The highest gust factors ($\approx$ 1.7), outside of the quiescent eye occur at the eye-eyewall interface (here, $R$ = 9-11 km) inward of the peak gusts (we ignore gust factors within the eye because mean wind speeds there are too weak to impact wind turbines). Additionally, gust factors $\geq$ 1.4 occur below 30 m ASL, on average, just outside of the eye-eyewall interface ($R$ > 11 km). Generally, the gust factor is ≤ 1.4 (the standard IEC value corresponding to mean wind speed of 50 m $s^{-1}$ and gust of 70 m $s^{-1}$) outside of the eyewall (except below ≈ 30 m ASL). This result is consistent with Vickery and Skerlj (2005) who showed that, over the open water, gust factors ≤ 1.4 for wind speeds ≤ 60 m $s^{-1}$. However, we find that gust factors up to 1.7 occur in the eyewall, and values of 1.5 occur close to the surface even outside the eyewall. While a gust factor of 1.4 is adequate for most of the hurricane, it underestimates the eyewall region and regions outside of the eyewall below 30 m ASL.

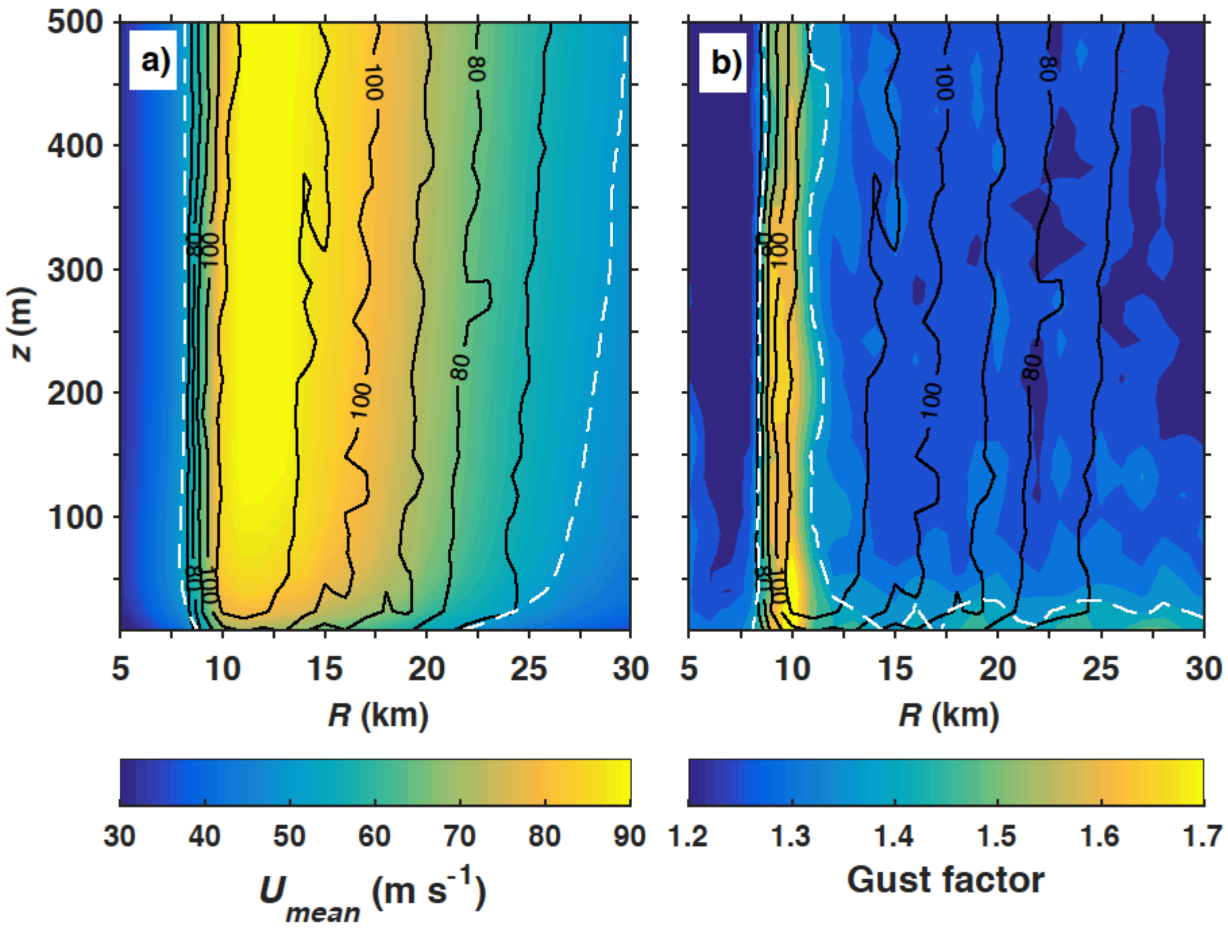

Figure 3.3 a) Radius-height contours of the maximum 10 min mean wind speed (colored contours) at each radius and height overlaid with maximum 3 s gusts (black contours, only values exceeding 70 m s$^{-1}$ are plotted); b) radius-height contours of the maximum gust factor (colored contours) during 10 minutes overlaid with maximum 3 s gusts (black contours, only values exceeding 70 m s$^{-1}$ are plotted). Contours (white-dashed) of the 50 m s$^{-1}$ 10-min mean wind threshold and a threshold gust factor of 1.4 are shown in a) and b), respectively.

## 3.4 YAW MISALIGNMENT

Wind direction can shift 180 deg during a hurricane passage over 0.5-1.5 h (Clausen et al. 2007). While turbines can slowly yaw, or rotate into the mean wind direction, abrupt changes in wind direction may affect turbine survival. Edgewise vibrations induced by yaw misalignment (Fadaeinedjad et al. 2009) damage turbine blades and induce buckling of the tower. Yaw misalignment, possibly from yaw drives breaking, the system's inability to keep up with the changing wind direction, or loss of grid connection caused turbines to fail at a wind farm in China during passage of Typhoon Dujuan (2003), even when wind speeds were below the design speed (Clausen et al. 2007).

Large shifts in wind direction occur at hub height (Figure 3.4). Largest shifts occur within the eyewall (here, ≈ 10 km) perhaps due to coherent vortices ("mesovortices") (Aberson et al. 2006). Turbines typically yaw based on the recorded 10-min average change in wind direction. However, for higher wind speeds, a shorter averaging time and faster yaw-response time are possible. The tails of the distributions (Figure 3.4) reveal that the wind direction can shift 10–30 deg over durations < 10 min even outside the eyewall. Yaw misalignment could occur frequently if the yaw system were not designed to sense and respond to 1-min or less directional shifts. Near the eyewall, abrupt changes in wind direction at hub height suggest a yaw response faster than 10 min may be needed.

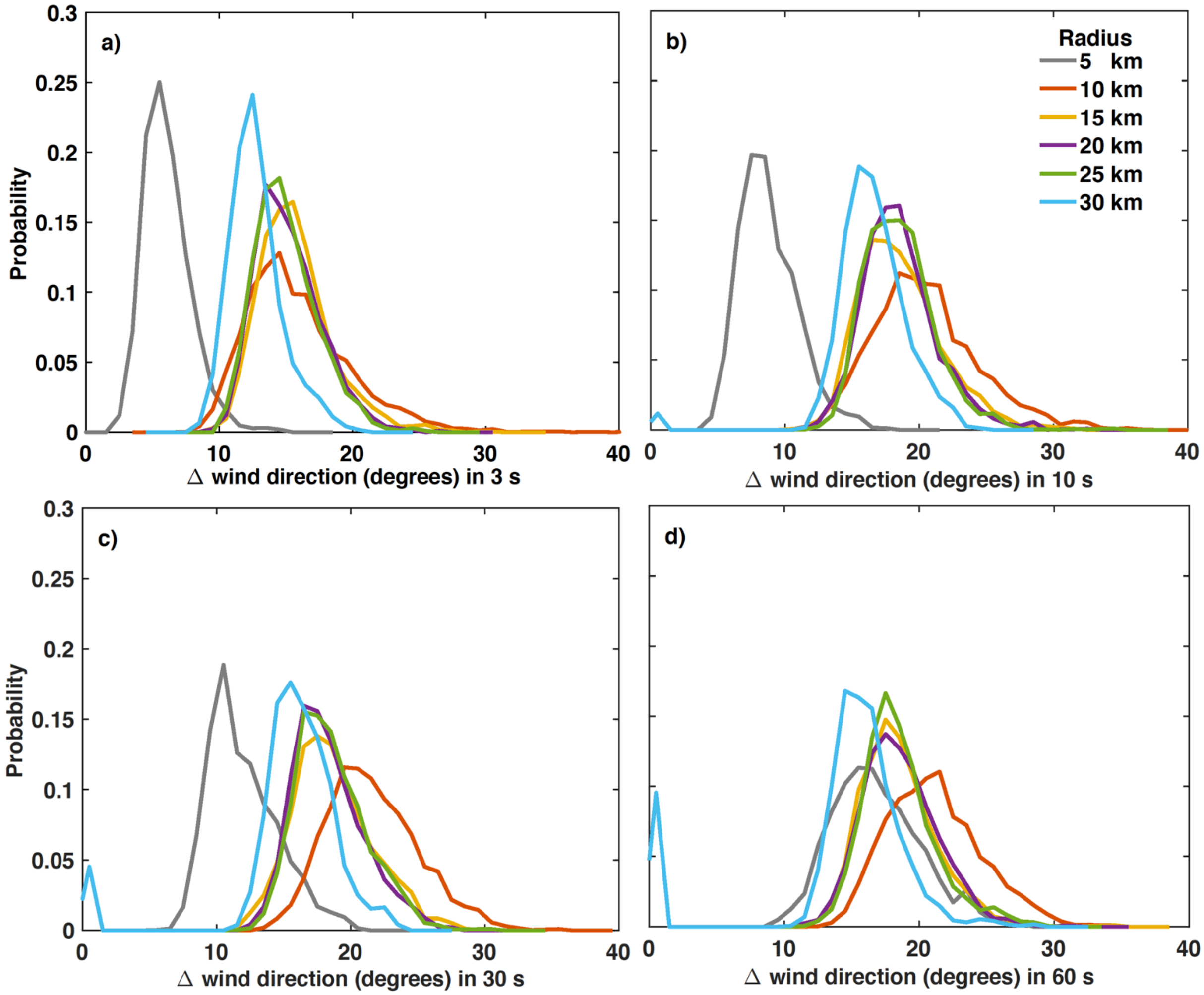

Figure 3.4 Histograms of the maximum change in wind direction over a) 3, b) 10, c) 30, and d) 60 s. Six hurricane radii are shown for each histogram: 5 km, 10 km, 15 km, 20km, 25km, and 30 km from the hurricane center.

## 3.5 WIND VEER

Current design standards do not address veer, the change in wind direction across the vertical rotor layer, even though veer may affect turbine loads and has been shown to affect power production (Walter et al. 2009; Vanderwende and Lundquist 2012). Varying wind direction can cause additional stress leading to mechanical failure. We calculate the average veer at each tower in each radius bin relative to hub height (100 m) over averaging periods from 3 s to 1 min (Figure 3.5) and then take the maximum value over all towers in that radius bin. Within 200 m ASL, we find the wind direction can change > 35 deg (maximum of 55 deg) as compared to hub height for periods ≤ 10 s (Figure 3.5a, b). Veer ranges from 5 to15 deg, particularly below 50 m for averaging periods of 30 s and 1 min (Figure 3.5c, d). This strong veer demonstrates that wind turbines will endure swift changes in wind direction, across the vertical rotor layer, on the order of 1 min or less during an eyewall passage. Testing the influence of an average veer of 15 deg in load simulators such as FAST (Jonkman and Buhl 2005) would reveal how veer impacts turbine loads and whether manufacturers should include veer in the turbine design process.

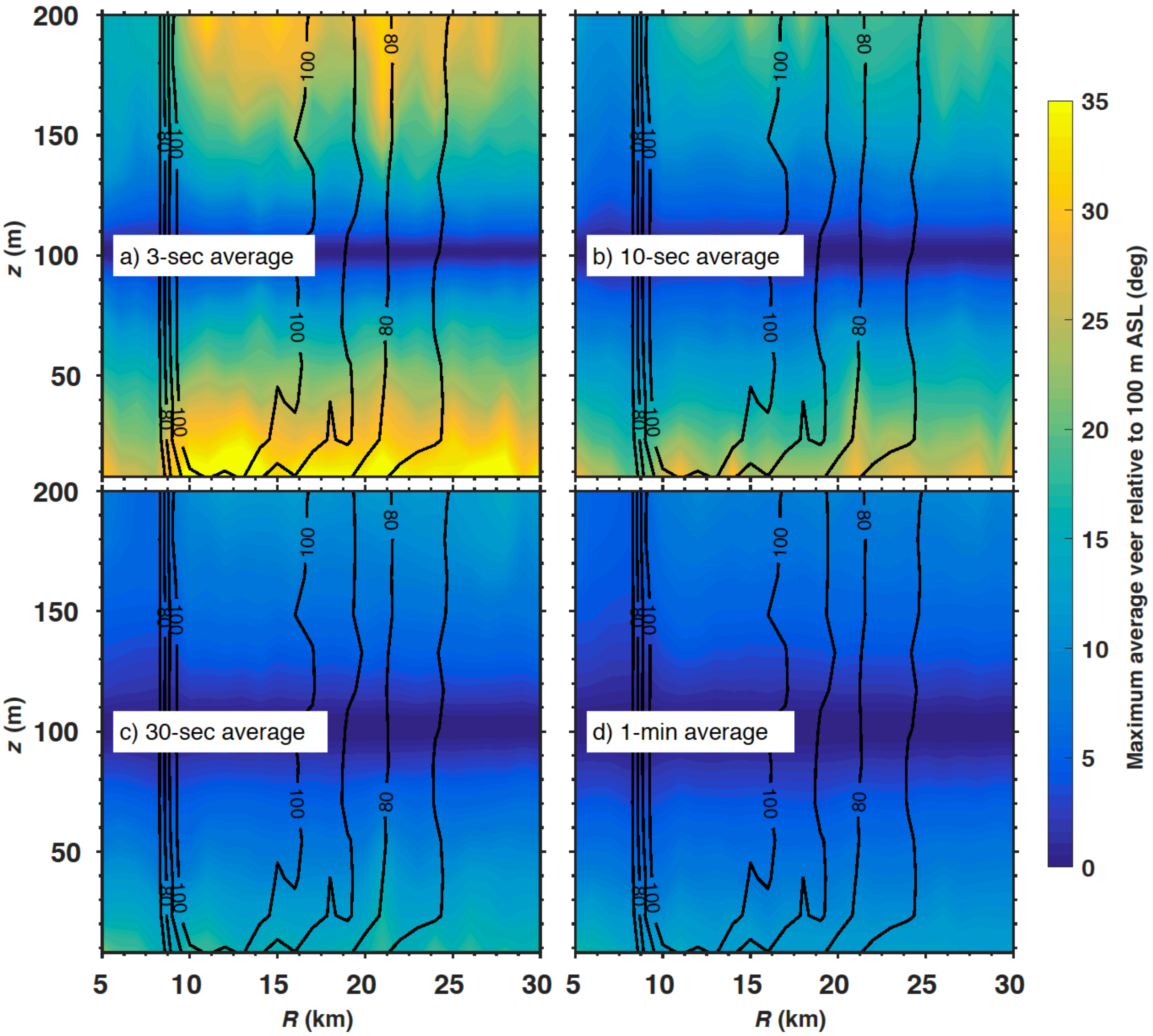

Figure 3.5 Radius-height contours of the maximum average veer relative to hub height (100 m ASL) (colored contours) for averages calculated over: a) 3 s, b) 10 s, c) 30 s, and d) 1 min. Overlaid are the maximum 3 s gusts (black contours, only values exceeding 70 m $s^{-1}$ are plotted).

## 3.6 CONCLUSION

We examined gusts, gust factor, and wind direction changes in the hurricane boundary layer (HBL) and compared these values to those in the IEC wind-turbine design standard for Class I turbines. We represented the HBL with large-eddy simulations of an idealized Category 5 hurricane using Cloud Model 1 (CM1). Results indicate that conditions outside the design standards would be encountered by wind turbines experiencing the eyewall and near-eyewall regions of a Category 5 hurricane; turbines built to current design standards would incur structural damage.

Mean wind speed and 3-s gusts are greatest in the turbulent eyewall of the hurricane. Within and just outside of the eyewall, winds exceed the current turbine design thresholds of 50 m $s^{-1}$ mean wind and 70 m $s^{-1}$ peak gust. Mean wind speeds (gusts) can exceed 90 m $s^{-1}$ (100 m $s^{-1}$) within the eyewall, consistent with observations (Stern et al. 2016), suggesting that either design standards or expected turbine lifetimes be modified to account for extreme conditions within a hurricane, if the probability of a direct eyewall strike is deemed likely in the wind farm location.

We also analyzed gust factors at altitudes relevant for wind turbines (< 200 m ASL). Largest gust factors occur at the eye-eyewall interface, just inward of the peak gusts. While the majority of the hurricane gust factors outside the eyewall are similar to those previously reported (Vickery and Skerlj 2005), gust factors exceed 1.7 within the eyewall. While the eyewall constitutes a small fraction of the total hurricane area, climatologies of Atlantic Category 5 hurricanes (Fig. 15 of Kimball and Mulekar (2004) and Fig. 10 of Stern et al. (2015)) show the median RMW is ≈ 20 km, which could engulf a wind farm experiencing a direct strike. Additionally, for radii outside the eyewall and RMW, the gust factor is greatest at altitudes < 50 m ASL. At these locations, the gust factor can exceed 1.4, the value used in the IEC standard to convert a reference wind speed of 50 m $s^{-1}$ to a 3-s gust. A value of 1.5 may be more accurate to estimate gusts at the lower reaches (≈ 30 m ASL) of wind turbines outside the eyewall of a Category-5 hurricane.

Wind direction shifts in the HBL lead to significant yaw misalignment: wind directions can shift 10–30 deg over durations < 10 min. Turbines should be able to respond to directional shifts on these shorter timescales to avoid damaging loads. In quantifying the absolute average veer for a typical turbine, we found shifts of 35 deg or greater from the hub to the tip of the rotor layer for 3- and 10-s periods. For 30-s and 1-min periods, veer is weaker, but can reach 15 deg. Veer across the turbine is not considered in current design standards, but these results suggest its influence should be tested in load simulators to determine if veer should be an essential component of turbine load estimations.

These results can guide the design of robust offshore wind turbines for hurricane-prone regions and the quantification of financial risk for those offshore wind turbines. The results herein could inform the upcoming subclass T (typhoon/hurricane resilient) turbines, which will soon appear in IEC 61400-1 Ed. 4. Investigation of the actual turbine loads induced by the gusts, veer, and yaw misalignments discussed herein can help determine the modifications required to build turbines to withstand major hurricanes. Incorporating these LES into turbine-load simulators as in  and accounting for storm surge (Jordan and Clayson 2008) and breaking waves (Suzuki et al. 2014; Hara and Sullivan 2015b) near offshore wind turbines would be a viable next step.

## 3.7 ACKNOWLEDGEMENTS AND DATA

This material is based upon work supported by the National Science Foundation under Grant No. DGE-1144083. We also acknowledge high-performance computing support from Yellowstone (ark:/85065/d7wd3xhc) provided by the National Center for Atmospheric Research’s Computational and Information Systems Laboratory and sponsored by the National Science Foundation. This work was partially supported by the U.S. Department of Energy under Contract No. DE-AC36-08GO28308 with the National Renewable Energy Laboratory. Partial funding was provided by the DOE Office of Energy Efficiency and Renewable Energy, Wind and Water Power Technologies Office. Model output from this study is stored on NCAR's High Performance Storage System and is available from the authors upon request. We also thank the anonymous reviewers for their helpful suggestions.

# 4 GENERATING WIND POWER SCENARIOS FOR PROBABILISTIC RAMP EVENT PREDICTION USING MULTIVARIATE STATISTICAL POST-PROCESSING

## Preface

Power ramps are large changes in power generated by wind turbines during a period of minutes to hours. These abrupt changes in power are caused by fluctuations in wind speed and the cut-in, cut-out, and rated power characteristics of the wind turbine's power curve. Improvements to wind speed forecasts and power ramp events increase the reliability of wind power and reduce stress on the electric grid.

The work presented in this chapter shows how statistical post-processing can be used to correct under- and over-forecasting biases of ramp events and to provide uncertainty information. We use 21 months of 80-m wind speed forecasts from the High-Resolution Rapid Refresh (HRRR) model, coupled with observations from two meteorological towers, to test four multivariate methods to generate wind speed scenarios. We then convert the wind speed scenarios into power scenarios before identifying ramp events of varying magnitudes.

The results herein show that statistical post-processing can improve power ramp forecasts over the raw HRRR forecasts regarding the relative frequency of ramp events. However, we found that improvements from statistical post-processing are limited to the initial skill of the raw forecasts, which for our complex-terrain sites, was quite poor. Nonetheless, some skill is gained as well as enhancements for decision-making from the added uncertainty information. Of the four multivariate methods tested to generate scenarios, the Standard Schaake Shuffle (StSS) method discussed herein provides the best combination of simplicity and skill for predicting ramp events.

I conducted the research for this project in collaboration with my coauthors during my year-long Pathways internship at the National Oceanic and Atmospheric Administration in Boulder, CO.

This chapter is adapted and reformatted from:

Worsnop, R. P., M. Scheuerer, T. M. Hamill, and J. K. Lundquist, 2018: Generating wind power scenarios for probabilistic ramp event prediction using multivariate statistical post-processing. *Wind Energy Science*, in preparation.

## 4.0 ABSTRACT

Wind power forecasting is gaining international significance as more regions promote policies to increase the use of renewable energy. Wind ramps, large variations in wind power production during a period of minutes to hours, challenge utilities and electrical balancing authorities. In this study, we compare different methods to generate probabilistic ramp forecasts from the High-Resolution Rapid Refresh (HRRR) numerical weather prediction model with up to twelve hours of lead time at two tall-tower locations in the United States. We validate model performance using 21 months of 80-m wind speed observations from towers in Boulder, Colorado and near the Columbia River Gorge in eastern Oregon.

We employ four statistical post-processing methods, three of which are not currently used in the literature for wind forecasting to correct biases in the model and to generate short-term wind speed scenarios which are then converted to power. This probabilistic enhancement of HRRR point forecasts provides valuable uncertainty information of ramp events and improves the skill of predicting ramp events over the raw forecasts. We compute

Brier skill scores for each method at predicting up- and down- ramps to determine which method provides the best prediction. These statistical methods can be implemented by wind farm operators to generate a range of possible wind speed and power scenarios to aid and optimize decisions before ramp events occur.

## 4.1 INTRODUCTION

Global wind energy installation reached 486 GW in 2016; the total installed generation capacity in the US alone reached > 82 GW by the end of 2016 and has experienced a rapid rise since then (GWEC 2017). Increased interest in alternatives to fossil-fuel-based energy to mitigate greenhouse gas emissions as outlined in the international Paris Agreement (UNFCCC 2015) has propelled the global wind-energy sector even further. Because of increased interest and deployment of wind energy in the US and worldwide, accurate wind speed and power forecasts are becoming increasingly important for successful power-grid operation; in particular, the prediction of specific wind situations such as power ramps is key to effective operation and control of wind farms (Kuik et al. 2016).

Wind ramp events are challenging to forecast because these abrupt and large increases or decreases in wind speed - and thus power - happen on time scales of minutes to hours making it difficult for wind farm operators and the power grid to respond. Up-ramps, or sharp increases in wind farm power can lead to an overload of electricity generation (Kamath 2010a). Sometimes the additional electricity is sold to nearby utility companies, but often wind farms must curtail, or stop power production (Ferreira et al. 2010). Conversely, down-ramps, or sharp decreases in power production over short time periods, also have serious implications for the power grid. If power generation from the wind farm does not meet expectations, then power must be generated by another source to “balance the load" and avoid brownouts and blackouts. Additionally, the wind farm owners may have to pay costly fees for not meeting their contractual expectations (Marquis et al. 2011).

Improving the accuracy of ramp forecasts can help avoid the situations described above. The overall effects of ramps on the grid can be reduced in several ways. The development of a geographically aggregated power grid which connects many wind farms and diverse renewable sources such as solar, hydro, and nuclear power (Budischak et al. 2013; Archer and Jacobson 2007) can help minimize the effects of sudden gusts and lulls of wind speed on the power grid. Additionally, optimized wind farm locations (St. Martin et al. 2015) could reduce fluctuation on the grid caused by individual wind farms. Directly improving ramp forecasts is also a viable option to reduce stress on the power grid and make wind energy even more reliable. In practice, a persistence forecast of wind speed and power generation over a 1-h or 30-min time interval is commonly used (Milligan et al. 2003). Persistence forecasts are generally reasonable on these time scales, because local weather conditions usually do not change drastically during these lengths of times except during certain weather events, such as fronts, convective outflow, etc. that often cause ramps. Persistence forecasts are poor at predicting ramps; a ramp identified in the previous 30 min to an hour can change magnitude or even sign (i.e., up- or down-ramp) in a short period and therefore lead to large forecast errors. In recent years, there has been a growing interest in information regarding the uncertainty of wind power forecasts to make situation-dependent decisions (Nielsen et al. 2006b). Typical single (i.e., point) forecasts cannot provide this necessary uncertainty information, but probabilistic forecasts can.

Considerable effort over the last decade has been made to improve short-term wind and power forecasts (Wilczak et al. 2014). To improve beyond the use of persistence of a point forecast, some of these methods include the use of predictive distributions broken into quantiles for each lead time to quantify uncertainty, but still neglect the interdependence structure among forecast lead times (Bremnes 2006), a characteristic needed for time-dependent events such as the evolution of ramps. Other methods construct the interdependence structure of forecast distributions among lead times, but achieve the original quantiles from non-parametric forecast distributions, which make no assumptions about the shape of the actual forecast distribution (Pinson et al. 2009; Pinson and Girard 2012). Another method includes the direct use of an ensemble of forecasts produced by perturbing the initial conditions of a numerical weather prediction (NWP) model, which does not require the generation of predictive distributions and their interdependence structures through statistical means. However, the ensembles themselves are not always reliable (Nielsen et al. 2006a; Bossavy et al. 2013). Others have used analogs of past forecasts based on weighted atmospheric predictors to quantify forecast uncertainty (Delle Monache et al. 2013; Junk et al. 2015). The forecasting methods above physically derive the power output from a single wind turbine or wind farm by inputting forecasted wind speed values into a turbine power curve provided by the wind turbine manufacturer. If the approach is purely statistical, a relationship between measured wind speed and power output from a training dataset is used to bypass the use of a power curve for future wind speeds (Lange and Focken 2006).

Here we correct biases in wind speed point forecasts produced by the HRRR NWP model using univariate post-processing techniques and parametric distributions. We employ four multivariate statistical post-processing methods to generate forecast scenarios of wind speed, representing the prediction uncertainty for a 12-h forecast horizon. We then compare the skills of the methods at predicting up- and down-ramp events. Three of the four methods, (the Schaake Shuffle, Minimum Divergence Schaake Shuffle (MDSS), and the enhanced version of MDSS (MDSS+)) are not currently discussed within the wind-forecasting literature and are offered as new forecasting tools for short-term ramp events. The fourth method, the Gaussian copula, has been assessed for short-term wind and power forecasting so we use this method as a benchmark of performance for the new methods. For all of our analyses, we physically compute wind power production via a turbine power curve, which relates the power that would be generated by a turbine to wind speed through the turbine rotor layer as well as turbine-specific characteristics.

The wind speed observations from tall meteorological towers and forecasts from the HRRR model used in this study are discussed in Sect. 4.2. Up- and down-ramp events are formally defined in Sect. 4.3.1. The transition from deterministic to probabilistic forecasts using parametric predictive distributions is described in Sect. 4.3.2. The multivariate methods for generating probabilistic forecast scenarios are discussed in Sect. 4.3.3. In Sect. 4.4, we evaluate the performance of each probabilistic forecast method and the raw HRRR forecasts focusing on the prediction of up- and down-ramp events. Specifically, we compare the relative frequency of up- and down-ramp events produced from each forecast. We also provide Brier skill scores to compare each multivariate method and to show the performance relative to climatology. In Sect. 4.5, we offer concluding remarks, uses for the probabilistic methods in the wind-energy sector, and advice for operational implementation.

## 4.2 DATA

### *4.2.1 WIND MEASUREMENTS FROM TALL METEOROLOGICAL TOWERS*

We use wind speed and direction measurements from two meteorological towers. The first tower is the 135-m M5 tower located south of Boulder, Colorado, located ≈ 5 km east of the Colorado Front Range at the US Department of Energy (DOE) National Wind Technology

Centre (NWTC) (Clifton et al. 2013). Wind speed and direction measurements from the M5 tower were collected at 80 m and 87 m above ground level (AGL), respectively, from a cup anemometer and wind vane. The instruments were mounted on tower booms aligned at 278°, which was derived as the prevailing wind direction at the NWTC from a 15-yr climatology (Clifton et al. 2013). We remove wind speed measurements that are associated with wind directions between $75° - 135°$ to ensure that the measurements are not contaminated as a result of the flow passing through and around the tower or waked by a nearby wind turbine before reaching the instrument sensors. We also remove data flagged by quality-control methods such as testing for constant values during a measurement interval (which indicates icing events during cold months), or checking for standard deviation values < 0.01% of the mean (which indicates instrument malfunction) among other measures described by (Clifton et al. 2013; St. Martin et al. 2016). We also only retain data from dates that have a continuous 12-h segment of data from the 00Z and 12Z forecast initialization times to encompass an entire day. The M5 tower data that we use are measured at a 20-Hz rate and averaged over ten minutes for the period from 31 August 2012 to 28 February 2017.

The second tower is an 80-m tall proprietary tower located near the Columbia River Gorge, which divides the southern boundary of Washington and the northern boundary of Oregon. Herein, we refer to this tower as the Pacific Northwest (PNW) tower. The wind speed and direction measurements are collected from a heated cup anemometer and wind vane at 79 m and 76 m AGL, respectively and averaged to 1 min. We perform quality-control measures on the data to remove suspect data using similar quality-control processes as for the M5 tower. We remove flat-line data (which could either indicate icing events, communication issues, or malfunctions of the instrument) by checking for time periods where the standard deviation values were ≈ 0 or constant during a running 10-min interval. We also remove unrealistic wind speed values, such as negative numbers, and remove data associated with waked flow from the PNW tower or nearby turbines. We filtered out dates that did not have a continuous 12-h segment of data starting from the 00Z and 12Z forecast initialization times. Data from the PNW tower were made available as part of the DOE-funded second Wind Forecast Improvement Project (WFIPII) that took place from fall 2015 to spring 2017 (A2E 2017). We use data from this tower for all available dates between 18 March 2015 – 06 March 2017.

### *4.2.2 WIND FORECASTS FROM HRRR SYSTEM*

Deterministic forecast data are obtained from the second experimental version of NOAA's real-time, High-Resolution Rapid Refresh assimilation and model forecast system (HRRRv2). The HRRRv2 domain covers North America with 3-km horizontal grid spacing. HRRRv2 is updated hourly and includes 15-min data assimilation between each hourly update. Detailed model physics for HRRRv2 is discussed by Benjamin et al. (2015). For this study, we analyse 80-m wind speed forecasts initialized at 00Z and 12Z and forecast lead times up to 12 h to encompass an entire day. The available dates for this version of the HRRR are from 01 January 2015 – 28 September 2016. For this reason, forecast verification is performed on this period of interest but observations measured on dates outside of this period will be used by the Schaake Shuffle post-processing techniques (Sects. 3.3.2 – 3.3.4). For comparison of the forecasts to the tower observations, the HRRR forecast values at each tower location are from the nearest model grid cell to the tower latitude and longitude. In addition, since the HRRRv2 forecasts are output hourly, we apply our analyses to the observations that occur at the top of the hour to match the forecast availability.

## 4.3 METHODS

### *4.3.1 RAMP DEFINITION*

Wind power ramps are large changes in power production over short time periods. Despite the significant influence of ramp events on the electric grid and a clear need for accurate forecasts of these events, there is not a commonly accepted method to define and identify them. Ramp definitions vary in the literature (Kamath 2010b, 2011; Pinson and Girard 2012; Bossavy et al. 2013; Bianco et al. 2016) regarding the threshold of power change and the duration over which that change occurs. Variations also exist regarding which data points in a given window of time should be used when calculating the change in power, and lastly whether to use power time series directly when defining ramps or instead use a filtered time series (Bossavy et al. 2013). Commonalities in the literature include the need to define ramp magnitude, duration, and sign (i.e., up- or down-ramp).

This lack of a standard definition is primarily because what is considered an important ramp event depends on the needs of the wind farm operator or grid-system manager at any given time or location. Here, we employ a combination of the *Minimum-maximum* method used by Pinson and Girard (2012) and that employed in the Ramp Tool & Metric created by Bianco et al. (2016) to generate separate ramp time series for up-ramps and down-ramps. Up-ramps and down-ramps are considered separately, because they have different impacts on the power grid and lead to different decisions. Up-ramps may result in a swap of conventional energy sources for cleaner wind power while a down-ramp may result in the opposite and can have more detrimental effects on the grid during periods of high electricity demand.

Before identifying power ramps, wind speed observations and forecasts must be converted to power. A conversion from wind speed to power in this study is achieved via the International Electrotechnical Commission (IEC) turbine power curve for Class 2 turbines (IEC 2007b). This power curve is for wind turbines with a cut-in wind speed > 3 m $s^{-1}$, rated power ≥ 16 m $s^{-1}$, and a cut-out wind speed > 25 m $s^{-1}$. Using the resulting power time series, we create binary time series of up- and down-ramp events into ones (ramp occurred) and zeros (no ramp occurred). We do this by first dividing the power time series into $N_{win}$ sliding time windows of length $h$ and then finding the largest positive and negative power differences that exists within each window, $\Delta p_{max}$ and $\Delta p_{min}$, respectively. If the largest positive power difference equals or exceeds the defined power change threshold $\xi$, then the up-ramp time series is given a value of 1 for that time window. Conversely, if the largest negative power difference is less than or equal to $-\xi$, then a 1 is assigned to the down-ramp time series for that time window. If the above respective criterion is not met, then a 0 is assigned for that time window. The window then slides one hour forward in time and the process is repeated until there are $N_{win}$ binary values for both the up-ramp and down-ramp time series. We allow up-ramps and down-ramps to happen within the same time window, so that there could be a value of 1 assigned for the same time window in both the up- and down-ramp time series. This allowance is reasonable, because for some longer window-lengths, up-ramps and down-ramps could both occur and are equally important to forecast. An example of the identification of up- and down-ramps according to this method appears in Figure 4.1. While more complex ramp definitions are available, the chosen criteria for up- and down-ramps reflect the common intuition about ramps including threshold $\xi$ and window length $h$ to customize the definition to specific needs. As determined later, this ramp definition can be employed in a probabilistic framework and will be used to compare the different approaches to scenario generation.

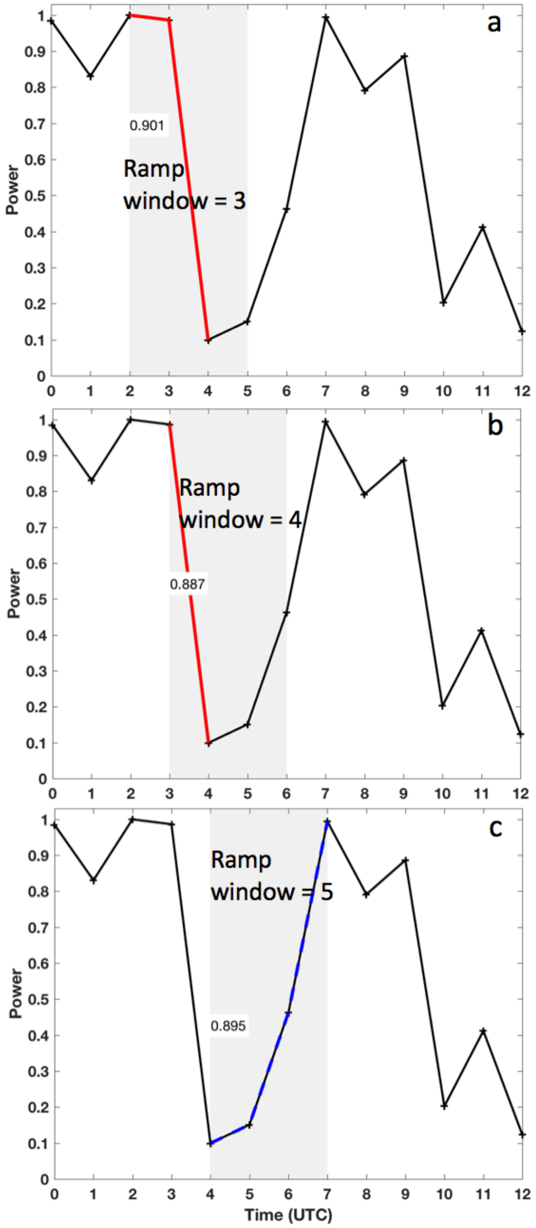

Figure 4.1 Ramp identification at the M5 tower location for an observed power time series at 00Z on 03 March 2016 for a window size $h$ = 3 h and change in power threshold $\boldsymbol{\xi} = \mathbf{60}\%$ of turbine power capacity. Three consecutive time windows are shown as the grey

rectangles in a, b, and c. The identified ramps in those time windows are highlighted in red (up-ramps with $\geq \mathbf{60}\%$ power change) and blue (down-ramps with $\leq -\mathbf{60}\%$ power change). The change in power capacity associated with each ramp is written in the white textboxes within the grey time windows. The total number of up- and down-ramps identified within all 3-h sliding time windows is 2 and 6, respectively.

### *4.3.2 DETERMINISTIC TO PROBABILISTIC FORECASTS: UNIVARIATE POST-PROCESSING*

To improve the skill of the raw HRRR forecasts at predicting ramp events, we employ statistical post-processing techniques to enhance the HRRR forecasts through the addition of uncertainty information. These methods convert the deterministic (single value) raw HRRR forecast into probabilistic forecasts by creating a set of forecast scenarios of wind speed that represent the forecast uncertainty. Wind speed scenarios are converted to power scenarios and then probabilities of ramp events are derived. The first step to generating scenarios is to perform univariate post-processing on the HRRR forecasts at each individual lead time.

We first determine a predictive distribution model for each tower and forecast initialization time which accurately predicts future observations for each forecast lead time. We employ ordinary-least-squares regression on the observed wind speed data in the period during which the HRRR forecasts are also available (01 January 2015 – 28 September 2016). The regression coefficients and future forecasts are then used to determine the mean and standard deviation of the predictive distribution model for each day and lead time of the forecasts. We find these statistical moments by inserting future forecasts into the fitted regression model. Before performing the regression, we apply a power transform (not to be confused with wind speed-to-power conversion) with power exponent $P$ to the forecasts $\tilde{x} = x^P$ and observations $\tilde{y} = y^P$ to address the increase of forecast uncertainty with wind speed (i.e., heteroscedasticity in the dataset). Heteroscedasticity in the data is visible as more spread in the data points at higher wind speeds than at lower wind speeds in Figure 4.2a. We select power exponents for the transformations that produce slope coefficients nearest to zero from a second regression of the absolute residuals from the first regression on the transformed forecasts. The exponent is 0.66 (0.75) for both initialization times and all lead times at the NREL M5 (PNW) tower.

After applying a power transform to the data, we remove the seasonal cycle for each location, initialization time, and lead time by normalizing the transformed forecasts and observations by the corresponding seasonal cycle. The seasonal cycle model takes on the form,

$$s(T) = a_0 + a_1 \sin(2\pi T) + a_2 \cos(2\pi T) \tag{4.1}$$

and the model coefficients $a_0$, $a_1$, and $a_2$ are determined by fitting the seasonal cycle model to the transformed forecasts for every forecast date in the form of fractional day of the year $T$. We fit the seasonal cycle model solely on the transformed forecasts, because there are more forecasts than observations available during the period of interest. Therefore, the same seasonal cycle coefficients are used to derive the seasonal cycle for the transformed forecasts and observations.

The transformation and removal of the seasonal cycle makes the relationship between the transformed forecasts and transformed observations more homoscedastic (i.e., more consistent forecast variability for all wind speeds in Figure 4.2b). This characteristic enables us to use more traditional statistical techniques and avoid the nonlinear regression that would be required between the untransformed forecasts and untransformed observations because of the heteroscedasticity. An inverse transformation of the observations, forecasts, and regression lines reveal the complexity of the regression line we would have had to use if we had not transformed the data before applying regression analysis (Figure 4.2c). The slight curvature in the regression and standard deviation lines in Figure 4.2c shows the dependence of error variance on wind speed magnitude (i.e., heteroscedasticity); the black dots are closer to the red regression line at lower wind speeds than at higher wind speeds. The scatter in the red regression dots in Figure 4.2c illustrates how the annual cycle influences the regression; depending on the time of year, the transformation value can be different because of the annual cycle.

We test three candidate predictive distribution models for the transformed wind speed observations using the predictive mean and standard deviation produced from the above linear regression: truncated normal, truncated logistic, and gamma distributions where the truncated distributions exclude negative values. These distributions, given the same mean and standard deviation, vary in the shape of their peaks and size of their tails. Probability integral transforms (PITs) of each predictive cumulative distribution function (CDF, $F_i$) and its verifying observation $y_i$ are calculated for each candidate distribution as $d_i := F_i(y_i)$, and provide an assessment of which distribution yields the best calibration (Dawid 1984; Gneiting et al. 2007). Histograms of the PITs which include all verification days and lead times show that the gamma and truncated logistic distributions are well-calibrated to the observed transformed wind speeds at the NREL M5 and PNW towers, respectively for 00Z (Figure 4.3) and 12Z (not shown) initialization times. This suitable calibration is qualitatively demonstrated by the mostly uniform histograms in Figure 4.3. For a more quantitative assessment of calibration, we compute the continuous ranked probability score (CRPS). The CRPS is a proper scoring rule that is often used to evaluate the quality of a probabilistic forecast by summarizing the sharpness and calibration of the forecast distribution (Gneiting et al. 2005; Gneiting and Raftery 2007). A proper score is one that produces the highest reward (i.e., lowest CRPS score) by using the true probability distribution (Gneiting and Raftery 2007). For a given pair of predictive CDF $F$ and verifying observation $y$, the CRPS is defined as

$$\mathrm{CRPS}(F,y) = \int_{-\infty}^{\infty}[F(\xi) - \boldsymbol{H}(\xi - y)]^2 d\xi, \tag{4.2}$$

where $F(\xi)$ is the probability that the forecast will not exceed threshold $\xi$ and $\boldsymbol{H}$ is a Heaviside step function which attains the value 1 when its argument is $\geq 0$, and 0 otherwise. A low CRPS value suggests a predictive distribution model can accurately represent future observations. We calculate the CRPS for each candidate predictive distribution using the closed-form expressions for the CRPS of a truncated normal (Gneiting et al. 2006) and the truncated logistic and gamma distributions (Scheuerer and Möller 2015). Based on the CRPSs, averaged over all lead times for each tower and initialization (Table 4.1), and the PIT histograms, we choose to proceed with the gamma (truncated logistic) distribution model for the NREL M5 (PNW) transformed observations.

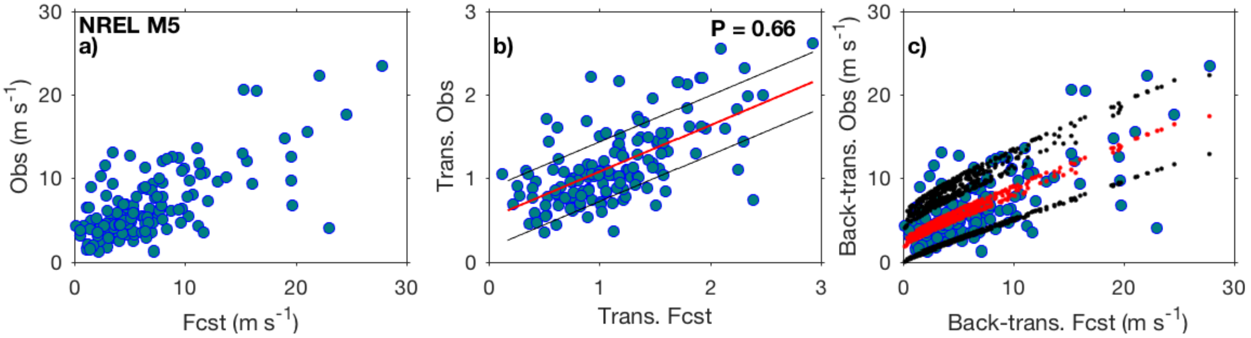

Figure 4.2 Scatter-plots of (a) observations (Obs) versus forecasts (Fcst), (b) unit-less transformed observations versus transformed forecasts, and (c) the back-transformation of the observations versus the back-transformed forecasts from the NREL M5 tower at an 00Z initialization and a two-hour forecast lead time. The exponent P used in the power transformation is shown in (b). The least-squares linear regression trends (solid red line in (b) and red dots in (c)) and lines representing one standard deviation (solid black line in (b) and black dots in (c)) from the regression lines are displayed for the transformed and back-transformed data.

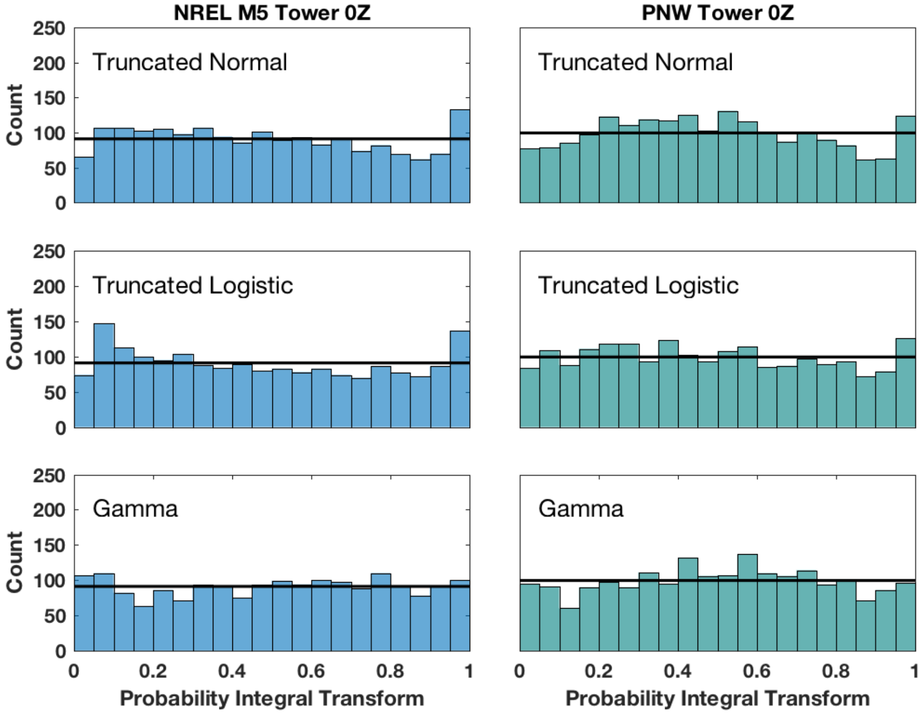

Figure 4.3 Histograms of the probability integral transform (PIT) using the predictive truncated normal, truncated logistic, or gamma distribution models at 00Z for the M5 tower (blue) and PNW tower (green). The horizontal black line depicts the count that each of the twenty bins would have if the histogram was perfectly uniform.

Table 4.1 Average CRPS (in m $s^{-1}$) for the 00Z and 12Z calibrated probabilistic forecasts obtained using the truncated normal ($\boldsymbol{\mathcal{N}_0}$), truncated logistic ($\boldsymbol{\mathcal{L}_0}$), and gamma ($\boldsymbol{\mathcal{G}}$) predictive distribution models. The arrow represents the direction for good scores and the best scores are shown in bold.

| | | NREL M5 | PNW ↓ |
|---|---|---|---|
| $\mathcal{N}_0$ | 00Z | 0.203 | 0.137 |
| | 12Z | 0.234 | 0.157 |
| $\mathcal{L}_0$ | 00Z | 0.203 | **0.136** |
| | 12Z | 0.235 | **0.156** |
| $\mathcal{G}$ | 00Z | **0.202** | 0.137 |
| | 12Z | **0.233** | 0.158 |

### *4.3.3 GENERATION OF FORECAST SCENARIOS: MULTIVARIATE POST-PROCESSING*

We obtain calibrated probabilistic forecasts of transformed wind speed for each verification day and lead time for each initialization and tower by using the truncated logistic or gamma distribution models as discussed in Sect. 4.3.2. These marginal distributions provide prediction uncertainty information for each lead time on a given day and initialization time, but they do not inform about the interdependence structure of the distributions across multiple lead times. Ramp events are changes in power over a short period of time; to identify ramps and the uncertainty associated with them, we need to generate scenarios of wind speed which represent that interdependence structure and can then be converted to scenarios of wind power. We model serial dependence of the individual lead-time predictive distributions to construct forecast scenarios of wind speed which are then converted to power. We utilize four methods to define the interdependence structure and generate the scenarios. The Gaussian copula, Schaake Shuffle, MDSS, and MDSS+ methods are discussed below.

#### 4.3.3.1 Gaussian Copula

We first generate scenarios of wind speed following the Gaussian copula method (Pinson et al. 2009; Pinson and Girard 2012). The Gaussian copula approach first converts the transformed wind speeds (Sect. 4.3.2) from the chosen forecast distribution (here, we use truncated logistic or gamma) into a uniform marginal probability distribution and then converts the uniform values into standard Gaussian-space using a combination of CDFs $F_{\mathcal{D}}$ and inverse CDFs $F_{\mathcal{D}}^{-1}$, where $\mathcal{D}$ is either a gamma $\mathcal{G}(\lambda, r)$, truncated logistic $\mathcal{L}_0(\mu, \sigma)$, or Gaussian $\mathcal{N}(0,1)$ distribution. A flow diagram of the Gaussian copula procedure starting with a marginal gamma distribution is shown in Figure 4.4 and described below. An empirical covariance matrix of the Gaussian values is constructed to estimate the correlation between the Gaussian values from all pairs of lead time. This covariance matrix provides information necessary to transition from marginal distributions for each lead time to multivariate distributions, which inform how the Gaussian values link across multiple lead times. Given the limited amount of training data and gaps in the range of dates for which observations are available, we do not attempt to estimate a time-varying covariance model. Instead, we follow Pinson and Girard (2012) and use a fixed exponential covariance model (ECM),

$$ECM(X_{k1}, X_{k2}) = \exp\left(-\frac{|k_1 - k_2|}{\nu}\right), \tag{4.3}$$

where $X_{k1}$ and $X_{k2}$ are the Gaussian random variables at lead time $k_1$ and $k_2$, respectively, and $\nu$ is the range parameter which controls the extent of correlation of transformed wind speed across lead times. An appropriate value for $\nu$ is selected empirically so that the resultant ECM for a given value of $\nu$ most resembles the decay of the empirical correlation values (Appendix A). A random number generation of the ECM for a given $\nu$ is employed to generate scenarios of multivariate Gaussian-distributed values. Those Gaussian-distributed scenarios are then converted to scenarios with uniform margins by taking the CDF of a standard Gaussian distribution evaluated at the Gaussian-distributed values. An inverse CDF of the forecast marginal distribution (here, we use truncated logistic or gamma) of the uniform values yields the final result of transformed wind speed scenarios with marginal distributions as determined in Sect 4.3.2. For this study, we generate 1000 Gaussian copula scenarios of transformed wind speed. We then convert the transformed scenarios into scenarios of un-transformed wind speeds by reversing the transformation performed in Sect. 4.3.2. A conversion from wind speed to power scenarios is achieved via the International Electrotechnical Commission (IEC) turbine power curve for Class 2 turbines (IEC 2007b) before ramps are identified.

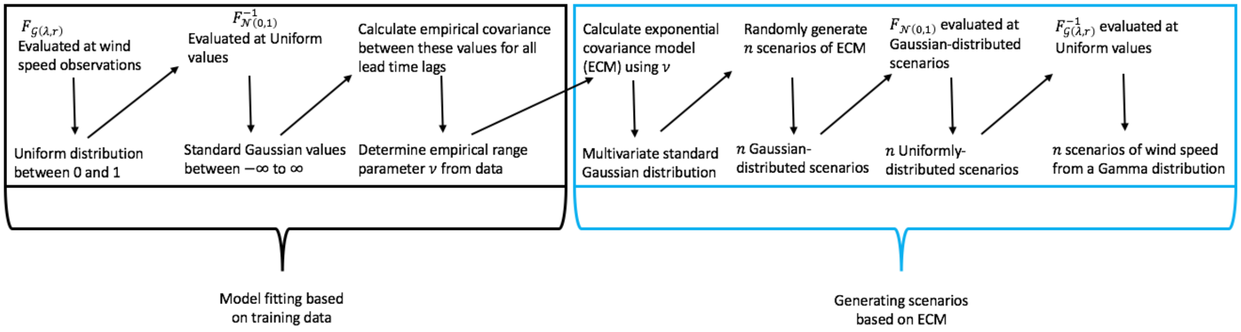

Figure 4.4 Flow diagram of how the Gaussian copula method is used to generate $\boldsymbol{n}$ number of wind speed scenarios from a multivariate Gamma distribution. Downward-pointing arrows show the result of the top processes. The diagonal-pointing arrows illustrate the next step in the method. The original wind speeds do not have to be transformed, but for this study, we begin this method using transformed wind speeds from a univariate Gamma distribution and result in $\boldsymbol{n}$ number of scenarios of transformed wind speeds from a multivariate Gamma distribution.

### 4.3.3.2 Standard Schaake Shuffle

We also generate forecast scenarios of transformed wind speed using the Schaake Shuffle method, which uses historical wind speed scenarios as "dependence templates" for how wind speed varies with lead time. This method for generating multivariate forecasts is used widely for precipitation and temperature forecasts (Clark et al. 2004), but has not yet been applied for wind speed and power forecasts. This method generates wind speed forecast scenarios which can be converted to power. Alternatively, the method could be used to generate power scenarios directly if given predictive distributions and observations of power. Forecast scenarios are easier to visualize in wind-speed-space (transformed wind speed for our data) because of the strong non-linearity of the power curve, so we discuss the method starting with predictive distributions and observations of transformed wind speed. For a given date, we construct 50 forecasts for each forecast lead time by breaking the predictive distributions in Sect 4.3.2 into 50 quantiles so that the $\eta$ forecasts are simply the

$\eta$ quantiles of the predictive distribution. For 50 quantile forecasts, the quantile proportions range from 0.01 to 0.99 of the predictive distribution in increments of 0.02.

The next step in the Schaake Shuffle method is to select an identical number of observed historical scenarios of transformed wind speed. The historical scenarios are selected from the 50 available dates preceding the forecast initialization date, so that the historical scenarios of transformed wind speed are from a similar season. Alternatively, dates could be pulled at random throughout the observed historical record. The method then ranks the 50 historical observations separately for each lead time and assigns the same ranking to the 50 sorted forecast quantiles (an illustration of this process for three historical scenarios and three forecast quantiles is shown in Figure 4.5b, c). The final step of the Schaake Shuffle method is to connect the ranked quantile forecasts across lead times to yield multivariate forecast scenarios (Figure 4.5d). For instance, a forecast quantile that is associated with historical scenario '3' at lead time 0 will connect to all forecast quantiles that are also associated with historical scenarios '3' at their lead time (Figure 4.5d). This shuffling of forecast quantiles to match the rank of historical scenarios yields forecast scenarios that maintain a realistic temporal interdependence and shape across lead time while matching the predictive marginal distribution as described in Sect.4.3.2.

Like in the Gaussian copula method, the generated scenarios of transformed wind speed forecasts from the Schaake Shuffle method can then be converted to power, if desired, to identify ramp events. Here, the selection of the historical scenarios used in the Schaake Shuffle was ad hoc; the method does not make a preferential selection of dates. We next discuss two methods which preferentially choose historical scenarios that are most similar to the 1) quantiles of the forecast marginals and 2) the quantiles of the forecast marginals and also the quantiles of the wind speed difference between lead times. We distinguish between these three methods by referring to the standard method above as the Standard Schaake Shuffle (StSS), the first preferential method which will be discussed below as the Minimum Divergence Schaake Shuffle (MDSS), and the enhanced preferential method also discussed below as the MDSS+.

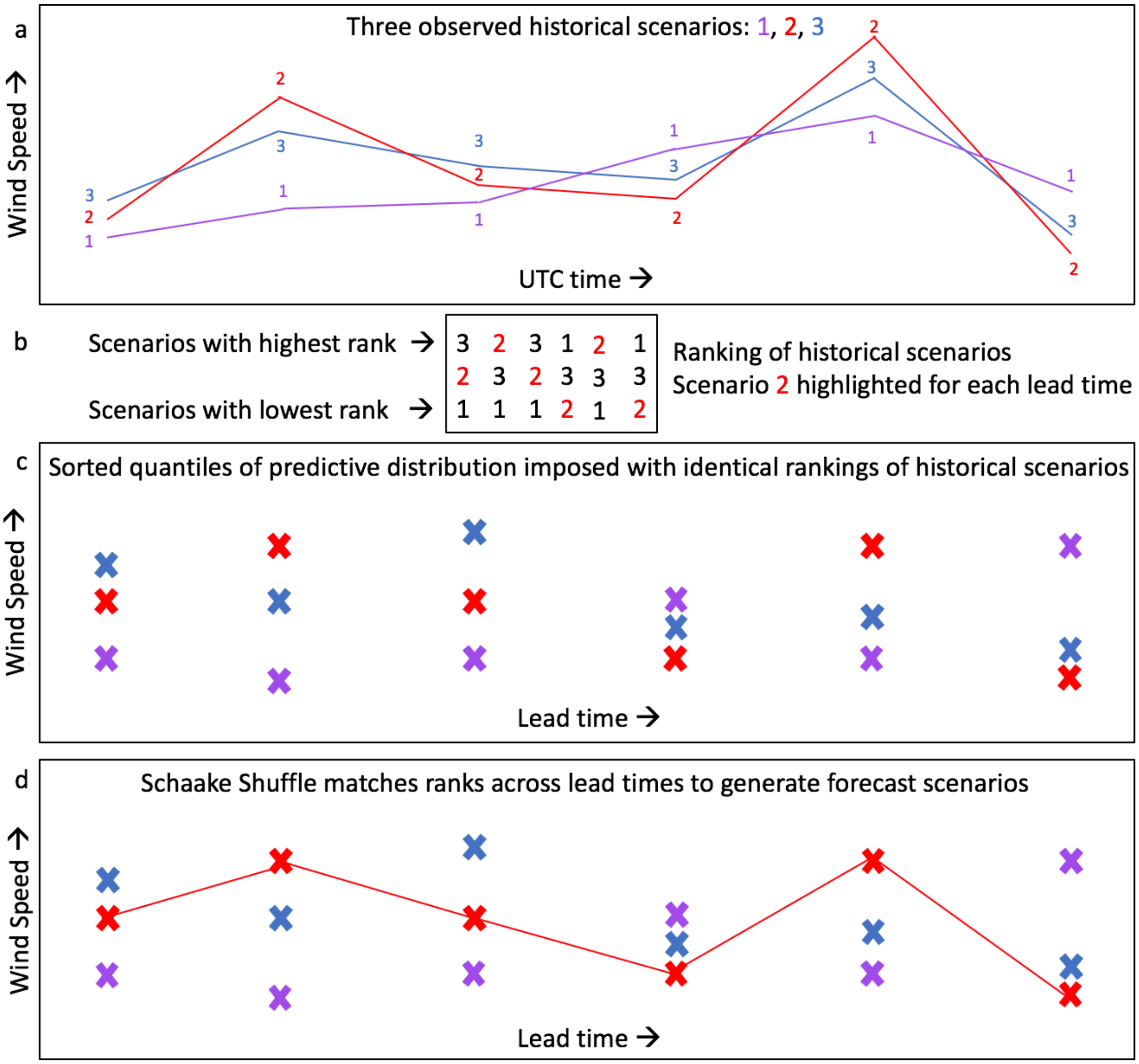

Figure 4.5 Illustration of how the Schaake Shuffle method generates three wind speed forecast scenarios for a given date. For a given forecast date, three observed historical scenarios of wind speed are selected from the historical record (a). The historical scenarios are ranked (b) and then the same ranking is imposed onto the sorted forecast quantiles (c). The forecast quantiles are connected across forecast lead time according to their corresponding rank (d). In panel (b), we emphasize the ranking of the second historical scenario to show how the ranking of a historical event manifests in the shape of a forecast scenario in (d).

### 4.3.3.3 Minimum Divergence Schaake Shuffle (MDSS)

The first of two methods that we use to preferentially select and generate probabilistic forecast scenarios of transformed wind speed is the Minimum Divergence Schaake Shuffle (MDSS) method (Scheuerer et al. 2017) . The MDSS follows the same procedures as the StSS method that impose the ranking of historical scenarios on sorted quantiles of the forecast distributions and that connect forecasted quantiles associated with one particular historical scenario across all lead times. Like for the StSS, the MDSS can also utilize historical observations from dates when no forecasts are available, an advantage over another variant of the Schaake Shuffle method introduced in Schefzik (2016). The identical processes of the StSS and MDSS methods are shown in Figure 4.5. The MDSS deviates from the StSS in its selection of historical scenarios; the MDSS preferentially chooses dates such that the marginal distributions of the sampled historical scenarios are most similar to the quantiles of the post-processed forecast marginal distributions across all forecast lead times rather than a random or user-assigned selection of dates used for the StSS method. In the hydrological context discussed by Scheuerer et al. (2017), this preferential selection helped preserve features in the historical scenarios during the shuffling procedure shown in Figure 4.5c and d, and lead to improved multivariate probabilistic forecasts compared to StSS.

Because historical scenarios selected for the MDSS method are not limited to the most recent $\eta$ scenarios from the forecast initialization date as with the StSS method, the number of scenarios must be narrowed-down to $\eta$ scenarios starting from the total number of candidate scenarios $N_0$ in the historical record, which for our dataset is $\approx 300-400$ scenarios for each initialization time and tower location. This selection seeks the $\eta$

historical scenarios that yield the least divergence[2] $\Delta_k^{\mathcal{H}}$ between the CDF of the forecast marginal distribution $F_k^f$ at each lead time $k$, and the empirical CDF $F_k^{\mathcal{H}}$ calculated from a set $\mathcal{H}$ of historical observation scenarios,

$$\Delta_k^{\mathcal{H}} = \int \left(F_k^{\mathcal{H}}(x) - F_k^f(x)\right)^2 dx. \tag{4.4}$$

Each scenario within the set $\mathcal{H}$ is evaluated for final selection based on whether the scenario results in a larger or smaller total divergence $\Delta_{tot}^{\mathcal{H}} = \sum_k \Delta_k^{\mathcal{H}}$ when it is removed from the calculation. If the scenario results in a smaller divergence when it is left out of the computation, then it is not an optimal choice. Conversely, if leaving out the scenario results in a larger divergence, then we know that the scenario is important for minimizing the divergence and should be kept as one of the final $\eta$ scenarios. Ideally, a set $\mathcal{H}$ that includes all possible candidate scenarios would be reduced to size $\eta$ one-by-one, but this is computationally expensive. Therefore, we use a sequence of $\mathcal{H}$ that reduces the starting number of candidate scenarios to test and eliminates more than one scenario with each iteration until $\eta$ scenarios are reached. For example, for the M5 tower location at initialization time 00Z, there are $N_0 = 416$ total candidate historical scenarios, but we use the sequence 350, 300, 250, 200, 180, 150, 140, 130, 120, 100, 80, 70, 65, 60, 55, $\eta$, which reduces $N_0$ to $\eta = 50$ historical scenarios in 15 iterations rather than $N_0 - \eta$ iterations.

---

[2] Divergence in this study means the integral of the squared difference between two CDFs and is different from the divergence term $\nabla \cdot \boldsymbol{F}$ commonly used in meteorology, where $\nabla$ is the del operator and $\mathbf{F}$ is a meteorological field.

Coding details of the method are given by (Scheuerer et al. 2017) along with a computationally-efficient method for calculating the integral.

#### 4.3.3.4 Enhanced Version of the Minimum Divergence Schaake Shuffle (MDSS+)

Constraining the marginal distributions does not necessarily improve the representation of temporal gradients of the quantity of interest. If the HRRR forecasts of wind speed *differences* have some skill, then using a predictive distribution of these differences explicitly in the MDSS algorithm might result in a better selection of historical dates that have similar temporal gradients. This formulation is the idea behind the final method we use to generate transformed wind speed scenarios. The final method is much like MDSS, but includes an additional term to explicitly capture the variation in wind speed between neighboring forecast lead times. For this enhanced MDSS method, $\eta$ historical scenarios are chosen that yield the least divergence from both the forecast marginal distributions and the forecast distribution of the lag1-h lead time differences of transformed wind speed. Forecast distributions of lag 1-h lead time differences are attained in the same way as forecast marginal distributions (Sect. 4.3.2), except that now we perform a regression on lag 1-h difference of transformed wind speed. Based on PIT histograms (not shown), the best predictive distribution that represents these differences for both tower locations is the (non-truncated) logistic distribution. For this method, the $\eta$ historical scenarios that yield the smallest divergence when considering both the forecast marginal distributions and the forecast distributions of wind-speed differences are selected. To emphasize the temporal gradient between two neighboring lead times, we assign more weight to the divergence term associated with wind speed differences. In this study, we weight the wind speed difference term as five times greater than the marginal distribution term. This method requires that the lag 1-h difference between lead times in the historical scenarios best-match the lag 1-h differences of the forecast and is therefore an enhanced method to the MDSS.

#### 4.3.3.5 Differences Between Historical Observations Selected by StSS, MDSS, and MDSS+

Marginal distributions of transformed wind speed of the historical scenarios used for each of the three Schaake shuffle methods (Figure 4.6a) and the distributions of the lag 1-h differences of those scenarios (Figure 4.6b) reveal that the MDSS and MDSS+ produce historical scenarios closer to the forecasted distributions than does the StSS method. Of course, the MDSS+ is the only multivariate method that utilizes the lag 1-h differences when selecting historical scenarios and for that reason, we see that the MDSS+ distributions for the lag 1-h differences (green boxes in Figure 4.6b) are often a slightly better match to the forecasted distribution (grey boxes in Figure 4.6b) than the regular MDSS or StSS methods (pink and blue boxes in Figure 4.6b, respectively). The MDSS+ method sometimes makes compromises in the selection of optimal scenarios for one of its two terms, because it seeks to find the historical scenarios that are an overall best match when considering both the quantiles of the forecasted transformed wind speed distribution and the distribution of lag 1-hr differences of those wind speeds. Also, the MDSS and MDSS+ methods only have a limited set of historical dates from which they can choose scenarios, so we cannot expect a perfect match. Once the historical scenarios are chosen, the quantiles of the forecast marginal distributions are reordered to have the same ranking of the corresponding historical scenarios. Like for the Gaussian copula and StSS methods, both the MDSS and MDSS+ scenarios are then transformed back into wind-speed-space and converted to power before identifying ramp events.

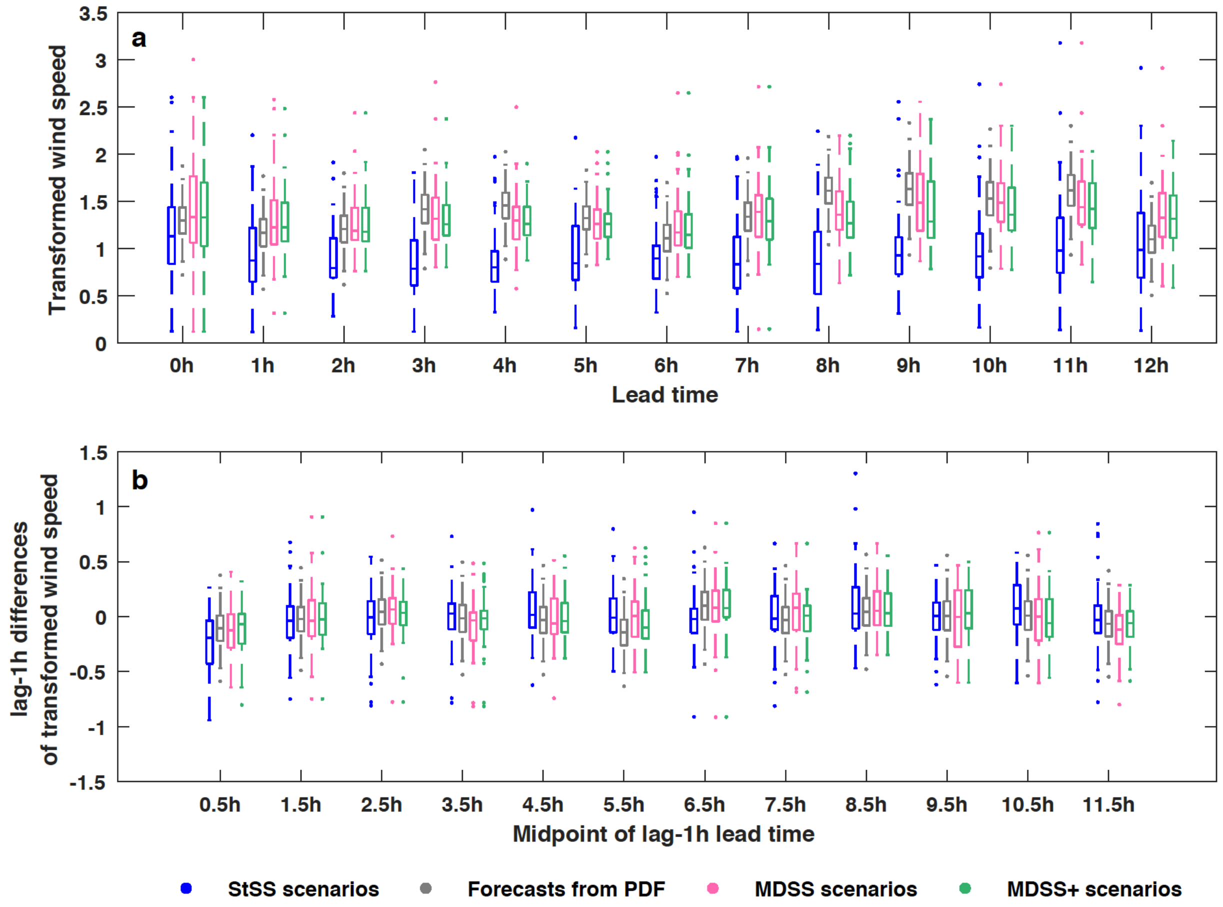

Figure 4.6 Box plots of a) the forecast marginal distributions of transformed wind speed (grey boxes) and b) forecast lag 1-hr wind speed differences (grey boxes) for 00Z forecast initialization on 28 March, 2015 at the PNW tower location. Distributions of transformed wind speed and lag 1-hr differences in transformed wind speed from the 50 historical scenarios used by the StSS (blue boxes) and selected by the MDSS (pink boxes) and MDSS+ (green) methods are also shown. The box plots display the outliers (dots), minimum and maximum (lower and upper whisker, respectively), the interquartile range (rectangle region), and the median (middle line within rectangle) of the distributions.

## 4.4 RESULTS

### *4.4.1 VERIFICATION OF DETERMINISTIC HRRR FORECASTS WITH OBSERVATIONS*

To provide a baseline of performance of predicting up- and down-ramp events, we first illustrate how ramps identified from the raw HRRR forecasts compare to those identified from the observations at the M5 and PNW tower locations. The correlation between ramps identified with the HRRR forecasts and observations are low at both tower locations (Figure 4.7) ranging between 0.23 and 0.37. The ramp definition used for Figure 4.7 is different from the ramp definition discussed in Sect.4.3.1, because it shows ramps identified with wind speed instead of power. This ramp definition is only used in Figure 4.7 to show the magnitude of the change in wind speed that is observed and forecasted at each tower location during a period of three hours. Utilizing the magnitude directly - rather than a particular exceedance event - eliminates the need to set any particular threshold for a change in wind speed, which would be difficult to define anyway because of the nonlinear relationship between wind speed and the power curve. The purpose of Figure 4.7 is to reveal biases in the HRRR forecasts and differences between the two tower sites, while the analysis of power ramp events in the subsequent sections is more applicable for decision-making of power grid operations.

At the M5 tower site, the HRRR predicts stronger wind speed ramps compared to observations; forecasted wind speed ramps $\geq 5$ m $s^{-1}$ make up 40% of the total number of up- and down-ramps while the observed ramps of the same magnitude only make up 33% of the total number of ramps. The HRRR generally under predicts the magnitude of wind speed ramps at the PNW site; observed wind speed ramps $\geq 5$ m $s^{-1}$ make up 18% of the total number of up- and down-ramps while the forecasted ramps $\geq 5$ m $s^{-1}$ only contribute to 9% of the total number of ramps. These percentages also highlight that the M5 location has a greater percentage of observed ramps of the same magnitude than at the PNW location (33% vs 18%), suggesting that the wind speeds at the M5 site are more variable than at the PNW site. The M5 tower is located in a region of very complex terrain about 5 km east of the Colorado Front Range, which because of the atmosphere's interaction with the mountainous terrain can cause large changes in wind speed over short periods of time. The PNW tower is also located in a region of complex terrain near the Columbia River Gorge, but the terrain is not as complex as the M5 site.

The low correlation coefficients between the HRRR forecasts and observed wind speed ramps suggest that there is some skill in the HRRR forecasts at predicting ramps, but the skill is limited and differs between up- and down- ramps. Low correlation limits the extent to which statistical post-processing can improve the forecast. On the other hand, we have shown that systematic over- and under-forecasting biases can be reduced with statistical post-processing. Moreover, the multivariate methods discussed in this paper can provide information about the uncertainty of the forecast via generation of many possible wind speed scenarios.

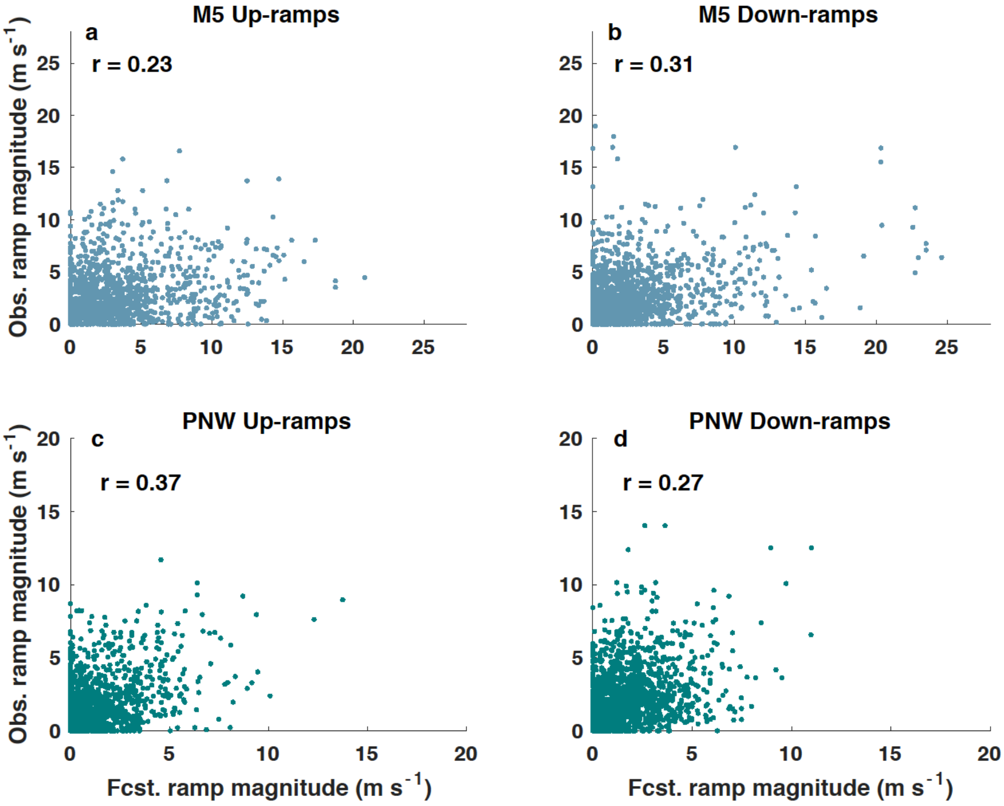

Figure 4.7 Observed (Obs.) and HRRR-forecasted (Fcst.) wind speed ramps during sliding 3-h time windows over a period of 12 hours. Absolute values of the ramp magnitudes are shown. Wind speed ramps are plotted for every sliding 3-h time window starting at 00Z and for both the M5 (a, b) and PNW (c, d) tower locations. The correlation coefficient, r is displayed for each tower location and type of ramp.

### *4.4.2 VERIFICATION OF MULTIVARIATE METHODS COMPARED WITH HRRR FORECASTS*

We now compare the various multivariate methods used to generate scenarios of transformed wind speed. To make use of the ≈ 21 months during which both the HRRR forecasts and observations are available, we cross-validate these data. We leave one month out for verification and fit the statistical models used to determine the parameters of the predictive distributions with the remaining 20 months of data. We repeat this process so that 21 months of forecasts and independent verifying observations are obtained for each month, forecast initialization, lead time, and tower location. To also compare the different methods to the deterministic raw HRRR forecasts, we first employ an event-based metric to assess systematic biases with regard to the frequency of ramp events. This metric counts the number of power ramps defined as in Sect. 4.3.1 identified from the scenarios generated by each method described in Sect. 4.3.3. The relative frequency of power ramps that exceed $\xi = 60\%$ change in power capacity during 6 h for all days when forecasts and observations are available (Figure 4.8) represents a climatology of up- and down-ramps for each tower location. The number of ramps identified in each 6-h window of time for each of the 50 scenarios (1000 scenarios for Gaussian copula method) were averaged together and plotted as a single line in Figure 4.8. We again see a general over-forecasting bias of the number of ramp events (this time power ramps) produced by the raw HRRR forecasts compared to observations at the M5 tower (Figure 4.8c, d) and the opposite behavior of the HRRR forecasts at the PNW tower (Figure 4.8a, b). The HRRR forecasts especially struggled with the diurnal cycle and magnitude of the relative frequency of up- and down-ramps at the PNW location. The HRRR predicted the most up-ramps in the first four ramp windows (between 00Z and 9Z) and then levelled out for the remainder of the early morning while the observations show a minimum in up-ramps during the first four ramp windows and a maximum during the remaining windows, which suggests that the HRRR incorrectly captured the diurnal cycle. For the down-ramps, the HRRR forecasted a gradual increase in ramp events across all ramp windows, while the observations show a peak in down-ramps around the fourth ramp window (≈ 9Z) followed by a gradual decrease in down-ramp events during the remainder of the morning.

The method that most-closely follows the ramp climatology of the observations (black line in Figure 4.8) is the StSS method followed by the MDSS+, MDSS, and lastly the

Gaussian copula method. The StSS method has an overall better prediction of up- and down-ramp climatology than the raw HRRR forecasts when compared to a climatology of observed ramp events. As discussed in Sect.4.3.3, the MDSS and MDSS+ methods make a preferential selection of historical scenarios that minimize the divergence between the post-processed forecast and past scenarios and should yield scenarios more similar to the current forecast than the random or assigned scenarios used in the StSS method. Despite this preferential selection, the MDSS and MDSS+ methods do not outperform the StSS method in predicting the climatology of relative frequency of ramp events. Next, we will examine a metric used to compare the skill of various probabilistic forecast methods to determine the differences in performance between the StSS and two MDSS methods.

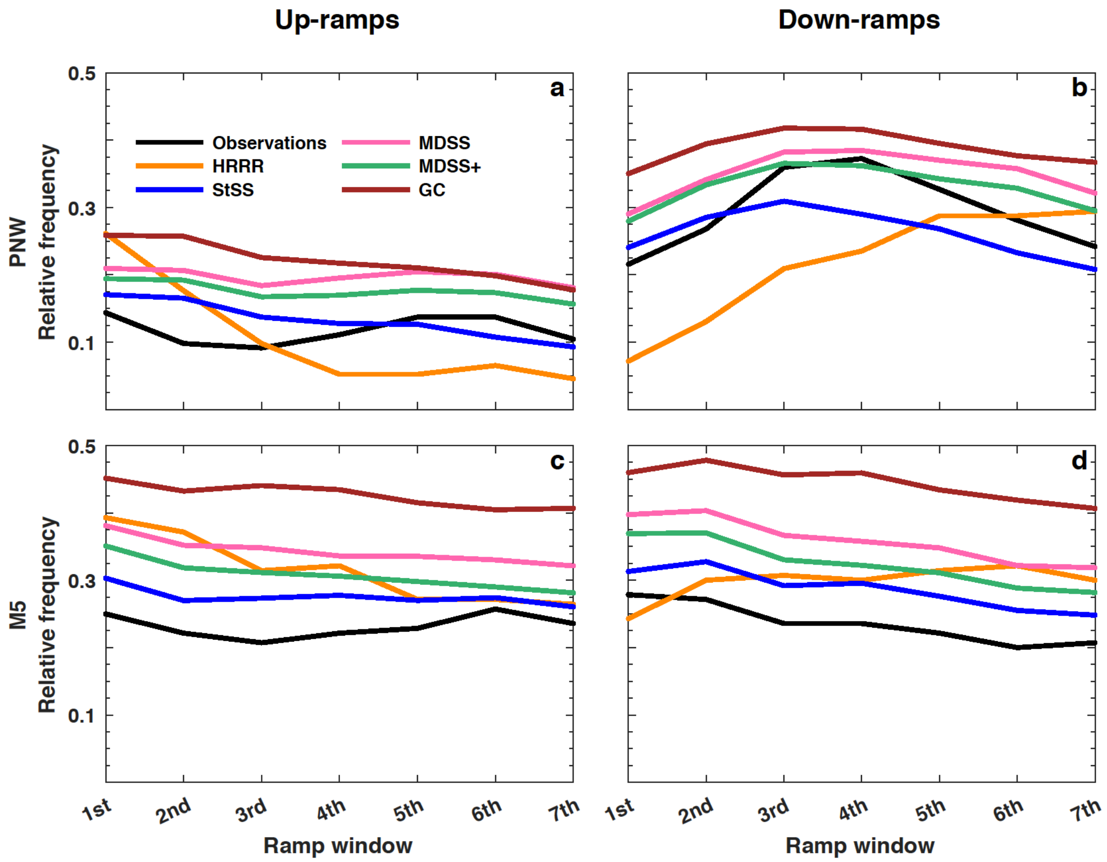

Figure 4.8 Relative frequency of up-ramps (a, c) and down-ramps (b, d) identified with ≥ 60% change in power capacity during each 6-h time period (i.e., ramp windows) starting at 00Z. Relative frequencies of observed ramps (black lines) and forecasted ramps from the HRRR model (orange lines) are shown for the PNW (a, b) and M5 (c, d) tower locations. Relative frequencies are also shown for the four different multivariate methods: standard Schaake Shuffle (StSS, blue lines), Minimum Divergence Schaake Shuffle (MDSS, pink lines), enhanced Minimum Divergence Schaake Shuffle (MDSS+, green lines), and Gaussian Copula (GC, brown lines).

The StSS, MDSS, MDSS+, and the Gaussian copula methods produce probabilistic forecasts of ramp events. To verify the skill of and compare among the different probabilistic methods, we compute Brier Skill scores (BSS). The Brier skill score quantifies the extent to which a forecast method improves the prediction of a two-categorical event compared to a reference forecast,

$$BSS = -\frac{BS_{fcst}-BS_{ref}}{BS_{ref}}, \tag{4.5}$$

where $BS_{fcst}$ is the Brier score of the forecast and $BS_{ref}$ is the Brier score of the reference forecast. The Brier score is a strictly proper score that summarizes the accuracy of a probabilistic forecast; it is defined as the squared error of the probability forecast of an event and the observed binary outcome (1 if the event happened, 0 if not). The events here are characterized by the exceedance of a particular ramp threshold $\xi$ during a ramp window size $h$. Climatological probabilities of occurrence of up- and down-ramp events with a particular $\xi$ and $h$ are used as the reference forecast. Before calculating the $BS_{fcst}$, we took the average of the binary event forecasts from all 50 scenarios (1000 scenarios for Gaussian copula method) for each method to create a probabilistic forecast with a value between 0 (no ramps occurred in any of the scenarios) and 1 (ramps occurred in all of the scenarios). Brier scores were calculated for each type of ramp (i.e., up- and down-ramps with $\xi$ = 0.20, 0.40, 0.60, and 0.80 and $h$ = 3 h and 6 h). To quantify the sampling variability of the BSS induced by the limited data sample size, we first generated 100 bootstrap samples with replacement of the daily $BS_{fcst}$ and $BS_{ref}$ separately for each forecast initialization time (i.e., 00Z and 12Z). Then, we summed the 100 BS from each initialization time together before calculating the BSS to reduce sampling variability.

Box plots of the BSS for both tower locations and different types of power ramps reveal dependencies of the forecast skill on $\xi$, $h$, and tower location (Figure 4.9 and Figure 4.10). The most noticeable difference among the BSS is that the skill is generally higher for forecasts made at the PNW tower location compared to those at the M5 tower location for all types of ramps. Recall from Sect. 4.4.1 that the raw HRRR forecasts at the M5 location greatly over-predicted the magnitude of the up- and down-ramps leading to low correlation coefficients, which is why it is difficult to get positive skill with any of the methods at the M5 site; statistical post-processing can correct for systematic forecasting biases, but it cannot improve random errors which lead to low correlation. Conversely, at the PNW site, there are overall higher correlation values (Figure 4.7) compared to those at the M5 site meaning that statistical post-processing will be more consequential. This behaviour results in generally positive and higher BSS for the PNW site than for the M5 site (Figure 4.9 and Figure 4.10). Greater positive skill is gained when we identify ramps in a window size of 6 h (Figure 4.10) instead of 3 h (Figure 4.9) for both the PNW and M5 sites, because timing errors are less consequential when the time window is larger.

The multivariate methods do not present as much skill in forecasting down-ramps as they do in forecasting up-ramps at the PNW site, except for events with small (20%) power changes during 3 h. In Figure 4.7, the correlation between observed ramps and ramps forecasted by the HRRR is greater for up-ramps (0.37) than down-ramps (0.27) at the PNW site. At the M5 site, the correlation between observed and HRRR-forecasted down-ramps (0.31) is larger than for up-ramps (0.23). We also note greater skill for the multivariate methods at predicting down-ramps opposed to up-ramps at the M5 site, which combined with the relative skill of up- and down-ramps at the PNW site suggests that the quality of the initial raw forecast skill impacts the amount of skill that can be gained from the probabilistic approaches.

How does skill vary among the different multivariate methods? The scenarios produced with the Gaussian copula method result in significantly less skill than all of the other methods for the M5 tower location and marginally less skill than the other methods at the PNW site. The Gaussian copula utilizes an exponential covariance model that defines the temporal dependence of scenarios through the range parameter $\upsilon$, which was set to 2.5

and 1.5 for the PNW site and M5 site, respectively. Those parameters were selected based on empirical correlations, but did not yield the highest BSS. Instead, we achieved the highest BSS using $\upsilon = 3.5$ and 2.5 (not shown) for the PNW and M5 site, respectively, but these values are not apparent choices based on what the data suggest. The fact that a larger parameter produces a better result implies that a generic exponential model may not be a good fit for these complex sites; the inclusion of local forecasts to create probabilistic scenarios is necessary to understand the correlation among lead times.

The most surprising result from the analyses is that the StSS method is more competitive than the MDSS method (and slightly more competitive than the MDSS+ method) despite the preferential selection of historical scenarios made by the MDSS method. The MDSS method selected historical scenarios of transformed wind speed that were most compatible with the marginal distributions of the forecast day and theoretically should provide higher BSS than the StSS method, which only could use scenarios from the 50 available historical dates prior to the forecast day. The original MDSS method used by Scheuerer et al. (2017) worked well for precipitation events, but does not focus on the selection of historical scenarios based on their compatibility with forecasted (temporal) gradients, which are crucial for the prediction of ramps. This understanding led us to include an additional term in the MDSS method that is based on lag 1-h differences of transformed wind speed. The modified MDSS method MDSS+, matches historical scenarios to not only the forecast marginal distributions but also to the forecast distributions of lag 1-h differences. The term of lag 1-h differences ensures a better selection of historical scenarios with ramps of similar slope or magnitude to the forecast.

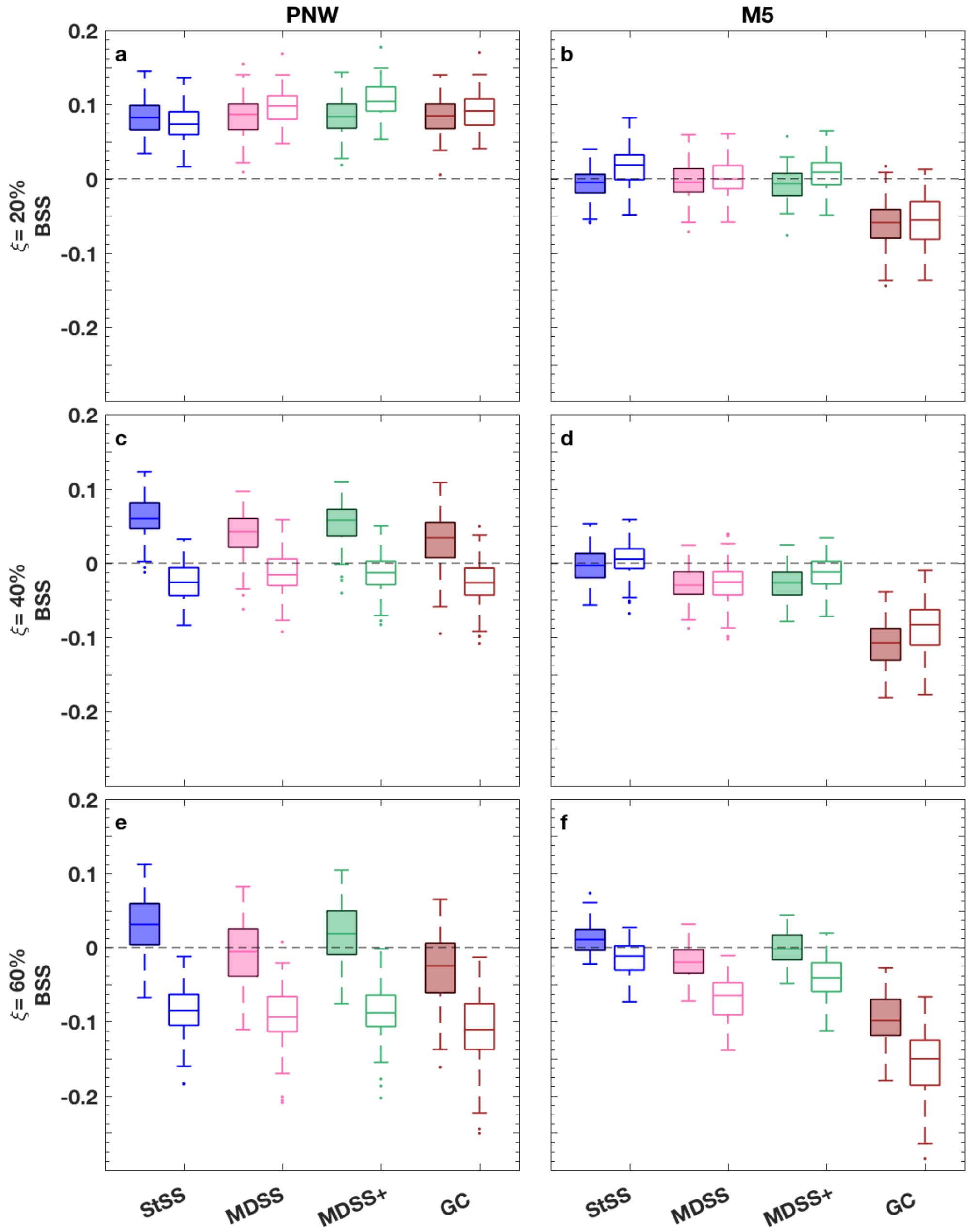

Figure 4.9 Box plots of Brier skill score (BSS) of power ramp events identified in 3-h time windows from forecast scenarios generated with the StSS (blue), MDSS (pink), MDSS+ (green), and Gaussian copula (GC, brown) methods. BSS are shown for the PNW tower location (a, c, and e) and the M5 tower location (b, d, f) and for up-ramps (filled boxplots) and down-ramps (non-filled boxplots). Ramp events with a power threshold of $\boldsymbol{\xi}$ = 20% (a and b), 40% (c and d), and 60% (e and f) change of the turbine power capacity are shown. The box plots display the outliers (dots), minimum and maximum (lower and upper whisker, respectively), the interquartile range (rectangle region), and the median (middle line within rectangle) of the distribution of BSS. For reference, a line (black-dashed) showing zero skill is plotted.

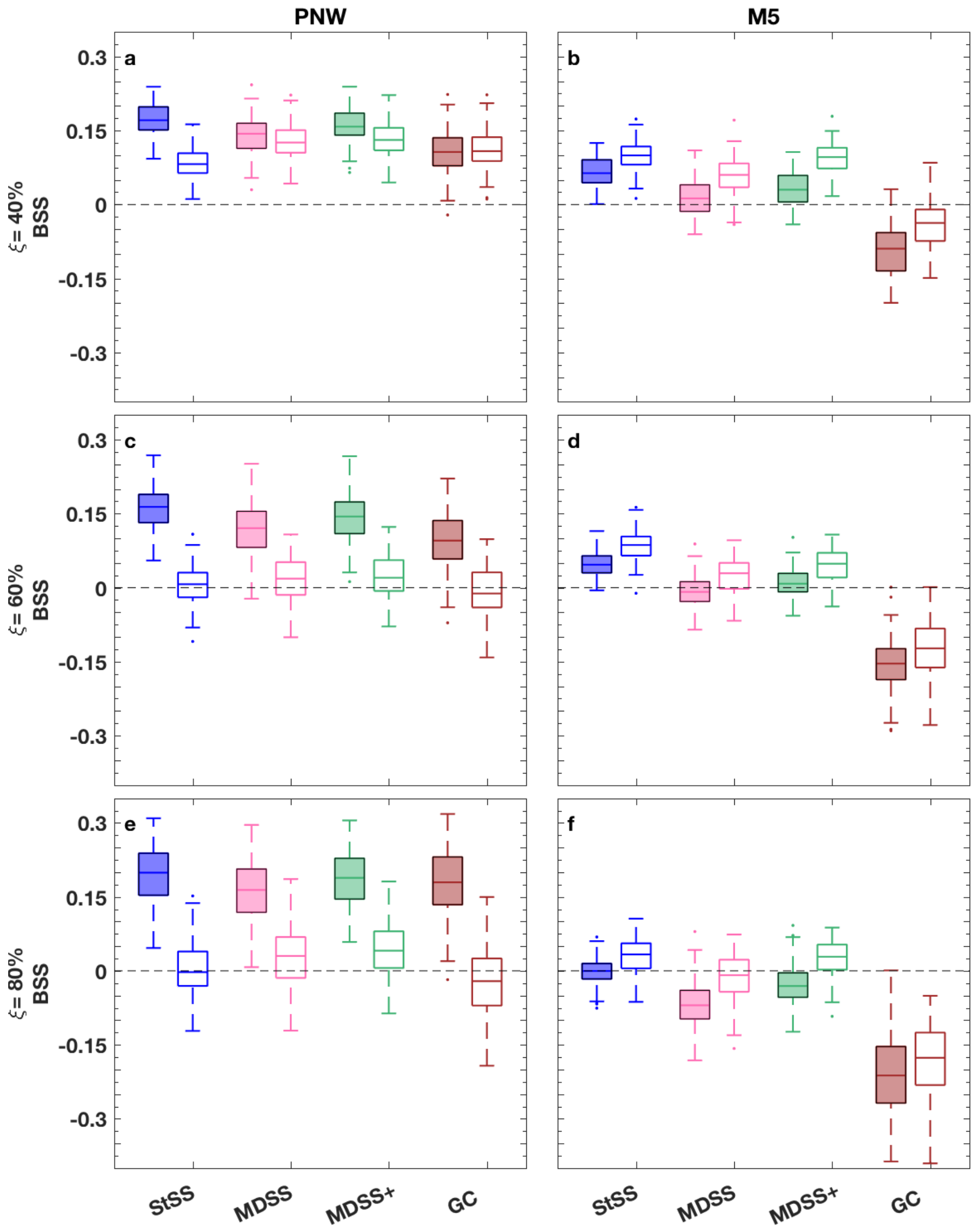

Figure 4.10 Box plots of Brier skill score (BSS) of power ramp events identified in 6-h time windows from forecast scenarios generated with the StSS (blue), MDSS (pink), MDSS+ (green), and Gaussian copula (GC, brown) methods. BSS are shown for the PNW tower location (a, c, and e) and the M5 tower location (b, d, f) and for up-ramps (filled boxplots) and down-ramps (non-filled boxplots). Ramp events with a power threshold of $\boldsymbol{\xi}$ = 40% (a and b), 60% (c and d), and 80% (e and f) change of the turbine power capacity are shown. The box plots display the outliers (dots), minimum and maximum (lower and upper whisker, respectively), the interquartile range (rectangle region), and the median (middle line within rectangle) of the distribution of BSS. For reference, a line (black-dashed) showing zero skill is plotted.

We see that the median BSS using the MDSS+ forecast scenarios are often higher than those of the MDSS method and more competitive with the StSS method for all ramp types (Figure 4.9 and Figure 4.10). However, minute difference between the three Schaake shuffle methods are unperceivable, because of the limited sample size which resulted in considerable overlap between the BSS boxplots. To highlight the differences between the three Schaake Shuffle methods, we generated 25 years of synthetic wind speed observations and forecasts (Appendix B). These synthetic data underwent the same univariate post-processing steps (Sect. 4.3.2) as the real data before applying the different Schaake shuffle methods.  Box plots of BSS using the synthetic data present positive skill, show considerably less variability than the real data, and highlight the differences between the MDSS and MDSS+ methods (Figure 4.11).  The inclusion of the lag 1-h differences in the MDSS+ is essential to achieve optimal and competitive skill from the method when compared to StSS. Recall that the lag 1-h differences are weighted five times more than the forecast marginal distributions in the MDSS+ meaning that the transformed-wind-speed gradient between lead times is even more important to match than the forecast marginal distributions. With this additional term, the MDSS+ is as competitive as the StSS method at choosing scenarios that lead to skillful ramp forecasts.

Why is the rather simplistic StSS method as good (even better in regards to ramp frequency biases, see Figure 4.8) as the more sophisticated MDSS+ and significantly better than the MDSS method? Some insight is gained by analysing the lag 1-h differences of wind speed forecasts generated by the three different Schaake Shuffle techniques. We compute absolute lag 1-h differences of observed wind speeds and those of the historical observed wind speed scenarios selected by the StSS, MDSS, and MDSS+ methods before shuffling. For each method, the absolute lag 1-h differences are calculated for each date and for each

12 pairs of lead times. For each date and paired lead time, the lag 1-h differences are then stratified according to the corresponding HRRR wind speed forecast. Lag 1-h differences from all dates and paired lead times associated with a certain range of HRRR forecasted wind speeds are then averaged together before plotting (Figure 4.12a). A dependency between the magnitudes of lag 1-h differences and HRRR wind speed forecasts emerge. The magnitude of the observed lag 1-h differences increases as the HRRR forecast wind speed increases, which suggests that higher wind speeds correspond to larger fluctuations in wind speed. Because the StSS method does not depend on the HRRR forecast to select historical scenarios, the lag 1-h differences of the StSS historical scenarios are independent of the magnitude of the HRRR forecast wind speed. This result is demonstrated by the relatively flat StSS (blue) curve in Figure 4.12a. Conversely, the MDSS and MDSS+ methods make a preferential selection of past observations based on the current HRRR forecast wind speed. The result is that the MDSS and MDSS+ methods produce curves (pink and green lines, respectively in Figure 4.12a) of lag 1-h differences qualitatively similar to the observed curve (black line in Figure 4.12a).

This better initial selection of scenarios, however, is offset by the effects of the shuffling procedure. Panel b) in Figure 4.12 shows the ratio of mean absolute lag 1-h differences before and after shuffling. For the StSS, the shuffling makes the lag 1-h differences more similar to the observed lag 1-h differences; lag 1-h differences decrease for low HRRR forecast wind speeds and increase for high HRRR forecast wind speeds during the shuffling procedure. For the MDSS and MDSS+ methods, shuffling always results in a slight increase of the magnitudes of lag 1-h differences (pink and blue lines in Figure 4.12b). This increase after shuffling the scenarios explains why the MDSS and to a lesser extent, the MDSS+ have a tendency to over-forecast the magnitude and frequency of wind speed ramps (see Figure 4.8).

Lastly, we investigate why the shuffling procedure affects the historical StSS scenarios differently than the MDSS and MDSS+ scenarios. We conjecture that one of the reasons for this effect is the difference in spread of the scenarios used by each method. We quantify the spread as the mean absolute difference between the historical scenarios. Since the historical StSS scenarios are chosen unconditionally, the spread of its marginal distribution (see blue line in Figure 4.12c) approximates the climatological spread of actual observed wind speeds. Preferential selection performed by MDSS and MDSS+ significantly decreases the spread of the historical marginal distributions with the exception for high HRRR wind speed forecasts where the prediction uncertainty can exceed the climatological spread. This initial reduction in spread, however, reduces a side effect entailed by StSS: the shuffling procedure squeezes together scenarios as the unconditional spread is transformed into a forecast-informed spread. By doing this, the shuffling procedure typically reduces the fluctuations present in the historical scenarios. Since the MDSS and MDSS+ historical scenarios already have low spread, shuffling does not change their characteristics as much as it does for the StSS historical scenarios; the level of fluctuations is similar before and after shuffling. In other setups, the shuffling side effect can be unwanted, but in the present setup, it seems to benefit the StSS method and results in the overall most accurate level of wind speed fluctuations.

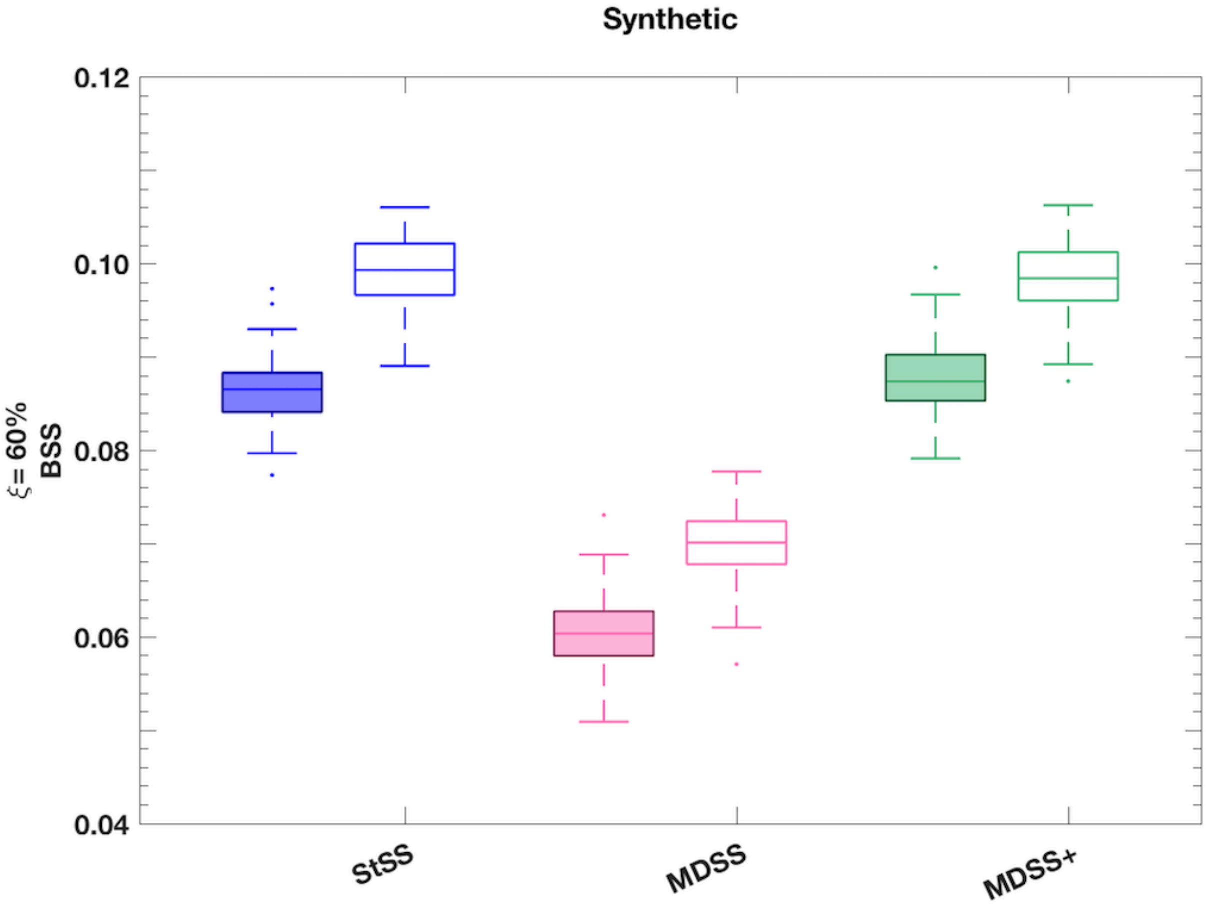

Figure 4.11 Box plots of Brier skill score (BSS) of power ramp events identified in 6-h time windows from synthetic forecast scenarios generated with the StSS (blue), MDSS (pink), and MDSS+ (green) methods. BSS are shown for the PNW tower location for up-ramps (filled boxplots) and down-ramps (non-filled boxplots). Ramp events with a power threshold of $\boldsymbol{\xi}$ = 60% change of the turbine power capacity is shown. The box plots display the outliers (dots), minimum and maximum (lower and upper whisker, respectively), the interquartile range (rectangle region), and the median (middle line within rectangle) of the distribution of BSS.

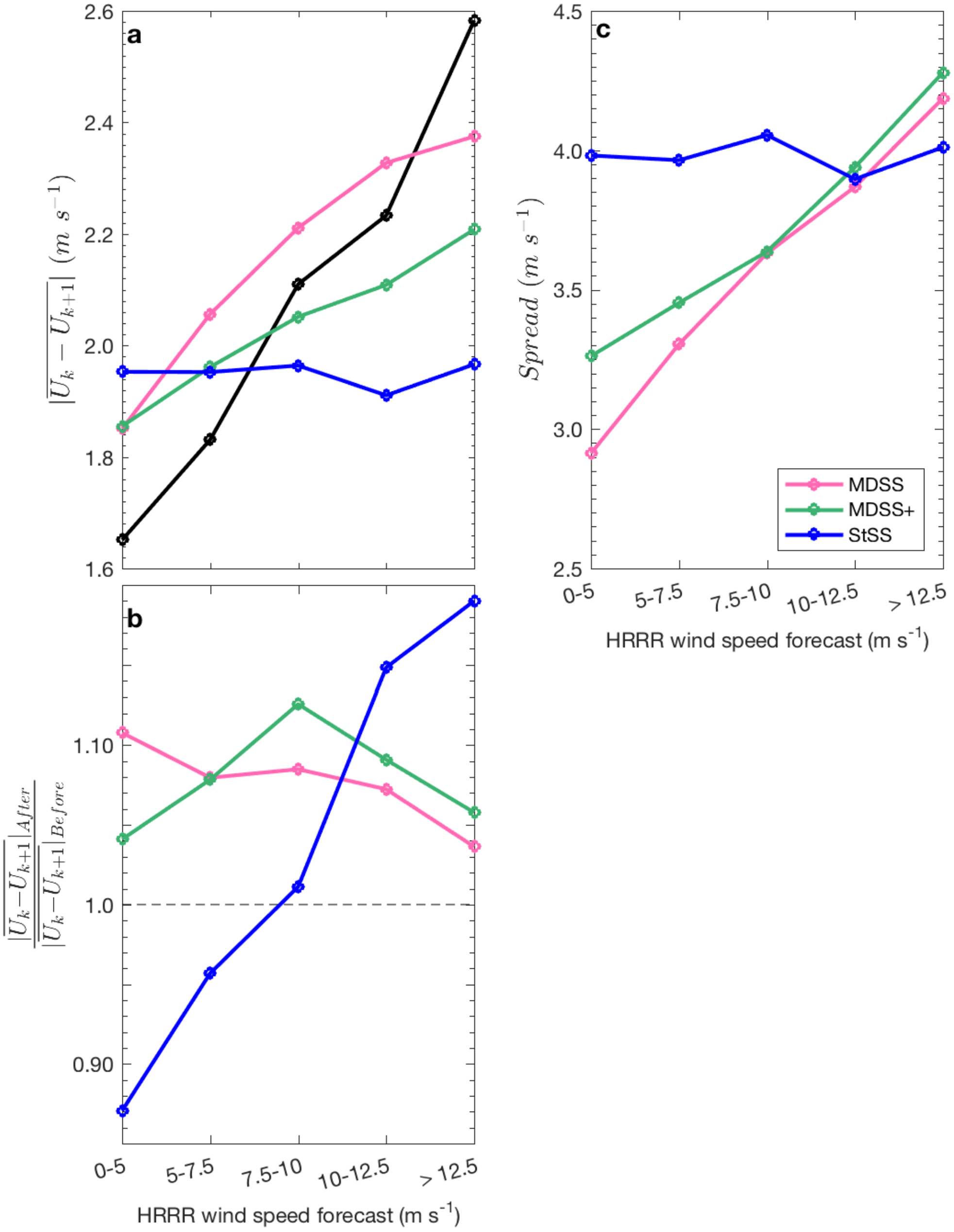

Figure 4.12 Statistics of observed wind speeds ($\boldsymbol{U}$), unshuffled historical observed wind speed scenarios used by each Schaake Shuffle method, and the shuffled wind speed forecast scenarios stratified according to the magnitude of the HRRR wind speed forecasts at the respective time. Mean absolute lag 1-h wind speed differences ($|\overline{\boldsymbol{U_k - U_{k+1}}}|$) of observations and historical scenarios (a), ratios of mean absolute wind speed differences after ($|\overline{\boldsymbol{U_k - U_{k+1}}}|_{\boldsymbol{After}}$) and before ($|\overline{\boldsymbol{U_k - U_{k+1}}}|_{\boldsymbol{Before}}$) the shuffling procedure (b), and the marginal spread of the unshuffled historical scenarios (c) are shown. The spread is quantified as the mean absolute difference between scenarios.

## 4.5 SUMMARY AND CONCLUSION

Wind power ramps present challenges to wind power forecasters and the electrical grid, because they cause sharp changes in power production in time periods of minutes to hours. Better forecasts of ramp events can lead to more reliable wind power generation and less strain on the power grid. Generally, wind farm operators rely on a single forecast of persistence to determine power fluctuations over the next 30 mins to an hour, which is not suitable during ramp events. Numerical weather prediction and statistical post-processing techniques can improve ramp forecasts by predicting rapid future fluctuations in wind speed and power and by providing uncertainty information to those forecasts.

In this paper, we used 21 months of observed 80-m wind speeds from tall meteorological towers located in Boulder, Colorado (M5 site) and in eastern Oregon (PNW site). We also used forecasts of 80-m wind speeds from the HRRR model to create probabilistic forecasts of up- and down-ramp events. With these data, we presented how to obtain probabilistic wind speed forecasts by first correcting biases in the forecasts and then applying one of the four multivariate methods discussed to generate scenarios of wind speed. We used the IEC power curve to convert scenarios of wind speed to scenarios of power before identifying ramps. Employing stochastic power curves (Jeon and Taylor 2012) would also take the conversion uncertainty into account. Because our study was focused on the evaluation and comparison of multivariate statistical post-processing methods and wind speed to power conversion affects all methods in the same way, using a fixed power curve warrants a fair comparison. If observed power production rather than observed wind speed was used as the 'ground truth', an inverse (power-to-wind speed) transformation could be employed to reconstruct the associated wind speeds (Messner et al. 2014), and the conversion uncertainty would be accounted for implicitly.

Before generating the scenarios, we removed the seasonal cycle and corrected for heteroscedasticity within the observations and raw HRRR forecasts by applying a power transformation. We then regressed the transformed observations on the transformed forecasts to obtain regression coefficients. The mean and standard deviation of marginal predictive distributions for each forecast initialization and lead time were determined by inserting future forecasts into the fitted regression model with these coefficients. We tested three candidate predictive distributions and found that the gamma distribution and the truncated logistic distributions were the best fits for the M5 and PNW tower locations in regards to wind speed, respectively. We determined that these predictive distribution models were suitable to represent observations based on uniform PIT histograms and low CPRS values. This approach to obtaining marginal predictive distributions is rather simple, but given the limited amount of data that remained after filtering, we thought that a stable parameter estimation for a more complex model was not warranted. A larger training dataset would allow one to account for forecast biases that vary with wind direction (Eide et al. 2017), or to use an analog-based regression approach similar to the method proposed by (Junk et al. 2015), and include analog predictor variables related to atmospheric stability.

The marginal predictive distributions provided uncertainty information for each lead time, but did not inform us about the interdependence structure across all lead times. To construct this interdependence, we first used the Gaussian copula technique following Pinson and Girard (2012), which relates the predictive distributions across all lead times by utilizing an exponential covariance model of Gaussian random variables. We used a random number generator to generate 1000 scenarios of wind speed using this method. The Gaussian copula method is based on parametric assumptions that may not be an adequate representation of the interdependence between observed wind speeds at different lead times, so we tested three new methods of generating scenarios of transformed wind speeds. The standard Schaake Shuffle (StSS), the minimum divergence Schaake Shuffle (MDSS), and the enhanced version of the MDSS (MDSS+) methods all use historical observed scenarios as “dependence templates” to inform how marginal predictive distributions should be connected across all lead times, which results to more realistic forecast scenarios.

The StSS method only used an ad hoc selection of historical scenarios while the MDSS and MDSS+ made preferential selections of historical scenarios that best matched the forecast marginal distributions (MDSS) or matched both the forecast marginal distributions and the forecast distributions of the lag 1-h differences of transformed wind speed (MDSS+). Even with these modified version of the Schaake Shuffle, we found that the StSS method provided the highest Brier skill scores overall using real data. However, all of these methods provided improvements over the raw HRRR forecasts, which struggled to capture the diurnal cycle and magnitude of the relative frequency of up- and down-ramp events. These methods also reduced the over- and under-forecasting biases of the raw forecasts at the M5 and PNW tower locations, respectively. We compared the three Schaake Shuffle methods at forecasting ramp events using a dataset of 25 years of synthetic forecasts and observations to emphasize the differences among the multivariate methods without constraints from the limited real dataset. We found that the MDSS+ method had significantly higher skill compared to the MDSS and was competitive with the StSS method suggesting that inclusion of the lag 1-h wind speed differences is a key component to accurate forecasting of ramp events when preferentially selecting historical scenarios.

We were limited with how much improvement statistical post-processing could provide with the real data, because the correlation between the observations and HRRR forecasts of up- and down-ramps were low. However, we still achieved some positive skill by reducing over- and under-forecasting biases and by employing the multivariate methods to generate probabilistic forecasts for the PNW tower which had overall higher correlation coefficients than that of the M5 tower location. Generally, the greatest skill was achieved for the prediction of up-ramps at the PNW site which also happened to be the ramp type associated with the highest correlation.  This dependence on initial forecast skill is encouraging, because it suggests that for sites with fewer random errors and better skill (e.g., sites over flat terrain), we may be able to achieve significant improvement in forecast skill using these multivariate methods. A longer record of historical scenarios would also be advantageous, because it would increase the likelihood that forecasts would have a good match with past events for selection by the MDSS and MDSS+ methods.

We demonstrated how statistical post-processing can correct forecast biases of up- and down-ramp events and how multivariate statistical methods can be used to generate probabilistic forecasts of wind speed and power scenarios. These methods can be implemented for real-time wind-farm operations using historical observations at a particular wind farm to gain uncertainty information regarding ramp forecasts. We used the generic IEC power curve to convert wind speed scenarios to power scenarios, but wind power forecasters should use their own turbine-specific power curves to further reduce uncertainty. Additionally, these methods are applicable with other numerical weather prediction models besides the HRRR model. Therefore, wind power forecasters can use forecasts from their proprietary models as long as observations are available during the same time period for verification. Enhancements to the forecasts provided by gaining uncertainty information should help with decision-making in the energy-sector not only for direct power generation, but also for scheduling the availability of transmission lines, energy reserves, and energy trading. These methods may find utility in assessing risks of other wind-speed dependent phenomena like wildfire propagation or pollution dispersion.

## 4.6 DATA AVAILABILITY

Data from the M5 meteorological tower are available at https://wind.nrel.gov/MetData/135mData/M5Twr/. Data from the PNW tower are available by request from Avangrid (contact Michael Zulauf, Ph.D). The HRRR forecast data are available from the National Oceanic and Atmospheric Administration Global Systems Division (contact Eric James or Stanley Benjamin).

## 4.7 ACKNOWLEDGEMENTS

The authors express appreciation for Eric James and Stanley Benjamin at NOAA and CIRES for providing the raw HRRR data and NREL for providing the M5 tower data. The authors express great appreciation to Avangrid for the collection and provision of the data from the PNW meteorological tower. We are greatly appreciative of Laura Bianco and Irina Djalalova from NOAA and CIRES and James Wilczak from NOAA for sharing their expertise of wind ramps and of the PNW tower location. Funding for this work was provided by NOAA under the federal Pathways Program.

# 5 OVERALL CONCLUSION

## 5.1 SUMMARY OF MAJOR FINDINGS

The work presented in this dissertation seeks to answer how various extreme wind characteristics in the atmospheric boundary layer influence wind turbine design and challenge accurate wind power forecasting. The studies herein 1) quantified power spectral density and spatial coherence characteristics within the hurricane boundary layer for wind turbine design applications using two configurations of large-eddy simulations (LES) (Chapter 2; Worsnop et al. 2017a), 2) assessed the mean wind speed, 3-s gusts, wind veer, and directional shear within a simulated Category 5 hurricane and compared values to current wind turbine design standards (Chapter 3; Worsnop et al. 2017b), and 3) utilized statistical post-processing to correct forecasting biases of the High-Resolution Rapid Refresh (HRRR) model at predicting up- and down-ramp events as well as provided uncertainty information by generating numerous forecast scenarios (Chapter 4; Worsnop et al. 2018).

In Chapter 2, large-eddy simulations from two configurations (i.e., Complex and Simple) of the Cloud Model 1 (CM1) numerical model were compared to assess the validity of the relatively Simple configuration to represent realistic hurricane wind profiles. Comparisons of normalized mean wind speed and standard deviation as well as power spectral density of a Category 5 hurricane at multiple hurricane radii and heights from the Complex and Simple simulations revealed that the Simple setup produced turbulent wind characteristics similar to those of a more complex hurricane configuration. I conclude that the Simple setup is suitable to create realistic wind profiles in the hurricane boundary layer (HBL) away from the eyewall. Comparisons between the Simple simulations and a rare low-altitude observational dataset collected during the CBLAST experiment further verified the turbulent characteristics of the Simple model.

Continuing analysis with the Simple setup in Chapter 2, I analyzed power spectral density and coherence within the hurricane boundary layer using LES with a horizontal grid spacing ≈ 10 m and $\Delta t = 0.1$ s. Additionally, I examined these characteristics within tropical cyclones of different strengths (using wind speeds at different radii of the overall Category 5 hurricane as a proxy for different hurricane strengths) ranging from tropical storm to Category 4 on the Saffir-Simpson hurricane wind scale.

The power-spectral-density analyses revealed that the power spectrum of the wind speed in the HBL is dependent on hurricane wind speed. The peak of the power spectral density increased in magnitude as the hurricane intensity increased. The vertical extent of the peak power spectral density in the HBL also increased with increasing hurricane intensity. When comparing the power spectral density derived from the Simple setup to the standard Kaimal and von Kármán spectral models, I found that the empirical and theoretical spectral models underestimated the magnitude of the power spectral density in the HBL for all hurricane intensities. Further, the peaks in the simulated power spectral densities were shifted to higher frequencies than the peaks of the standard spectral models. Modifications of the Kaimal model were proposed to account for the greater variance and the shifted peak in turbulent energy to higher frequencies in hurricanes.

I also analyzed coherence in the HBL. In general, the HBL flow remained highly coherent (≥ 0.6 coherence) for relatively large separations. Coherent flow between points separated horizontally by ≈ 60 m was apparent in the Category-4 case, which is roughly the size of a typical turbine blade. The exponential coherence model used in current turbine design standards generally underestimated the coherence for a given horizontal separation but overestimated the coherence for a given vertical separation. For these reasons, adjustments to the coefficients used in the exponential model may be required.

In Chapter 3, I expanded the work in Chapter 2 to analyze hurricane mean wind speed, 3-s gusts, gust factor, and directional veer and shear at hub height. These variables were analyzed, because mean wind speed, 3-s gusts, and gust factor are metrics currently used to design wind turbines for a particular atmospheric environment. Veer and shear are not currently outlined in the design standards for wind turbines, but based on the results in Chapter 3, they may be consequential to turbine loads. To determine the maximum values of the variables mentioned above, and to circumvent the lack of adequate observational data to estimate these values, I ran a LES of an idealized Category 5 hurricane again using CM1. This simulation was like the Complex setup in Chapter 2, but with a horizontal grid spacing of $\approx$ 32 m instead of 62 m. Mock tower data were output throughout the model domain and aggregated into 1-km radial bins to assess how these variables vary with hurricane radius.

I found that mean wind speeds, 3-s gusts, and gust factor all exceed the corresponding values in the IEC standard for Class I wind turbines. A special class of turbines can be specified for hurricane conditions within the standard, but no specific values are given to help manufacturers build the turbines to withstand strong hurricane conditions. The goal of the research in Chapter 3 was to provide guidance for the design of wind turbines which may endure Category 5 hurricanes. I found that 10-min mean wind speeds exceeded 90 m $s^{-1}$, 3-s gusts exceeded 100 m $s^{-1}$, and gust factor values $> 1.7$ occurred within the eye-eyewall interface, especially below 100 m ASL. Additionally, 10-30° wind shear at hub height suggests turbines may need to rotate at sub-minute response time to avoid loads induced from turbine yaw misalignment. Veer from hub height to the blade tips ranged from 15-50° in the simulated Category 5 hurricane showing that veer may have influence on turbine loads.

Chapter 4 explored wind characteristics outside of hurricanes and focused on power ramp events. Power ramps are large and abrupt increases or decreases in power produced by wind turbines or wind farms. Knowing when ramp events will occur and what magnitude they will be are critical for making decisions regarding the stability of the electrical grid. Additionally, having a range of possible ramp outcomes provides uncertainty information of the forecast, which can allow for situation-dependent decisions. To improve the skill of power ramp forecasts and quantify the uncertainty associated with the forecasts, we used 21 months of 80-m wind speed forecasts from the High Resolution Rapid Refresh (HRRR) model at 13-km horizontal grid spacing. I also utilized wind speed observations from two tall meteorological towers located in eastern Oregon and at the National Wind Technology Center near Boulder, Colorado.

Results in Chapter 4 show that HRRR forecasts can be represented with a gamma or truncated logistic distribution, but not before transforming the forecasts to address the increased variability with wind speed and seasonality within the dataset. I next separated the predictive distributions for each tower into 50 quantiles to represent 50 forecasts for a given forecast initialization (00Z or 12Z) and forecast lead time out to 12 h. I used three variants of the Schaake Shuffle method (Clark et al. 2004), StSS, MDSS, and MDSS+, to generate wind speed forecast scenarios based on historical wind speed observations. Additionally, I also generated wind speed scenarios using a Gaussian copula method, which does not rely on the current forecast like the Schaake Shuffle methods, but instead uses an exponential covariance model defined by an empirical range parameter. The wind speed scenarios from all methods were then converted to power scenarios using the IEC power curve before identifying power ramp events.

To quantify the improvement of these methods at predicting ramp events over the raw HRRR forecasts, I computed the relative frequency of up- and down-ramp events. Results show that the three Schaake Shuffle methods correct under- and over-forecasting biases of the raw HRRR forecasts, with the StSS method providing the closest number of ramp events to that of the observed. Brier skill scores (BSS) of each method showed that the best forecast skill is gained for the Oregon (PNW) site, especially for up-ramps. It was difficult to gain any positive skill at the Colorado (M5) site, because random errors existed in the original HRRR forecasts likely due to the very complex terrain in this location. Nonetheless, the results demonstrated that statistical post-processing and the multivariate methods used to generate forecast scenarios can produce positive forecast skill at predicting ramp events and provide uncertainty information.

In summary, these three studies illustrate the implications that extreme and irregular wind characteristics have on wind energy development. I modeled hurricane-force winds to quantify various turbulence and wind characteristics that could impact offshore wind turbine design. I also used observations and forecasts at two onshore sites in complex terrain to assess and improve power ramp forecasts, which have enormous implications for electrical grid stability and wind energy reliability. With continued global interest in renewable energy, wind energy will continue to be a top contender in the energy sector. Knowledge of atmospheric processes, including the extreme, that influence the production of wind power is a vital component to its success.

## 5.2 OUTLOOK

Several opportunities exist to extend the work presented in this dissertation. Chapters 2 and 3 explored various turbulent and wind characteristics within the hurricane boundary layer. Much of the work in those chapters compared the magnitude of variables currently used to design wind turbines to the magnitude of those variables expected during hurricanes. Additionally, new variables that may be consequential such as veer across the rotor layer and directional shear at hub height were also recommended for consideration in the design standards. A natural progression of this work would be to test the effect of these values in turbine load simulators such as FAST (Jonkman and Buhl 2005). Running several load simulations with a range of values for gusts, gust factor, veer, shear, and modifications to the power spectral density and coherence curves would help identify which variables contribute to significant loads on turbines in hurricane conditions. These various load simulations would also help define thresholds for veer and shear, which could be included in upcoming versions of the IEC design standard.

Another avenue to extend the research discussed in Chapters 2 and 3 would be to run the complex configuration of CM1 (CM1C) for different tropical cyclone strengths ranging from Tropical Storm to Category 4 (in addition to the Category 5 simulation analyzed herein) to create a comprehensive LES dataset of hurricane simulations that would not only be useful for the wind energy community, but also for the hurricane community. LES provide insight into all regions of the hurricane that are not afforded by observations. These simulations could be used to create turbine design standards for offshore turbines in areas most prone to hurricanes of a particular strength. For instance, wind farm developers who deploy wind turbines in the waters off the US NE coastline may want to install wind turbines designed to withstand up to Category 2 hurricanes, while a developer interested in the Gulf of Mexico may want to design turbines to withstand up to Category 5 conditions.

Enhancements to the simulations beyond varying the hurricane strength could involve coupling the CM1 model with a wave model such as WAVEWATCH III (WW3DG 2016) to include the effects of waves on wind characteristics and turbine loads. Using a different atmospheric model such as the Advanced Research Weather Research and Forecasting (WRF-ARW) model is also a possibility. A further enhancement could be the inclusion of wind turbines within the simulation using either a wind farm parameterization (Fitch et al. 2012) or a generalized actuator disk model (Mirocha et al. 2014) to represent the interaction between wind turbines and the environment.

The work from Chapter 4 could be extended by generating forecast scenarios using the same multivariate methods, but for a region of flat terrain or over the ocean rather than complex terrain. Since the amount of improvement to the forecasts through statistical post-processing was limited to the skill of the initial forecasts, significant skill using the statistical post-processing methods could be gained for sites that are better-forecasted (e.g., not as complex). These multivariate methods could also be used to create a real-time forecasting tool for a particular wind farm using proprietary or public forecasting models run with a domain specifically for the wind farm. This tool may take on the following functions for a given wind farm by 1) assimilating wind turbine data of the wind farm into a regional forecast model, 2) generating forecast scenarios of wind speed or power using the different multivariate methods discussed in Chapter 4, 3) using those scenarios to predict wind speed, power, and ramp events to trade energy, to manage the electrical grid, and to maximize wind farm profits.

There are still many unanswered questions to explore regarding the influence of atmospheric phenomena on wind energy. Collaborations between turbine engineers and atmospheric scientists ensure that consequential atmospheric events are accounted for in wind turbine design and development. Additionally, communication between these groups ensures that atmospheric scientists provide variables on time and spatial scales that are most useful and relevant for the designers. Further collaborations to answer atmospheric questions will continue to improve the success of wind as a reliable and competitive energy source worldwide.

# REFERENCES

A2E, 2017: WFIP2 Wind Forecast Improvement Project 2. https://a2e.energy.gov/projects/wfip2 (Accessed October 30, 2017).

Aberson, S. D., M. Black, M. T. Montgomery, and M. Bell, 2006: Hurricane Isabel (2003): New Insights Into the Physics of Intense Storms. Part II: Extreme Localized Wind. *Bull. Am. Meteorol. Soc.*, **87**, 1349–1354, doi:10.1175/BAMS-87-10-1349.

Aitken, M. L., B. Kosović, J. D. Mirocha, and J. K. Lundquist, 2014: Large eddy simulation of wind turbine wake dynamics in the stable boundary layer using the Weather Research and Forecasting Model. *J. Renew. Sustain. Energy*, **6**, 33137, doi:10.1063/1.4885111.

Andreas, E. L., L. Mahrt, and D. Vickers, 2012: A New Drag Relation for Aerodynamically Rough Flow over the Ocean. *J. Atmospheric Sci.*, **69**, 2520–2537, doi:10.1175/JAS-D-11-0312.1.

Archer, C. L., and M. Z. Jacobson, 2007: Supplying Baseload Power and Reducing Transmission Requirements by Interconnecting Wind Farms. *J. Appl. Meteorol. Climatol.*, **46**, 1701–1717, doi:10.1175/2007JAMC1538.1.

——, and Coauthors, 2013: Meteorology for Coastal/Offshore Wind Energy in the United States: Recommendations and Research Needs for the Next 10 Years. *Bull. Am. Meteorol. Soc.*, **95**, 515–519, doi:10.1175/BAMS-D-13-00108.1.

——, B. A. Colle, D. L. Veron, F. Veron, and M. J. Sienkiewicz, 2016: On the predominance of unstable atmospheric conditions in the marine boundary layer offshore of the U.S. northeastern coast. *J. Geophys. Res. Atmospheres*, **121**, 2016JD024896, doi:10.1002/2016JD024896.

AWEA, A. W. E. A., 2017: U.S. Wind Energy State Facts. Texas Wind Energy. https://www.awea.org/state-fact-sheets (Accessed October 15, 2017).

Bell, M. M., M. T. Montgomery, and K. A. Emanuel, 2012: Air–Sea Enthalpy and Momentum Exchange at Major Hurricane Wind Speeds Observed during CBLAST. *J. Atmospheric Sci.*, **69**, 3197–3222, doi:10.1175/JAS-D-11-0276.1.

Bender, M. A., T. R. Knutson, R. E. Tuleya, J. J. Sirutis, G. A. Vecchi, S. T. Garner, and I. M. Held, 2010: Modeled Impact of Anthropogenic Warming on the Frequency of Intense Atlantic Hurricanes. *Science*, **327**, 454–458, doi:10.1126/science.1180568.

Benjamin, S. G., and Coauthors, 2015: A North American Hourly Assimilation and Model Forecast Cycle: The Rapid Refresh. *Mon. Weather Rev.*, **144**, 1669–1694, doi:10.1175/MWR-D-15-0242.1.

Bianco, L., I. V. Djalalova, J. M. Wilczak, J. Cline, S. Calvert, E. Konopleva-Akish, C. Finley, and J. Freedman, 2016: A Wind Energy Ramp Tool and Metric for Measuring the Skill of Numerical Weather Prediction Models. *Weather Forecast.*, **31**, 1137–1156, doi:10.1175/WAF-D-15-0144.1.

Bilgili, M., A. Yasar, and E. Simsek, 2011: Offshore wind power development in Europe and its comparison with onshore counterpart. *Renew. Sustain. Energy Rev.*, **15**, 905–915, doi:10.1016/j.rser.2010.11.006.

Black, P. G., and Coauthors, 2007: Air–Sea Exchange in Hurricanes: Synthesis of Observations from the Coupled Boundary Layer Air–Sea Transfer Experiment. *Bull. Am. Meteorol. Soc.*, **88**, 357–374, doi:10.1175/BAMS-88-3-357.

Blackman, R., and J. Tukey, 1959: *The Measurement of Power Spectra*. Dover, 190 pp.

BOEM, B. of O. E. M., 2017: Offshore wind energy. *Bur. Ocean Energy Manag.*,. https://www.boem.gov/Renewable-Energy-Program/Renewable-Energy-Guide/Offshore-Wind-Energy.aspx (Accessed November 15, 2017).

Bossavy, A., R. Girard, and G. Kariniotakis, 2013: Forecasting ramps of wind power production with numerical weather prediction ensembles. *Wind Energy*, **16**, 51–63, doi:10.1002/we.526.

Bremnes, J. B., 2006: A comparison of a few statistical models for making quantile wind power forecasts. *Wind Energy*, **9**, doi:10.1002/we.182. http://www.readcube.com/articles/10.1002/we.182 (Accessed August 8, 2017).

Bryan, G. H., 2012: Effects of Surface Exchange Coefficients and Turbulence Length Scales on the Intensity and Structure of Numerically Simulated Hurricanes. *Mon. Weather Rev.*, **140**, 1125–1143, doi:10.1175/MWR-D-11-00231.1.

——, and R. Rotunno, 2009: The Maximum Intensity of Tropical Cyclones in Axisymmetric Numerical Model Simulations. *Mon. Weather Rev.*, **137**, 1770–1789, doi:10.1175/2008MWR2709.1.

——, J. C. Wyngaard, and J. M. Fritsch, 2003: Resolution Requirements for the Simulation of Deep Moist Convection. *Mon. Weather Rev.*, **131**, 2394–2416, doi:10.1175/1520-0493(2003)131<2394:RRFTSO>2.0.CO;2.

——, R. P. Worsnop, J. K. Lundquist, and J. A. Zhang, 2017: A Simple Method for Simulating Wind Profiles in the Boundary Layer of Tropical Cyclones. *Bound.-Layer Meteorol.*, **162**, 475–502, doi:10.1007/s10546-016-0207-0.

Budischak, C., D. Sewell, H. Thomson, L. Mach, D. E. Veron, and W. Kempton, 2013: Cost-minimized combinations of wind power, solar power and electrochemical storage, powering the grid up to 99.9% of the time. *J. Power Sources*, **225**, 60–74, doi:10.1016/j.jpowsour.2012.09.054.

Chen, X., and J. Z. Xu, 2016: Structural failure analysis of wind turbines impacted by super typhoon Usagi. *Eng. Fail. Anal.*, **60**, 391–404, doi:10.1016/j.engfailanal.2015.11.028.

Cione, J. J., E. A. Kalina, E. W. Uhlhorn, A. M. Farber, and B. Damiano, 2016: Coyote unmanned aircraft system observations in Hurricane Edouard (2014). *Earth Space Sci.*, **3**, 2016EA000187, doi:10.1002/2016EA000187.

Clark, M., S. Gangopadhyay, L. Hay, B. Rajagopalan, and R. Wilby, 2004: The Schaake Shuffle: A Method for Reconstructing Space–Time Variability in Forecasted Precipitation and Temperature Fields. *J. Hydrometeorol.*, **5**, 243–262, doi:10.1175/1525-7541(2004)005<0243:TSSAMF>2.0.CO;2.

Clausen, N.-E., A. Candelaria, S. Gjerding, S. Hernando, P. Norgard, S. Ott, and N.-J. Tarp-Johansen, 2007: Wind Farms in Regions Exposed to Tropical Cyclones. European Wind Energy Conference and Exhibition, Milan, Italy, European Wind Energy Association https://www.researchgate.net/profile/Samuel_Hernando/publication/228491415_Wind_farms_in_regions_exposed_to_tropical_cyclones/links/56c6d0d608ae408dfe4e67e0.pdf.

Clifton, A., S. Schreck, G. Scott, N. Kelley, and J. K. Lundquist, 2013: Turbine Inflow Characterization at the National Wind Technology Center. *J. Sol. Energy Eng.*, **135**, 031017–031017, doi:10.1115/1.4024068.

Cruz, A. M., and E. Krausmann, 2008: Damage to offshore oil and gas facilities following hurricanes Katrina and Rita: An overview. *J. Loss Prev. Process Ind.*, **21**, 620–626, doi:10.1016/j.jlp.2008.04.008.

Dawid, A. P., 1984: Present Position and Potential Developments: Some Personal Views: Statistical Theory: The Prequential Approach. *J. R. Stat. Soc. Ser. Gen.*, **147**, 278–292, doi:10.2307/2981683.

Delle Monache, L., F. A. Eckel, D. L. Rife, B. Nagarajan, and K. Searight, 2013: Probabilistic Weather Prediction with an Analog Ensemble. *Mon. Weather Rev.*, **141**, 3498–3516, doi:10.1175/MWR-D-12-00281.1.

Demuth, J. L., M. DeMaria, and J. A. Knaff, 2006: Improvement of Advanced Microwave Sounding Unit Tropical Cyclone Intensity and Size Estimation Algorithms. *J. Appl. Meteorol. Climatol.*, **45**, 1573–1581, doi:10.1175/JAM2429.1.

DOE, D. of E., 2015: Wind Vision: A New Era for Wind Power in the United States. http://www.energy.gov/sites/prod/files/WindVision_Report_final.pdf.

DOE, U. S. D. of E., 2017: *2016 Wind Technologies Market Report*. https://energy.gov/sites/prod/files/2017/08/f35/2016_Wind_Technologies_Market_Report_0.pdf (Accessed October 15, 2017).

Dvorak, M. J., E. D. Stoutenburg, C. L. Archer, W. Kempton, and M. Z. Jacobson, 2012: Where is the ideal location for a US East Coast offshore grid? *Geophys. Res. Lett.*, **39**, L06804, doi:10.1029/2011GL050659.

Eide, S. S., J. B. Bremnes, and I. Steinsland, 2017: Bayesian model averaging for wind speed ensemble forecasts using wind speed and direction.

Fadaeinedjad, R., G. Moschopoulos, and M. Moallem, 2009: The Impact of Tower Shadow, Yaw Error, and Wind Shears on Power Quality in a Wind #x2013;Diesel System. *IEEE Trans. Energy Convers.*, **24**, 102–111, doi:10.1109/TEC.2008.2008941.

Ferreira, C., J. Gama, L. Matias, A. Botterud, and J. Wang, 2010: *A survey on wind power ramp forecasting*. Argonne National Laboratory, http://www.ipd.anl.gov/anlpubs/2011/02/69166.pdf.

Fitch, A. C., J. B. Olson, J. K. Lundquist, J. Dudhia, A. K. Gupta, J. Michalakes, and I. Barstad, 2012: Local and Mesoscale Impacts of Wind Farms as Parameterized in a Mesoscale NWP Model. *Mon. Weather Rev.*, **140**, 3017–3038, doi:10.1175/MWR-D-11-00352.1.

French, J. R., W. M. Drennan, J. A. Zhang, and P. G. Black, 2007: Turbulent Fluxes in the Hurricane Boundary Layer. Part I: Momentum Flux. *J. Atmospheric Sci.*, **64**, 1089–1102, doi:10.1175/JAS3887.1.

Gneiting, T., and A. E. Raftery, 2007: Strictly Proper Scoring Rules, Prediction, and Estimation. *J. Am. Stat. Assoc.*, **102**, 359–378, doi:10.1198/016214506000001437.

——, ——, A. H. Westveld, and T. Goldman, 2005: Calibrated Probabilistic Forecasting Using Ensemble Model Output Statistics and Minimum CRPS Estimation. *Mon. Weather Rev.*, **133**, 1098–1118, doi:10.1175/MWR2904.1.

——, K. Larson, K. Westrick, M. G. Genton, and E. Aldrich, 2006: Calibrated Probabilistic Forecasting at the Stateline Wind Energy Center. *J. Am. Stat. Assoc.*, **101**, 968–979, doi:10.1198/016214506000000456.

——, F. Balabdaoui, and A. E. Raftery, 2007: Probabilistic forecasts, calibration and sharpness. *J. R. Stat. Soc. Ser. B Stat. Methodol.*, **69**, 243–268, doi:10.1111/j.1467-9868.2007.00587.x.

GWEC, G. W. E. C., 2017: *Global Wind Report, Annual Market Update*. http://gwec.net/publications/global-wind-report-2/ (Accessed October 15, 2017).

Hara, T., and P. P. Sullivan, 2015a: Wave Boundary Layer Turbulence over Surface Waves in a Strongly Forced Condition. *J. Phys. Oceanogr.*, **45**, 868–883, doi:10.1175/JPO-D-14-0116.1.

——, and ——, 2015b: Wave Boundary Layer Turbulence over Surface Waves in a Strongly Forced Condition. *J. Phys. Oceanogr.*, **45**, 868–883, doi:10.1175/JPO-D-14-0116.1.

Harper, B. A., J. D. Kepert, and J. D. Ginger, 2010: Guidelines For Converting Between Various Wind Averaging Periods in Tropical Cyclone Conditions. http://www.wmo.int/pages/prog/www/tcp/documents/WMO_TD_1555_en.pdf.

Harris, F. J., 1978: On the use of windows for harmonic analysis with the discrete Fourier transform. *Proc. IEEE*, **66**, 51–83, doi:10.1109/PROC.1978.10837.

IEC, I. E. C., 2007a: IEC 61400-1 Wind Turbines- Part 1: Design Requirements, Edition 3, 2007.

——, 2007b: *Wind turbines-Part 12-1: Power performance measurements of electricity producing wind turbines.*

Ishihara, T., A. Yamaguchi, and K. Takahara, 2005: An Analysis of Damaged Wind Turbines by Typhoon Maemi in 2003. *Proceedings of the sixth Asia-Pacific conference on wind engineering*, Seoul, South Korea https://www.researchgate.net/publication/228415873_An_Analysis_of_damaged_wind_turbines_by_typhoon_Maemi_in_2003.

Jeon, J., and J. W. Taylor, 2012: Using Conditional Kernel Density Estimation for Wind Power Density Forecasting. *J. Am. Stat. Assoc.*, **107**, 66–79, doi:10.1080/01621459.2011.643745.

Jonkman, J. M., and M. L. Buhl, 2005: *FAST User's Guide*. National Renewable Energy Laboratory, http://wind.nrel.gov/public/bjonkman/TestPage/FAST.pdf.

——, S. Butterfield, W. Musial, and G. Scott, 2009: *Definition of a 5-MW reference wind turbine for offshore system development*. National Renewable Energy Laboratory, http://www.nrel.gov/docs/fy09osti/38060.pdf.

Jordan, M. R., and C. A. Clayson, 2008: A new approach to using wind speed for prediction of tropical cyclone generated storm surge. *Geophys. Res. Lett.*, **35**, L13802, doi:10.1029/2008GL033564.

Junk, C., L. Delle Monache, and S. Alessandrini, 2015: Analog-Based Ensemble Model Output Statistics. *Mon. Weather Rev.*, **143**, 2909–2917, doi:10.1175/MWR-D-15-0095.1.

Justin Gillis, 2016: America’s First Offshore Wind Farm May Power Up a New Industry. *The New York Times*, August 22.

Kaimal, J. C., J. C. Wyngaard, Y. Izumi, and O. R. Coté, 1972: Spectral characteristics of surface-layer turbulence. *Q. J. R. Meteorol. Soc.*, **98**, 563–589, doi:10.1002/qj.49709841707.

Kamath, C., 2010a: *Using simple statistical analysis of historical data to understand wind ramp events*. Lawrence Livermore National Laboratory, http://ckamath.org/yahoo_site_admin/assets/docs/RampEvents_TR_423242.38225409.pdf (Accessed December 19, 2017).

——, 2010b: Understanding wind ramp events through analysis of historical data. *IEEE PES T D 2010*, IEEE PES T D 2010, 1–6.

——, 2011: Associating weather conditions with ramp events in wind power generation. *2011 IEEE/PES Power Systems Conference and Exposition*, 2011 IEEE/PES Power Systems Conference and Exposition, 1–8.

von Kármán, T. V., and C. C. Lin, 1951: On the Statistical Theory of Isotropic Turbulence1. *Advances in Applied Mechanics*, R.V.M. and T.V. Kármán, Ed., Vol. 2 of, Elsevier, 1–19 http://www.sciencedirect.com/science/article/pii/S0065215608702977 (Accessed November 21, 2016).

Keim, B. D., R. A. Muller, and G. W. Stone, 2007: Spatiotemporal Patterns and Return Periods of Tropical Storm and Hurricane Strikes from Texas to Maine. *J. Clim.*, **20**, 3498–3509, doi:10.1175/JCLI4187.1.

Kepert, J. D., J. Schwendike, and H. Ramsay, 2015: Why is the Tropical Cyclone Boundary Layer Not “Well Mixed”? *J. Atmospheric Sci.*, **73**, 957–973, doi:10.1175/JAS-D-15-0216.1.

Kimball, S. K., and M. S. Mulekar, 2004: A 15-Year Climatology of North Atlantic Tropical Cyclones. Part I: Size Parameters. *J. Clim.*, **17**, 3555–3575, doi:10.1175/1520-0442(2004)017<3555:AYCONA>2.0.CO;2.

Kuik, G. A. M. van, and Coauthors, 2016: Long-term research challenges in wind energy – a research agenda by the European Academy of Wind Energy. *Wind Energy Sci.*, **1**, 1–39, doi:10.5194/wes-1-1-2016.

Landsea, C. W., 1993: A Climatology of Intense (or Major) Atlantic Hurricanes. *Mon. Weather Rev.*, **121**, 1703–1713, doi:10.1175/1520-0493(1993)121<1703:ACOIMA>2.0.CO;2.

Lange, M., and U. Focken, 2006: Overview of Wind Power Prediction Systems. *Physical Approach to Short-Term Wind Power Prediction*, Springer, Berlin, Heidelberg, 7–22 https://link.springer.com/chapter/10.1007/3-540-31106-8_2 (Accessed August 8, 2017).

Larsen, G. C., and K. S. Hansen, 2004: *Database on Wind Characteristics Analyses of Wind Turbine Design Loads*. Risø National Laboratory, Roskilde, Denmark, http://orbit.dtu.dk/fedora/objects/orbit:90481/datastreams/file_7711165/content.

Li, L., A. Kareem, J. Hunt, Y. Xiao, C. Zhou, and L. Song, 2015: Turbulence Spectra for Boundary-Layer Winds in Tropical Cyclones: A Conceptual Framework and Field Measurements at Coastlines. *Bound.-Layer Meteorol.*, **154**, 243–263, doi:10.1007/s10546-014-9974-7.

London Array, 2017: *Lond Array. The world's largest offshore wind farm.* http://www.londonarray.com/wp-content/uploads/London-Array-Brochure.pdf (Accessed October 15, 2017).

Marquis, M., J. Wilczak, M. Ahlstrom, J. Sharp, A. Stern, J. C. Smith, and S. Calvert, 2011: Forecasting the Wind to Reach Significant Penetration Levels of Wind Energy. *Bull. Am. Meteorol. Soc.*, **92**, 1159–1171, doi:10.1175/2011BAMS3033.1.

Messner, J. W., A. Zeileis, J. Broecker, and G. J. Mayr, 2014: Probabilistic wind power forecasts with an inverse power curve transformation and censored regression. *Wind Energy*, **17**, 1753–1766, doi:10.1002/we.1666.

Milligan, M., M. Schwartz, and Y.-H. Wan, 2003: Statistical wind power forecasting models: results for U.S. wind farms. Windpower, Austin, Texas https://www.nrel.gov/docs/fy03osti/33956.pdf.

Mirocha, J. D., B. Kosovic, M. L. Aitken, and J. K. Lundquist, 2014: Implementation of a generalized actuator disk wind turbine model into the weather research and forecasting model for large-eddy simulation applications. *J. Renew. Sustain. Energy*, **6**, 13104, doi:10.1063/1.4861061.

Miyake, M., R. W. Stewart, and R. W. Burling, 1970: Spectra and cospectra of turbulence over water. *Q. J. R. Meteorol. Soc.*, **96**, 138–143, doi:10.1002/qj.49709640714.

Morrison, I., S. Businger, F. Marks, P. Dodge, and J. A. Businger, 2005: An Observational Case for the Prevalence of Roll Vortices in the Hurricane Boundary Layer. *J. Atmospheric Sci.*, **62**, 2662–2673, doi:10.1175/JAS3508.1.

Musial, W., and S. Butterfield, 2004: Future for offshore wind energy in the United States. Energy Ocean, Palm Beach, FL, 16 http://www.nrel.gov/docs/fy04osti/36313.pdf.

Musial, W., D. Heimiller, P. Beiter, G. Scott, and C. Draxl, 2016: *2016 Offshore Wind Energy Resource Assessment for the United States*. National Renewable Energy Laboratory, https://www.nrel.gov/docs/fy16osti/66599.pdf (Accessed October 15, 2017).

Nakanishi, M., and H. Niino, 2012: Large-Eddy Simulation of Roll Vortices in a Hurricane Boundary Layer. *J. Atmospheric Sci.*, **69**, 3558–3575, doi:10.1175/JAS-D-11-0237.1.

NCAR, N. C. for A. R., 2017: NCAR Real-Time Weather Data. *NCAR Real-Time Weather Data*,. http://weather.rap.ucar.edu/surface/ (Accessed September 11, 2017).

Neumann, C., J., 1991: The National Hurricane Center Risk Analysis Program (HURISK). http://www.nhc.noaa.gov/pdf/NWS-NHC-1987-38.pdf.

NHC, N. H. C., 2016: Tropical Cyclone Climatology. http://www.nhc.noaa.gov/climo/ (Accessed September 9, 2016).

Nielsen, H. A., and Coauthors, 2006a: From wind ensembles to probabilistic information about future wind power production – results from an actual application. *2006 International Conference on Probabilistic Methods Applied to Power Systems*, 2006 International Conference on Probabilistic Methods Applied to Power Systems, 1–8.

Nielsen, H. A., H. Madsen, and T. S. Nielsen, 2006b: Using quantile regression to extend an existing wind power forecasting system with probabilistic forecasts. *Wind Energy*, **9**, 95–108, doi:10.1002/we.180.

Nikolaos, N., 2004: Deep water offshore wind technologies. University of Strathclyde, 131 pp. http://www.esru.strath.ac.uk/Documents/MSc_2004/nikolaos.pdf (Accessed November 15, 2017).

NOAA, N. O. and A. A., 2017: Emergency Response Imagery. *Natl. Geod. Survery Emerg. Response Imag.*,. https://storms.ngs.noaa.gov (Accessed October 15, 2017).

Nolan, D. S., 2005: Instabilities in hurricane-like boundary layers. *Dyn. Atmospheres Oceans*, **40**, 209–236, doi:10.1016/j.dynatmoce.2005.03.002.

——, J. A. Zhang, and E. W. Uhlhorn, 2014: On the Limits of Estimating the Maximum Wind Speeds in Hurricanes. *Mon. Weather Rev.*, **142**, 2814–2837, doi:10.1175/MWR-D-13-00337.1.

Park, J., S. Basu, and L. Manuel, 2014: Large-eddy simulation of stable boundary layer turbulence and estimation of associated wind turbine loads. *Wind Energy*, **17**, 359–384, doi:10.1002/we.1580.

Pinson, P., and R. Girard, 2012: Evaluating the quality of scenarios of short-term wind power generation. *Appl. Energy*, **96**, 12–20, doi:10.1016/j.apenergy.2011.11.004.

Pinson, P., H. Madsen, H. A. Nielsen, G. Papaefthymiou, and B. Klöckl, 2009: From probabilistic forecasts to statistical scenarios of short-term wind power production. *Wind Energy*, **12**, 51–62, doi:10.1002/we.284.

Piper, M., and J. K. Lundquist, 2004: Surface Layer Turbulence Measurements during a Frontal Passage. *J. Atmospheric Sci.*, **61**, 1768–1780, doi:10.1175/1520-0469(2004)061<1768:SLTMDA>2.0.CO;2.

Powell, M. D., and S. Cocke, 2012: Hurricane wind fields needed to assess risk to offshore wind farms. *Proc. Natl. Acad. Sci.*, **109**, E2192–E2192, doi:10.1073/pnas.1206189109.

——, P. J. Vickery, and T. A. Reinhold, 2003: Reduced drag coefficient for high wind speeds in tropical cyclones. *Nature*, **422**, 279–283, doi:10.1038/nature01481.

Richter, D. H., R. Bohac, and D. P. Stern, 2016: An Assessment of the Flux Profile Method for Determining Air–Sea Momentum and Enthalpy Fluxes from Dropsonde Data in Tropical Cyclones. *J. Atmospheric Sci.*, **73**, 2665–2682, doi:10.1175/JAS-D-15-0331.1.

Rose, S., P. Jaramillo, M. J. Small, I. Grossmann, and J. Apt, 2012: Quantifying the hurricane risk to offshore wind turbines. *Proc. Natl. Acad. Sci.*, **109**, 3247–3252, doi:10.1073/pnas.1111769109.

Russo, G., 2014: Renewable energy: Wind power tests the waters. *Nature*, **513**, 478–480, doi:10.1038/513478a.

Samenow, J., 2017: Hurricane Maria destroyed Puerto Rico's radar, a critical tool for forecasting. September 25 https://www.washingtonpost.com/news/capital-weather-gang/wp/2017/09/25/hurricane-maria-destroyed-puerto-ricos-radar-a-critical-tool-for-forecasting/?utm_term=.068f1e876b6e (Accessed October 15, 2017).

Saranyasoontorn, K., L. Manuel, and P. S. Veers, 2004: A Comparison of Standard Coherence Models for Inflow Turbulence With Estimates from Field Measurements. *J. Sol. Energy Eng.*, **126**, 1069–1082, doi:10.1115/1.1797978.

Schefzik, R., 2016: A Similarity-Based Implementation of the Schaake Shuffle. *Mon. Weather Rev.*, **144**, 1909–1921, doi:10.1175/MWR-D-15-0227.1.

Scheuerer, M., and D. Möller, 2015: Probabilistic wind speed forecasting on a grid based on ensemble model output statistics. *Ann. Appl. Stat.*, **9**, 1328–1349, doi:10.1214/15-AOAS843.

——, T. M. Hamill, B. Whitin, M. He, and A. Henkel, 2017: A method for preferential selection of dates in the Schaake shuffle approach to constructing spatiotemporal forecast fields of temperature and precipitation. *Water Resour. Res.*, **53**, 3029–3046, doi:10.1002/2016WR020133.

Siebesma, A. P., and Coauthors, 2003: A Large Eddy Simulation Intercomparison Study of Shallow Cumulus Convection. *J. Atmospheric Sci.*, **60**, 1201–1219, doi:10.1175/1520-0469(2003)60<1201:ALESIS>2.0.CO;2.

Sim, C., L. Manuel, and S. Basu, 2010: A Comparison of Wind Turbine Load Statistics for Inflow Turbulence Fields based on Conventional Spectral Models and Large Eddy Simulation. 48th AIAA Aerospace Sciences Meeting, Orlando, FL http://arc.aiaa.org/doi/pdf/10.2514/6.2010-829.

Sommeria, G., 1976: Three-Dimensional Simulation of Turbulent Processes in an Undisturbed Trade Wind Boundary Layer. *J. Atmospheric Sci.*, **33**, 216–241, doi:10.1175/1520-0469(1976)033<0216:TDSOTP>2.0.CO;2.

St. Martin, C., J. K. Lundquist, and M. A. Handschy, 2015: Variability of interconnected wind plants: correlation length and its dependence on variability time scale. *Environ. Res. Lett.*, **10**, 44004, doi:10.1088/1748-9326/10/4/044004.

——, ——, A. Clifton, G. S. Poulos, and S. J. Schreck, 2016: Wind turbine power production and annual energy production depend on atmospheric stability and turbulence. *Wind Energy Sci.*, **1**, 221–236, doi:10.5194/wes-1-221-2016.

Stern, D. P., J. L. Vigh, D. S. Nolan, and F. Zhang, 2015: Revisiting the Relationship between Eyewall Contraction and Intensification. *J. Atmospheric Sci.*, **72**, 1283–1306, doi:10.1175/JAS-D-14-0261.1.

——, G. H. Bryan, and S. D. Aberson, 2016: Extreme Low-Level Updrafts and Wind Speeds Measured by Dropsondes in Tropical Cyclones. *Mon. Weather Rev.*, **144**, 2177–2204, doi:10.1175/MWR-D-15-0313.1.

Stevens, B., C.-H. Moeng, and P. P. Sullivan, 1999: Large-Eddy Simulations of Radiatively Driven Convection: Sensitivities to the Representation of Small Scales. *J. Atmospheric Sci.*, **56**, 3963–3984, doi:10.1175/1520-0469(1999)056<3963:LESORD>2.0.CO;2.

Suzuki, N., T. Hara, and P. P. Sullivan, 2014: Impact of Dominant Breaking Waves on Air–Sea Momentum Exchange and Boundary Layer Turbulence at High Winds. *J. Phys. Oceanogr.*, **44**, 1195–1212, doi:10.1175/JPO-D-13-0146.1.

Thresher, R. W., W. E. Holley, C. E. Smith, N. Jafarey, and S. R. Lin, 1981: *Modeling the response of wind turbines to atmospheric turbulence*. Oregon State Univ., Corvallis (USA). Dept. of Mechanical Engineering, United States, http://www.osti.gov/scitech/biblio/6811573.

UNFCCC, 2015: *Adoption of the Paris Agreement*. UNFCCC, http://unfccc.int/resource/docs/2015/cop21/eng/l09r01.pdf.

Vanderwende, B. J., and J. K. Lundquist, 2012: The modification of wind turbine performance by statistically distinct atmospheric regimes. *Environ. Res. Lett.*, **7**, 34035, doi:10.1088/1748-9326/7/3/034035.

Vickery, P. J., and P. F. Skerlj, 2005: Hurricane Gust Factors Revisited. *J. Struct. Eng.*, **131**, 825–832, doi:10.1061/(ASCE)0733-9445(2005)131:5(825).

——, D. Wadhera, M. D. Powell, and Y. Chen, 2009: A Hurricane Boundary Layer and Wind Field Model for Use in Engineering Applications. *J. Appl. Meteorol. Climatol.*, **48**, 381–405, doi:10.1175/2008JAMC1841.1.

Walter, K., C. C. Weiss, A. H. P. Swift, J. Chapman, and N. D. Kelley, 2009: Speed and Direction Shear in the Stable Nocturnal Boundary Layer. *J. Sol. Energy Eng.*, **131**, 11013, doi:10.1115/1.3035818.

Wang, H., R. J. Barthelmie, S. C. Pryor, and H. G. Kim, 2014: A new turbulence model for offshore wind turbine standards. *Wind Energy*, **17**, 1587–1604, doi:10.1002/we.1654.

Wicker, L. J., and W. C. Skamarock, 2002: Time-Splitting Methods for Elastic Models Using Forward Time Schemes. *Mon. Weather Rev.*, **130**, 2088–2097, doi:10.1175/1520-0493(2002)130<2088:TSMFEM>2.0.CO;2.

Wilczak, J., and Coauthors, 2014: The Wind Forecast Improvement Project (WFIP): A Public–Private Partnership Addressing Wind Energy Forecast Needs. *Bull. Am. Meteorol. Soc.*, **96**, 1699–1718, doi:10.1175/BAMS-D-14-00107.1.

Worsnop, R., M. Scheuerer, T. M. Hamill, and J. K. Lundquist, 2018: Generating wind power scenarios for probabilistic ramp event prediction using multivariate statistical post-processing. *Wind Energy Science*, **In prep.**

Worsnop, R. P., G. H. Bryan, J. K. Lundquist, and J. A. Zhang, 2017a: Using Large-Eddy Simulations to Define Spectral and Coherence Characteristics of the Hurricane Boundary Layer for Wind-Energy Applications. *Bound.-Layer Meteorol.*, 1–32, doi:10.1007/s10546-017-0266-x.

——, J. K. Lundquist, G. H. Bryan, R. Damiani, and W. Musial, 2017b: Gusts and shear within hurricane eyewalls can exceed offshore wind turbine design standards. *Geophys. Res. Lett.*, **44**, 2017GL073537, doi:10.1002/2017GL073537.

Wurman, J., and J. Winslow, 1998: Intense Sub-Kilometer-Scale Boundary Layer Rolls Observed in Hurricane Fran. *Science*, **280**, 555–557, doi:10.1126/science.280.5363.555.

The WAVEWATCH III Development Group (WW3DG), 2016: User manual and system documentation of WAVEWATCH III version 5.16. Tech. Note 329, NOAA/NWS/NCEP/MMAB, College Park, MD, USA, 326 pp. + Appendices.

Yang, Q., L. K. Berg, M. Pekour, J. D. Fast, R. K. Newsom, M. Stoelinga, and C. Finley, 2013: Evaluation of WRF-Predicted Near-Hub-Height Winds and Ramp Events over a Pacific Northwest Site with Complex Terrain. *J. Appl. Meteorol. Climatol.*, **52**, 1753–1763, doi:10.1175/JAMC-D-12-0267.1.

Yu, B., A. G. Chowdhury, and F. J. Masters, 2008: Hurricane Wind Power Spectra, Cospectra, and Integral Length Scales. *Bound.-Layer Meteorol.*, **129**, 411–430, doi:10.1007/s10546-008-9316-8.

Zhang, J. A., 2010a: Spectral characteristics of turbulence in the hurricane boundary layer over the ocean between the outer rain bands. *Q. J. R. Meteorol. Soc.*, **136**, 918–926, doi:10.1002/qj.610.

——, 2010b: Estimation of Dissipative Heating Using Low-Level In Situ Aircraft Observations in the Hurricane Boundary Layer. *J. Atmospheric Sci.*, **67**, 1853–1862, doi:10.1175/2010JAS3397.1.

——, and W. M. Drennan, 2012: An Observational Study of Vertical Eddy Diffusivity in the Hurricane Boundary Layer. *J. Atmospheric Sci.*, **69**, 3223–3236, doi:10.1175/JAS-D-11-0348.1.

——, K. B. Katsaros, P. G. Black, S. Lehner, J. R. French, and W. M. Drennan, 2008: Effects of Roll Vortices on Turbulent Fluxes in the Hurricane Boundary Layer. *Bound.-Layer Meteorol.*, **128**, 173–189, doi:10.1007/s10546-008-9281-2.

——, W. M. Drennan, P. G. Black, and J. R. French, 2009: Turbulence Structure of the Hurricane Boundary Layer between the Outer Rainbands. *J. Atmospheric Sci.*, **66**, 2455–2467, doi:10.1175/2009JAS2954.1.

——, F. D. Marks, M. T. Montgomery, and S. Lorsolo, 2010: An Estimation of Turbulent Characteristics in the Low-Level Region of Intense Hurricanes Allen (1980) and Hugo (1989). *Mon. Weather Rev.*, **139**, 1447–1462, doi:10.1175/2010MWR3435.1.

——, R. F. Rogers, D. S. Nolan, and F. D. Marks, 2011: On the Characteristic Height Scales of the Hurricane Boundary Layer. *Mon. Weather Rev.*, **139**, 2523–2535, doi:10.1175/MWR-D-10-05017.1.

# APPENDICES. SUPPLEMENT TO CHAPTER 4

## APPENDIX A: DETERMINATION OF RANGE PARAMETER FOR EXPONENTIAL COVARIANCE MODEL

The range parameter $\nu$ defines the decay of correlation of the exponential covariance model (Eq. 3) among lead times. We determined the range parameters for use in the Gaussian copula method (Sect. 4.3.3.1) by choosing values of $\nu$ that best-aligned with the observed correlation of the Gaussian wind speeds at each tower location and forecast initialization time. We used $\nu = 2.5$ (associated with the purple lines **Error! Reference source not found.**a and b) and $\nu = 1.5$ (associated with the orange lines in **Error! Reference source not found.**c and d) for the PNW and M5 tower locations, respectively. We only considered lagged-lead time correlations out to 6 h, because our largest ramp window size is 6 h.

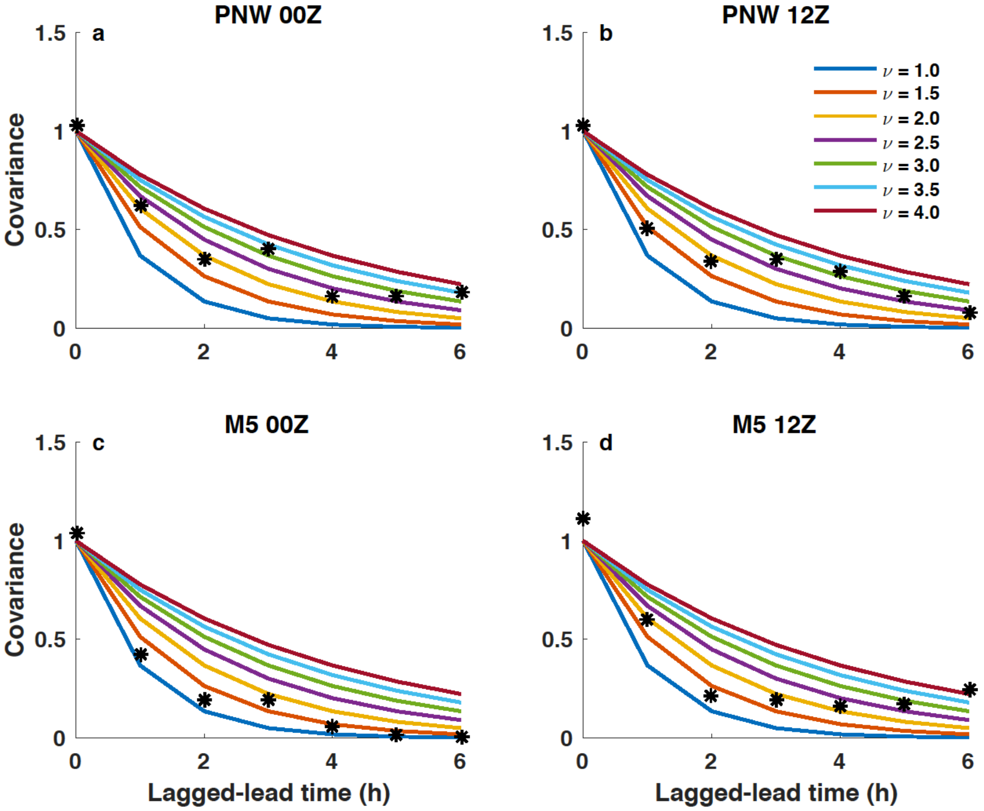

Figure A 1 Exponential covariance models (solid lines) given different values of the range parameter $\boldsymbol{\nu}$ ranging from 1 to 4 in increments of 0.5 as a function of lagged-lead time. Overlaid are the observed covariance values (black asterisk) of the Gaussian wind speed values. Covariance is shown from the PNW (a, b) and M5 (c, d) tower locations for 00Z (a, c) and 12Z (b, d) forecast initialization times.

## APPENDIX B: GENERATION OF A SYNTHETIC DATASET TO OVERCOME SAMPLE SIZE LIMITATIONS

To generate a synthetic wind speed dataset (deterministic forecasts and observations) we use again a Gaussian copula approach, now applied to unconditional (climatological) marginal distributions. For simplicity, we assume the same climatology at each day of the year and each time of the day. Serial dependence in the Gaussian space is modelled via AR(1) processes, i.e. autoregressive processes of order one, that are used to generate two dependent time series $(z_t^{(x)})_{t=1,..,T}$ and $(z_t^{(y)})_{t=1,..,T}$ with time index ranging from 1 to T. We proceed in two steps:

1. Simulate a bivariate Gaussian time series with zero mean and marginal variances equal to 1

- let $\rho = 0.8$ be the correlation between the forecast and observation time series
- simulate an AR(1) time series $(z_t^{(y)})_{t=1,..,T}$ corresponding to the 25 years of data, using $\phi = e^{-0.5}$ as the autoregression parameter and $\sigma^2 = 1-\phi^2$ as the variance of the driving white noise process
- simulate another AR(1) time series $(\varepsilon_t)_{t=1,..,T}$ with the exact same specifications
- define a third time series $(z_t^{(x)})_{t=1,..,T}$ as $z_t^{(x)} = \rho \cdot z_t^{(y)} + \sqrt{1-\rho^2} \cdot \varepsilon_t$

By this construction, the correlation coefficient of the time series $(z_t^{(x)})_{t=1,..,T}$ and $(z_t^{(y)})_{t=1,..,T}$ at each time t is $\rho$.

2. Transform to a bivariate time series with gamma-distributed margins

- denote by $F^{-1}_{G(3,3)}$ the inverse CDF of a gamma distribution with shape parameter 3 and scale parameter 3
- denote by $\Phi$ the CDF of a standard Gaussian distribution
- the observation time series is then defined by $y_t = F^{-1}_{\Gamma(3,3)}(\Phi(z_t^{(y)}))$ for $t = 1,\ldots,T$.
- the forecast time series is defined by $x_t = F^{-1}_{\Gamma(3,3)}(\Phi(z_t^{(x)}))$ for $t = 1,\ldots,T$.